Fractional Chern insulators versus nonmagnetic states in twisted bilayer $MoTe_2$

Jiabin Yu,[1] Jonah Herzog-Arbeitman,[1] Minxuan Wang,[2] Oskar Vafek,[2,3] B. Andrei Bernevig,[1,4,5] and Nicolas Regnault[1,6]

[1]*Department of Physics, Princeton University, Princeton, New Jersey 08544, USA*
[2]*National High Magnetic Field Laboratory, Tallahassee, Florida, 32310, USA*
[3]*Department of Physics, Florida State University, Tallahassee, Florida 32306, USA*
[4]*Donostia International Physics Center, P. Manuel de Lardizabal 4, 20018 Donostia-San Sebastian, Spain*
[5]*IKERBASQUE, Basque Foundation for Science, Bilbao, Spain*
[6]*Laboratoire de Physique de l'Ecole normale supérieure, ENS, Université PSL, CNRS, Sorbonne Université, Université Paris-Diderot, Sorbonne Paris Cité, 75005 Paris, France*

(Received 4 October 2023; accepted 18 December 2023; published 29 January 2024)

Fractionally filled Chern bands with strong interactions may give rise to fractional Chern insulator (FCI) states, the zero-field analog of the fractional quantum Hall effect. Recent experiments have demonstrated the existence of FCIs in twisted bilayer $MoTe_2$ without external magnetic fields—most robust at $\nu = -2/3$—as well as Chern insulators (CIs) at $\nu = -1$. Although the appearance of both of these states is theoretically natural in an interacting topological system, experiments repeatedly observe nonmagnetic (or weakly magnetic) states (lacking FCIs) at $\nu = -1/3$ and $-4/3$, a puzzling result, which has not been fully theoretically explained. In this paper, we perform Hartree-Fock and exact diagonalization calculations to test whether the standard $MoTe_2$ moiré model with the (greatly varying) parameter values available in the literature can reproduce the nonmagnetic/weakly magnetic states at $\nu = -1/3$ and $-4/3$ in unison with the FCI at $\nu = -2/3$ and CI state at $\nu = -1$. We focus on the experimentally relevant twist angles and, crucially, include remote bands. We find that the parameters proposed in Wang *et al.* [arXiv:2306.02501] can nearly capture the experimental phenomena at $\nu = -1/3, -2/3, -1, -4/3$ simultaneously, although the predicted ground states at $\nu = -1/3$ are still mostly FCIs and a larger dielectric constant $\epsilon > 10$ than is typical of hexagonal boron nitride (h-BN) substrate $\epsilon \sim 6$ is required. Our results show the importance of remote bands in identifying the competing magnetic orders and lay the groundwork for further study of the realistic phase diagram.

DOI: 10.1103/PhysRevB.109.045147

I. INTRODUCTION

As proposed more than a decade ago [1–3], interactions can induce fractional Chern insulator (FCI) states when nearly flat Chern bands [4,5] (in zero magnetic field) are fractionally filled. Owing to the development of moiré materials [6,7], there has been extensive theoretical [8–21] interest in the realization of FCI states in this platform. First steps towards FCIs were taken through the experimental observation of fractional quantum Hall (FQH)-like states in twisted bilayer graphene [22] and in bilayer graphenehexagonal boron nitride (h-BN) heterostructures [23], both—especially the latter—requiring a large external magnetic field. Remarkably, recent experiments [24–27] demonstrated true FCI states without external magnetic fields in twisted bilayer $MoTe_2$ ($tMoTe_2$) at fractional fillings $\nu = -2/3, -3/5$, as well as a Chern insulator (CI) exhibiting the integer quantum anomalous Hall effect at $\nu = -1$, spurring immediate theoretical interest [28–38]. (ν is the electron filling measured from the charge neutrality point.) The FCI and CI states observed in the experiments have been reproduced theoretically [28,29,31,32,34,36,37] based on the continuum model proposed in Ref. [39].

Reference [39] already showed that the valley-filtered bands exhibit a Chern number at the single-particle level. Fractionally filling them ought to produce FCIs, as Refs. [1–3] showed at multiple rational fillings of Chern bands. However, there is a puzzling and essential departure from the typical FCI phase diagram [1–3]. Unlike at $\nu = -2/3$, experiments [24–27] repeatedly found nonmagnetic/weakly magnetic (and non-FCI) states at $\nu = -1/3$, although several existing theoretical studies [29,31] have predicted the experimentally nonexistent $\nu = -1/3$ FCI at experimentally relevant angles. The magnetic ordering at $\nu = -1/3$ in comparison to $\nu = -2/3$ was studied in Refs. [28,29], but remote bands were neglected. Robust nonmagnetic states were also found at $\nu = -4/3$ in experiments, despite $\nu = -4/3$ being the particle-hole (PH) partner of $\nu = -2/3$ within the lowest-energy *spinful* bands. The ground state at $\nu = -4/3$ has not been theoretically studied. The full phase diagram poses an unavoidable question for theory: Can the known continuum model of Ref. [39] with the widely used parameter values [28,29,31,32,34,36,37] capture the nonmagnetic states at $\nu = -1/3, -4/3$, FCI states at $\nu = -2/3$, and the CI state at $\nu = -1$? In this paper, we mainly limit ourselves to the more robust and pronounced $\nu = -2/3$ FCI and focus on explaining this key puzzle and other essential features of the theoretical model. The FCI at $\nu = -3/5$ will be lightly discussed at the end of Sec. V; its appearance is consistent with the initial studies [1–3].

To answer the question, we perform self-consistent Hartree-Fock (HF) and exact-diagonalization (ED) calculations for the experimental angles [24–27] $\theta \in [3.5^\circ, 4.0^\circ]$. We

only focus on the two mainly used sets of parameter values in Refs. [28,29]. As will be discussed, the two other sets of parameters proposed in the literature [36,39] are similar to Ref. [28]. Crucially, we include remote bands in our calculation, but restrict ourselves to at most two bands per valley where the model is thought to be most faithful [28,29].

Our two-band-per-valley (2BPV) HF calculation shows that a CI at $\nu = -1$ occurs for dielectric constants $\epsilon > 10$ using the parameter values in Ref. [29]. The required value of the dielectric constant is considerably larger than $\epsilon \sim 6$ estimated from the h-BN substrate [40]. On the other hand, similar to what was found in Ref. [37], dielectric constants as small as $\epsilon = 5$ yield CIs for the parameters of Ref. [28]. On the other hand, our 1BPV HF gives CI at $\nu = -1$ for dielectric constants as small as $\epsilon = 5$ for both sets of parameters [28,29]; the difference in the 1BPV and 2BPV HF results (most notably for the parameters in [29]) indicates the importance of the remote bands. Despite this enlarged CI region at $\nu = -1$, we do not see clear signatures that the parameters in Ref. [28] can fully capture the experimental phenomena at the fractional fillings of interest, as discussed in the following.

We further perform 1BPV and 2BPV ED calculations for the parameters of Refs. [28,29] for the ϵ range that covers the CI region at $\nu = -1$ in HF calculations (i.e., $\epsilon \in [5, 25]$ for Ref. [28] and $\epsilon \in [10, 25]$ for Ref. [29]).

1BPV ED calculations were performed in Refs. [28,29], and weaker ferromagnetism was found at $\nu = -1/3$ than at $\nu = -2/3$, for values of ϵ yielding FCIs at $\nu = -2/3$. In our 1BPV ED calculations (consistent with Ref. [28] and Ref. [29] on the same system sizes), the parameter values in Ref. [28] require a much stronger interaction ($\epsilon \in [5, 6.25]$) to give FCIs at $\nu = -2/3$ than the parameters in Ref. [29] where ϵ can be as large as 25. References [28,29] found the weaker ferromagnetism at $\nu = -1/3$ concomitant with the $\nu = -2/3$ FCI for 1BVP calculations on 12 unit cells. We further consider 15, 18, and 24 unit cell systems. Though larger system sizes do reduce the difference in ferromagnetic stability between $\nu = -1/3$ and $\nu = -2/3$, we find that the finite size effects are not significant enough to eliminate the trend that ferromagnetism at $\nu = -1/3$ is considerably weaker than that at $\nu = -2/3$. Moreover, at $\nu = -1/3$, we find that the parameters in Ref. [29] mostly give FCIs (similar to the finding in Ref. [29]), while K_M-CDW states are found at $\nu = -1/3$ for the parameters in Ref. [28] (in agreement with experiments and with Ref. [28]). On the other hand, our 1BPV ED results show that when the interaction is strong enough to give FCI at $\nu = -2/3$, $\nu = -4/3$ (not considered in earlier paper) is ferromagnetic and always has a similar or stronger magnetic stability as $\nu = -2/3$, which is inconsistent with the experiments. To resolve this inconsistency, we will include remote bands to the ED calculation.

Our 2BPV ED calculations include one more remote band per valley. Generally, we find that their inclusion typically reduces the spin gaps at $\nu = -1/3$ and $-2/3$ (or even causing a sign change) and changes the spin of the ground state at $\nu = -4/3$. We note that although the remote bands were included in the study of $\nu = -2/3$ in the fully spin-polarized sector in Ref. [36], the effects of remote bands on the spin gap have not yet been studied. In particular for the parameter values in Ref. [29], when FCIs appear at $\nu = -2/3$, the spin gap at $\nu = -1/3$, albeit still fully spin polarized across most of the region, is dramatically reduced, and nearly spin-unpolarized states (i.e., small total spin) are now favored at $\nu = -4/3$. Nevertheless, the ground states at $\nu = -1/3$ are still mostly FCIs when FCIs appear at $\nu = -2/3$. Taken together, the inclusion of remote bands greatly ameliorates the agreement with the experimental phase diagram for the parameters in Ref. [29], although we caution that the ground states at $\nu = -1/3$ are still mostly FCIs and the results are contingent on a dielectric constant $\epsilon > 10$.

On the other hand, the same 2BPV ED calculations for the parameter values in Ref. [28] show large-spin states are energetically favored at $\nu = -4/3$ and (for the system sizes currently accessible to us) have even larger spin-1 gap than that at $\nu = -2/3$ for $\epsilon \in [5, 6.25]$. Thus, we have not seen clear signatures that the parameters in Ref. [28] can capture the significant experimental difference in magnetism between $\nu = -2/3$ and $\nu = -4/3$ for the experimental angles $\theta \in [3.5^\circ, 4.0^\circ]$ for the system sizes currently accessible to us, although $\nu = -1/3$ becomes nonmagnetic and remains not FCIs in agreement with experiments. A summary of our results in comparison to experiment and the literature may be found in Table I.

These results show the need for the analog of the Landau level mixing to explain the experimental facts. Since the single-particle bands have different Chern number sequences depending on the twist angle, the physics of $t\text{MoTe}_2$ is likely to be very rich.

In the rest of this paper, we review the single-particle model in Sec. II and discuss the interaction and the PH symmetry in Sec. III. We further discuss the HF, 1BPV ED, and 2BPV ED results in Secs. IV, V, and VI, respectively. We eventually conclude the paper in Sec. VII, and provide more details in a series of Appendices.

II. SINGLE-PARTICLE MODEL

The moiré physics of the TMDs was originally proposed by Ref. [39] to be captured by a two-valley continuum model formed from low-energy states at the K and K' valleys, where the strong spin-orbit coupling splits the spin-up and spin-down states. By time reversal, the states at valley K have the opposite spin as the states at valley K. Thus spin is effectively locked to valley, and the only global symmetries of the model are charge $U(1)$ and valley/spin (S_z) $U(1)$. Because MoTe_2 is a semiconductor, the effective single-particle moiré Hamiltonian around the quadratic band edge takes the form (in the K valley)

$$H_K(\boldsymbol{r}) = \begin{pmatrix} \frac{\hbar^2\nabla^2}{2m_*} + V_+(\boldsymbol{r}) & t(\boldsymbol{r}) \\ t^*(\boldsymbol{r}) & \frac{\hbar^2\nabla^2}{2m_*} + V_-(\boldsymbol{r}) \end{pmatrix} \tag{1}$$

where the matrix acts on the *electron* wavefunction $(\psi_+(\boldsymbol{r}), \psi_-(\boldsymbol{r}))^T$ with support on momenta near $R(\pm\frac{\theta}{2})\boldsymbol{K}$ in the top/bottom layer [see Fig. 1(a)], $V_\pm(\boldsymbol{r})$ are moiré potentials in the top/bottom layer, and $t(\boldsymbol{r})$ is the interlayer moiré tunneling. Here $R(\theta)$ is a rotation matrix, m_* is the effective mass, and $\boldsymbol{K} = \frac{4\pi}{3a_0}\hat{x}$ is the untwisted K point with $a_0 = 3.52$ Å [39]. Note that ∇^2 is unbounded below and Eq. (1) describes the electron valence bands below the charge neutrality point.

TABLE I. Minimal phase diagram at $\theta \sim 3.7^\circ$ (determined with HF at $\nu = -1$ and ED otherwise). "N-M/W-M" stands for the nonmagentic/weakly magnetic ground states. "Not FCI" stands for the ground states being not FCI ground states. Checkmarks (crosses) indicate a match (mismatch) to experiment for a considerable part of values of ϵ in the indicated range. The question mark indicates an uncertainty due to finite size effects, and "$\approx$ ✓" for $\nu = -4/3$ means a ground state with small (but nonzero) total spin. Citations to earlier work are shown if they are consistent with our work in the same range of parameters. We only consider calculations including *both* valleys, a prerequisite for a prediction of magnetism. Note that Ref. [36] performed two-band ED calculations at $\nu = -2/3$ on a related model with different irreps in the remote bands due to a truncation of the Wannier basis, but only in the fully spin-polarized sector.

$\nu =$	$-1/3$	$-1/3$	$-2/3$	-1	$-4/3$	ϵ
Parameters \ Experiment	N-M/W-M	Not FCI	FCI	CI	N-M	
Ref. [28] param. (1BPV)	✓[28]	✓[28]	✓[28]	✓	✗	[5,6.25]
Ref. [28] param. (2BPV)	✓	✓	?	✓[37]	✗?	[5,6.25]
Ref. [29] param. (1BPV)	✓[29]	✗[29]	✓[29]	✓	✗	[10,25]
Ref. [29] param. (2BPV)	✓	✗	✓	✓	$\approx$ ✓	[10,25]

Spinful time reversal yields the K' valley model $H_{K'}(\boldsymbol{r}) = H_K(\boldsymbol{r})^*$.

A. Moiré potentials

Reference [39] obtained expressions for $V_\pm(\boldsymbol{r})$ and $t(\boldsymbol{r})$ by using the lowest-order symmetry-allowed Fourier modes with parameters fit to bilayer band structures. The point group symmetry of AA-stacked $MoTe_2$ [41,42] is generated by mirror $z \to -z$, threefold rotation about the z axis C_{3z}, twofold rotation about the y axis C_{2y}, and spinful time-reversal $\mathcal{T}$. Note that C_{3z} acts locally on each layer, whereas $C_{2y}\mathcal{T}$ flips the layers. Twisting the layers in opposite directions preserves only the C_{3z} and $C_{2y}\mathcal{T}$ symmetries at the K point, yielding the magnetic point group $3m'$ as the intravalley symmetry group of the moiré model $H_K(\boldsymbol{r})$. Their explicit representations are given in Appendix A.

The interlayer coupling $t(\boldsymbol{r})$ can be expanded in terms of the moiré scattering momentum

$$\boldsymbol{q}_1 = R(\theta/2)\boldsymbol{K} - R(-\theta/2)\boldsymbol{K} = 2\sin\frac{\theta}{2}|\boldsymbol{K}|\hat{y} \tag{2}$$

and $\boldsymbol{q}_{i+1} = R(2\pi/3)\boldsymbol{q}_i$ [43]. Keeping only the lowest order Fourier modes gives

$$t(\boldsymbol{r}) = w\sum_{n=1}^{3} e^{i\boldsymbol{q}_n\cdot\boldsymbol{r}} \tag{3}$$

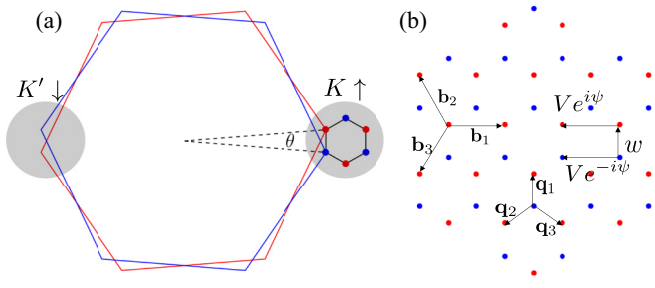

FIG. 1. (a) Twisted BZs of the bilayer, with oppositely spin-polarized low-energy states at K and K'. Twisting creates a moiré BZ shown (for a single valley) in (b) where blue/red represent moiré reciprocal lattice points in the top/bottom layers. The momentum space hoppings $Ve^{\pm i\psi}$, w of the moiré potential are marked.

where C_{3z} ensures all three modes have equal amplitude w. The overall phase of $t(\boldsymbol{r})$ is not observable since it depends on the arbitrary relative phase choice between the top and bottom layers, and is not constrained by $C_{2y}\mathcal{T}$. By convention we take $w < 0$.

Next we consider the potentials $V_\pm(\boldsymbol{r})$. Because they are intralayer, they are supported on the moiré reciprocal lattice spanned by the vectors

$$\boldsymbol{b}_1 = \boldsymbol{q}_3 - \boldsymbol{q}_2 = \sqrt{3}|\boldsymbol{q}_1|\hat{x}, \quad \boldsymbol{b}_2 = R(2\pi/3)\boldsymbol{b}_1 \tag{4}$$

and we define $\boldsymbol{b}_3 = -(\boldsymbol{b}_1 + \boldsymbol{b}_2) = R(2\pi/3)\boldsymbol{b}_2$ for convenience. The lowest-order reciprocal lattice points are $\boldsymbol{0}$ and the first shell $\boldsymbol{G} = R(2\pi n/6)\boldsymbol{b}_1$ for $n = 0, \ldots, 5$. Keeping only these harmonics and imposing $C_{3z}, C_{2y}\mathcal{T}$, the most general form of the potential can be written in terms of an amplitude V and phase ψ as

$$V_\pm(\boldsymbol{r}) = 2V\sum_{n=1}^{3}\cos(\boldsymbol{b}_n\cdot\boldsymbol{r} \pm \psi) \tag{5}$$

up to an overall chemical potential. Figure 1 depicts these next-nearest neighbor hoppings on the momentum space lattice [44].

Within the approximation of keeping the lowest harmonics only, an emergent intravalley pseudo-inversion symmetry of $H_K(\boldsymbol{r})$ appears (see Appendix A). Although the pseudo-inversion can be broken by $C_{3z}, C_{2y}\mathcal{T}$-preserving higher-order terms (see Appendix A), we focus on the original, lowest-order model. As the model stands, the pseudo-inversion symmetry relates $\boldsymbol{k}$ and $-\boldsymbol{k}$ so that the band structures in the K and K' valleys are identical. The *ab initio* calculations in Ref. [29] are in agreement with this to good accuracy.

The values of model parameters have been determined by matching the DFT band structure (either at AA stacking [39] or at commensurate twist angles [28,29,45]), which are summarized in Table II. Among the four sets of parameter values in Table II, the first three sets of parameter values are fairly similar: they exhibit dispersive bands structures [see Fig. 2(a)], peaked quantum geometry, and Ch $= -1$ topology in both bands closest to the charge neutrality per valley (see Appendix A). In contrast, the fourth set of parameter values in Table II is qualitatively different, showing a flatter active band [see Fig. 2(b)], nearly ideal quantum geometry [33,46–50], and opposite Chern numbers Ch $= \pm 1$ for the bands

TABLE II. Proposed parameter values for the single-particle moiré model Eq. (1).

$MoTe_2$	m_* (m_e)	w (meV)	V (meV)	ψ
Ref. [28]	0.62	−13.3	11.2	−91°
Ref. [39]	0.62	−8.5	8	−89.6°
Ref. [45]	0.62	−11.2	9.2	−99°
Ref. [29]	0.6	−23.8	20.8	−107.7°

closest to the charge neutrality per valley. (The larger values of the moiré potential are on par with other transition metal dichalcoginides [51].) Therefore, in the following, we will focus on the first (Ref. [28]) and fourth (Ref. [29]) sets of parameter values in Table II. Since experiments repeatedly show FCIs around the twist angle 3.7°, we also restrict our attention to the range of angles $\theta \in [3.5°, 4°]$. Figure 3 maps out the single-particle phase diagram of the active bands across V, w for two values of ψ proposed in Refs. [28,29], finding three topologically distinct regimes when the lowest two bands are considered. Figure 3 shows that the parameters of Ref. [28] and Ref. [29] fall in different phases, and can be expected to yield different many-body phase diagrams.

We note that Refs. [28] and [29] extracted their parameters from different commensurate twist angles, 4.4° and 3.89° respectively. Thus the parameters used in Ref. [29] are perhaps more reliable for describing the experiments at the angle of 3.7°. Although, it is likely that the model parameters depend on twist angle due to relaxation effects [52,53].

B. Topology

The full magnetic wallpaper group (in one valley) is $p31m'$ (or 157.55 in the BNS setting) generated by $C_{3z}, C_{2y}\mathcal{T}$, and moiré translations. Band structures can be labeled by their C_{3z} eigenvalues at the high-symmetry points Γ_M, K_M, K'_M in the moiré Brillouin zone (BZ) (for a fixed valley). Figure 2 depicts two example band structures. The active (highest valence) band in both cases has the same eigenvalues, but the lower two bands differ by a band inversion at the Γ_M point, as can be seen from the interchange of the Γ_1 and Γ_2 irrep. A minimal character table for the spin-less irreps (we choose $C_{3z}^3 = +1$ since it is intravalley) at the C_{3z}-symmetric points in one valley

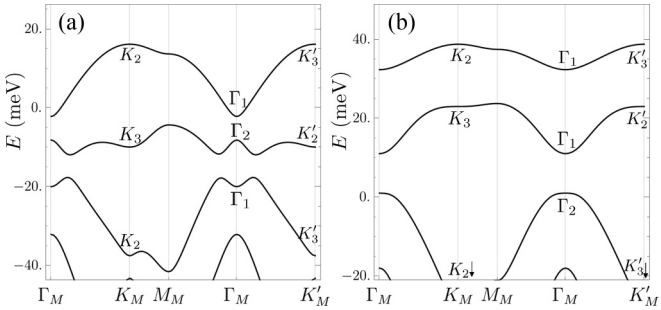

FIG. 2. Single-particle band structures at $\theta = 3.7°$ for the parameters in Ref. [28] (a) and Ref. [29] (b), along with their C_{3z} irreps. In Fig. 3, (a) is marked with a circle and (b) with a star.

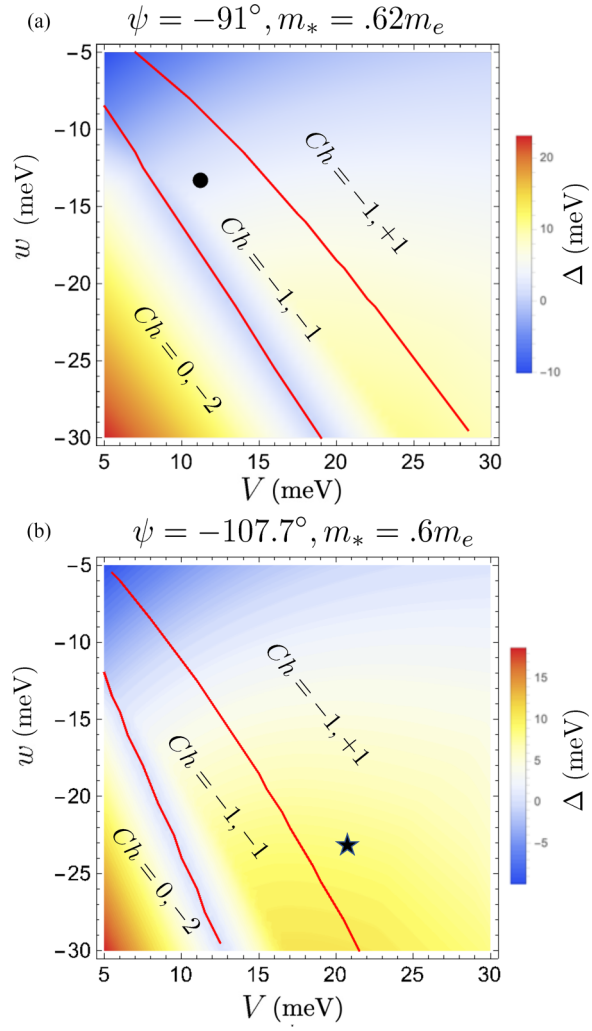

FIG. 3. Single-particle phase diagram at $\theta = 3.7°$. The parameter space of the model contains three topologically distinct phases delineated by direct gap closings (red lines). In each phase, the Chern numbers Ch of the two bands nearest the Fermi energy are labeled and the indirect gap Δ right below the highest valence band is colored. (a) Parameters of Ref. [28] are marked with a black dot. (b) Parameters of Ref. [29] are marked with a black star.

(giving the notation in real space and momentum space) is

$\boldsymbol{r}$	$\boldsymbol{k}$	1	C_{3z}
A	Γ_1, K_1, K'_1	1	1
^2E	Γ_2, K_2, K'_3	1	$e^{\frac{2\pi i}{3}}$
^1E	Γ_3, K_3, K'_2	1	$e^{-\frac{2\pi i}{3}}$

. (6)

We see that all irreps are one dimensional, showing that there are no symmetry-protected degeneracies. Secondly, the Chern number Ch of an individual band is related to the symmetry eigenvalues by [54]

$$\exp\left[\frac{2\pi i}{3}\mathrm{Ch}\right] = \prod_{\boldsymbol{k}=\Gamma_M,K_M,K'_M} \mathcal{D}_{\boldsymbol{k}}[C_{3z}] \tag{7}$$

where $\mathcal{D}_{\boldsymbol{k}}[g]$ is the representation of g at $\boldsymbol{k}$, which can be used to determine Ch mod 3. Lastly, we remark that this space group hosts decomposable elementary band representations (see Appendix A), which generically give rise to Ch =

$\pm 1 \bmod 3$ Chern bands [55,56]. Thus there is a symmetry principle [57] that predicts the appearance of topology.

C. Remarks on the continuous model

According to previous DFT calculations [28,29], the current single-particle model Ref. [39] can faithfully capture the top two bands in the K, K' valleys, but fails farther from the charge neutrality. Specifically, the *ab initio* calculations [29] show low-energy moiré bands from the TMD Γ valley appearing right below the second highest K, K'-valley bands, which are absent from the Hamiltonian. Therefore, in the following sections, we include at most two bands per valley in our calculations. The Γ bands will be studied in our forthcoming paper.

The single-particle Hamiltonian can be written in second quantized notation as

$$H_0 = \int d^2r \sum_{\eta,ll'} c^\dagger_{\eta,l,\boldsymbol{r}} [H_\eta(\boldsymbol{r})]_{ll'} c_{\eta,l',\boldsymbol{r}} \tag{8}$$

where $c^\dagger_{\eta,l,\boldsymbol{r}}$ creates an electron at position $\boldsymbol{r}$ in the lth layer and the η valley. The global symmetries of H_0, as well as the interacting Hamiltonians to be introduced in the following section, are

$$\begin{aligned} N &= \int d^2r \sum_{\eta,l} c^\dagger_{\eta,l,\boldsymbol{r}} c_{\eta,l,\boldsymbol{r}} \\ S_z &= \frac{1}{2} \int d^2r \sum_{\eta,l} \eta c^\dagger_{\eta,l,\boldsymbol{r}} c_{\eta,l,\boldsymbol{r}} \end{aligned} \tag{9}$$

where $\eta = \pm$ denotes the valley ηK quantum number, which is equivalently the spin quantum number $S_z = \eta/2$. In this work, we only consider states with $S_z \geqslant 0$ since those with negative S_z are related by time reversal.

III. INTERACTION AND PARTICLE-HOLE SYMMETRY

We now consider the many-body Hamiltonian obtained from adding the Coulomb interaction to the single-particle model discussed above. We first discuss the different interactions suggested in the literature and then clarify their behavior under particle-hole transformations.

A. Interaction among electrons and holes

In the previous theoretical papers [16,28,29,31,32,34,36,37] on FCIs in $t\text{MoTe}_2$, two different interactions are used. One choice is the Coulomb interaction among holes, employed by Ref. [28] in the full Hamiltonian

$$\begin{aligned} H_h = &\int d^2r \sum_{\eta,ll'} \widetilde{c}^\dagger_{\eta,l,\boldsymbol{r}} [-H_\eta(\boldsymbol{r})]_{ll'} \widetilde{c}_{\eta,l',\boldsymbol{r}} \\ &+ \frac{1}{2} \sum_{l\eta,l'\eta'} \int d^2r d^2r' V(\boldsymbol{r}-\boldsymbol{r}') \widetilde{c}^\dagger_{\eta,l,\boldsymbol{r}} \widetilde{c}^\dagger_{\eta',l',\boldsymbol{r}'} \widetilde{c}_{\eta',l',\boldsymbol{r}'} \widetilde{c}_{\eta,l,\boldsymbol{r}}, \end{aligned} \tag{10}$$

where $\widetilde{c}^\dagger_{\eta,l,\boldsymbol{r}}$ creates a hole at position $\boldsymbol{r}$ in the lth layer and η valley and $V(\boldsymbol{r})$ is the double-gated screened Coulomb potential with gate distance ξ and dielectric constant ϵ (see Appendix B for explicit formulas). Note that $\widetilde{c}^\dagger_{\eta,l,\boldsymbol{r}}$ and $c_{\eta,l,\boldsymbol{r}}$ are related by a complex conjugation operator, i.e., $\widetilde{c}^\dagger_{\eta,l,\boldsymbol{r}} = \mathcal{K} c_{\eta,l,\boldsymbol{r}} \mathcal{K}^{-1}$ with $\mathcal{K}$ the complex conjugate (see Appendix B). H_h annihilates the charge neutrality point $\nu = 0$, which is the hole vacuum. This is because the charge neutrality ($|\nu = 0\rangle$) is the product state of all valence electron bands occupied (all holes unoccupied), which is the maximally filled state in the Hilbert space,

$$|\nu = 0\rangle = \prod_{\boldsymbol{r},\eta,l} c^\dagger_{\eta,l,\boldsymbol{r}} |0\rangle \,, \tag{11}$$

with $c_{\eta,l,\boldsymbol{r}}|0\rangle = 0$, leading to $\widetilde{c}_{\eta,l,\boldsymbol{r}}|\nu = 0\rangle = 0$.

The other choice is the Coulomb interaction among electrons, which is used in Refs. [16,29],

$$\begin{aligned} H_e = &\int d^2r \sum_{\eta,ll'} c^\dagger_{\eta,l,\boldsymbol{r}} [H_\eta(\boldsymbol{r})]_{ll'} c_{\eta,l',\boldsymbol{r}} \\ &+ \frac{1}{2} \sum_{l\eta,l'\eta'} \int d^2r d^2r' V(\boldsymbol{r}-\boldsymbol{r}') c^\dagger_{\eta,l,\boldsymbol{r}} c^\dagger_{\eta',l',\boldsymbol{r}'} c_{\eta',l',\boldsymbol{r}'} c_{\eta,l,\boldsymbol{r}}, \end{aligned} \tag{12}$$

recalling that $c^\dagger_{\eta,l,\boldsymbol{r}}$ creates an electron at position $\boldsymbol{r}$ in the lth layer and the η valley. As is apparent from Eq. (11), the electron interaction H_e does not annihilate $|\nu = 0\rangle$, the state around which the single-particle Hamiltonian was derived,

In our HF and ED calculations, we use a projected Hamiltonian in the band basis. In this basis, H_h can be written as (see Appendix B)

$$H_h = -\sum_{\boldsymbol{k},\eta,n} \widetilde{\gamma}^\dagger_{\eta,n,\boldsymbol{k}} \widetilde{\gamma}_{\eta,n,\boldsymbol{k}} E_{\eta,n}(\boldsymbol{k}) + H_{h,\text{int}} \,, \tag{13}$$

where

$$\begin{aligned} H_{h,\text{int}} = &\frac{1}{2} \sum_{\boldsymbol{k},\boldsymbol{k}',\boldsymbol{q}} \sum_{\eta,\eta'} \sum_{m,m',n',n} V_{\eta\eta',mm'n'n}(\boldsymbol{k},\boldsymbol{k}',\boldsymbol{q}) \\ &\times \widetilde{\gamma}^\dagger_{\eta,m,\boldsymbol{k}+\boldsymbol{q}} \widetilde{\gamma}^\dagger_{\eta',m',\boldsymbol{k}'-\boldsymbol{q}} \widetilde{\gamma}_{\eta',n',\boldsymbol{k}'} \widetilde{\gamma}_{\eta,n,\boldsymbol{k}}, \end{aligned} \tag{14}$$

and $V_{\eta\eta',mm'n'n}(\boldsymbol{k},\boldsymbol{k}',\boldsymbol{q})$ labels the projected interaction and m, m', n', n are the band indices. Note that $-E_{\eta,n}(\boldsymbol{k})$ is the nth hole band energy (which is bounded below) in valley η, and $\widetilde{\gamma}^\dagger_{\eta,n,\boldsymbol{k}}$ creates a hole in the nth hole band in η valley at $\boldsymbol{k}$. The projection of $H_{e,int}$ is analogous (see Appendix B).

We note that if we do not perform the band projection and keep the whole continuous Hamiltonian, H_h [Eq. (10)] and H_e [Eq. (12)] only differ by a chemical potential-like term that is proportional to the particle number operator, which means that the unprojected Eqs. (10) and (12) should give the same results (up to a overall constant) in a fixed particle-number sector. However, in practice, we always keep a finite set of bands, and the projected H_e and H_h are not guaranteed to give the same results in a fixed particle-number sector anymore (see Appendix B). In the rest of this paper, we will always use the projected Hamiltonians with a finite set of bands. Section IV will show that the H_e and H_h give different results at $\nu = -1$ in projected HF calculation.

B. Particle-hole symmetry

Any single Landau level (LL) under the projected Coulomb interaction possesses exact particle-hole (PH) symmetry, which was widely used in study of the fractional quantum Hall effect [58]. However, this is not the case in general for FCIs [59], and we will give a brief summary of the role of particle-hole symmetry in H_h and H_e.

In close analogy to the PH symmetry of a single LL, we consider the following intraband PH transformation

$$\mathcal{C}\gamma^{\dagger}_{\eta,n,\boldsymbol{k}}\mathcal{C}^{-1} = \gamma_{\eta,n,\boldsymbol{k}}\ , \tag{15}$$

where $\mathcal{C}$ is an anti-unitary operator. Under this PH transformation, H_e acquires two extra terms,

$$\mathcal{C}H_e\mathcal{C}^{-1} = H_e + \sum_{\eta,\boldsymbol{k},n}\gamma^{\dagger}_{\eta,n,\boldsymbol{k}}\gamma_{\eta,n,\boldsymbol{k}}(-2E_{\eta,n}(\boldsymbol{k})) + \sum_{\eta,\boldsymbol{k},nm}\gamma^{\dagger}_{\eta,n,\boldsymbol{k}}\gamma_{\eta,m,\boldsymbol{k}}\epsilon_{\eta,nm}(\boldsymbol{k}) + \text{const.}, \tag{16}$$

where $(-2E_{\eta,n}(\boldsymbol{k}))$ accounts for the sign flipping of the single-particle dispersion, and $\epsilon_{\eta,nm}(\boldsymbol{k})$ is an effective one-body term arising from the interaction matrix elements. Its explicit form is given in Appendix B. The hole Hamiltonian H_h transforms similarly, with $\gamma_{\eta,n,\boldsymbol{k}} \to \widetilde{\gamma}_{\eta,n,\boldsymbol{k}}$ and $E_{\eta,n}(\boldsymbol{k}) \to -E_{\eta,n}(\boldsymbol{k})$ in Eq. (16). The case of single LL can be recovered by dropping the valley and band index, and then PH invariance follows from the flat kinetic energy [$E(\boldsymbol{k}) = \text{const.}$] and the flat one-body term [$\epsilon(\boldsymbol{k}) = \text{const.}$] due to the unique LL wavefunction [60], which has uniform quantum geometry [61].

Note that, in the transformation of H_e and H_h, we have kept the number of bands in the projected Hamiltonian fully general. As mentioned at the end of Sec. III A, only a finite number of bands (and spin-valley flavors) can be kept in numerical calculations, and importantly the PH transformation acts differently depending on this truncation. For instance, one could keep only one active band in a single valley (corresponding a fully spin-polarized Hilbert space); in this case, the PH transformation transforms the electron filling ν to $-1-\nu$ (e.g., $-1/3$ to $-2/3$, recalling that ν is the electron filling measured from the charge neutrality point). This case has been studied in Ref. [34], which shows that the PH symmetry is not exact (e.g., the spectra at $-1/3$ and $-2/3$ will not be identical) but might be approximately correct outsides the experimental range of angles considered in this paper.

In this paper, we will consider PH symmetry breaking beyond the fully spin-polarized sector, which is a basic requirement for studying the nonmagnetized states observed in experiment. In particular, if we keep one band in each valley, PH maps ν to $-2-\nu$ (e.g., $-2/3$ to $-4/3$). For this case it is then possible to have approximate PH symmetry between $-2/3$ and $-4/3$. However, if the remote bands are heavily involved in the low-energy physics, they might strongly break any approximate PH symmetry (if it exists) between ν and $-2-\nu$, akin to the situation of the fractional quantum Hall effect at $\nu = 5/2$ [62,63]. Strictly speaking, if we keep two valleys and two bands per valley, we can only have exact PH symmetry between ν and $-4-\nu$. We will see in Secs. V and VI that these effects are indeed relevant for the parameter values in Ref. [29].

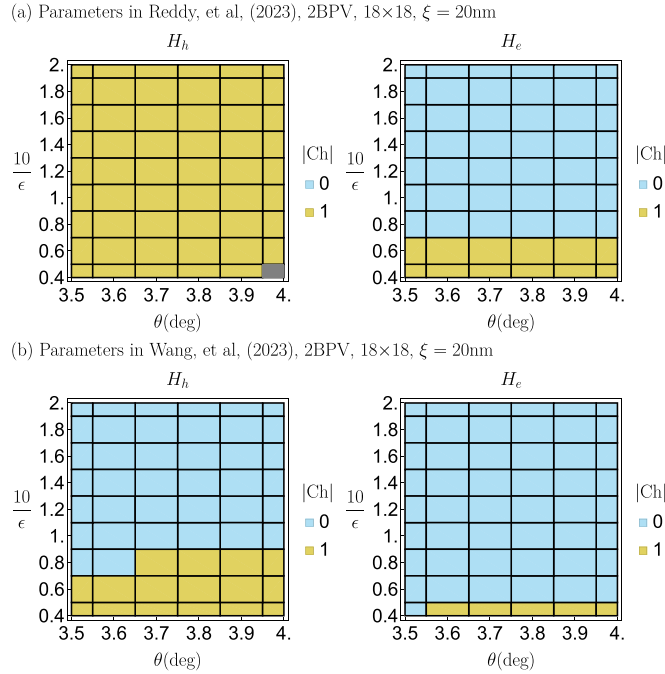

FIG. 4. The 2BPV Hartree-Fock results for $\xi = 20$ nm at $\nu = -1$. H_h and H_e refer to the Hamiltonian used, and Ch refers to the Chern number. The gray region in (a) indicates a *non*ferromagnetic ground state, which is intervalley coherent translationally breaking state with wavevector K_M and which has zero Chern number. 18×18 labels the system size. In general, the system size $L_1 \times L_2$ means that the momenta included in the calculation are $(n/L_1)\boldsymbol{b}_1 + (m/L_2)\boldsymbol{b}_2$ with $n = 0, \ldots, L_1 - 1$ and $m = 0, \ldots, L_2 - 1$, where $\boldsymbol{b}_1$ and $\boldsymbol{b}_2$ are defined in Eq. (4).

IV. SELF-CONSISTENT HARTREE-FOCK CALCULATIONS AT $\nu = -1$

Self-consistent HF calculations at $\nu = -1$ for $t\text{MoTe}_2$ have been performed in previous works [16,27,31,37], among which Refs. [27,30,37] demonstrated different phases induced by band mixing. In this section, we provide HF results at $\nu = -1$ for sets of parameter values in Refs. [28] and [29] for both hole and electron interactions H_h and H_e. These HF calculations will serve to demonstrate the difference between the interactions H_h and H_e and will allow us to screen out the choices of parameters for which no CI appears at $\nu = -1$ in preparation for more time-consuming ED calculations.

As discussed in Sec. II C, we include two bands per valley—the two highest electron bands or two lowest hole bands per valley—as done in Ref. [37]. In the end of this section, we will mention the 1BPV HF results. Our 2BPV HF calculation is different from the 3BPV HF calculations done in Ref. [30], and different from the 2BPV calculation in Ref. [27], which replaces part of the states in the second band in each valley by those in the third band due to Wannierization.

Our 2BPV HF results are summarized in Fig. 4 where we show the phase diagram for the experimentally relevant angles $\theta \in [3.5°, 4.0°]$ and a range of dielectric constants $\epsilon \in [5, 25]$. For both interactions and both parameter values, we find that the ground state is ferromagnetic (fully spin polarized) over

nearly the entire phase diagram. The only exception is the appearance of an intervalley coherent (IVC) translation-breaking state with wavevector K_M, called IVC-K_M [37], which appears at ϵ close to 25 for H_h [grey region in Fig. 4(a)]. We note that although the IVC-K_M state becomes the ground state only at $\theta = 4.0^\circ$ in our (θ, ϵ) mesh for H_h in Fig. 4(a), it has energy very close to the $|\mathrm{Ch}| = 1$ state for smaller angles at $\epsilon = 25$, e.g., for $(\theta, \epsilon) = (3.8^\circ, 25)$, the $|\mathrm{Ch}| = 1$ state only wins over the IVC-K_M state by about 0.1 meV per unit cell. Such IVC-K_M states were also found in Ref. [37] for ϵ close to 25. Intuitively, the translationally invariant IVC state that mixes the lowest-energy bands in the two valleys is not energetically favored because it is topologically obstructed—the opposite Chern numbers of the lowest-energy bands in the two valleys require the order parameter to have zeros [64–67].

Comparing H_h to H_e in Figs. 4(a) and 4(b), the hole interaction H_h in Eq. (13) gives a much larger region where $|\mathrm{Ch}| = 1$, i.e., the CI phase, than H_e. The $\mathrm{Ch} = 0$ region that occurs at stronger interaction for H_e in Fig. 4(a) and for both H_h and H_e in Fig. 4(b) comes from the band inversion between the active band and the remote band in one valley (typically, a single band inversion at K_M or K'_M due to spontaneous breaking of $C_{2y}\mathcal{T}$ in each valley). This effect is only possible due to the inclusion of remote bands, and underscores their importance. Since only $|\mathrm{Ch}| = 1$ is consistent with the CI state observed at $\nu = -1$ [24–27], our HF results suggest that the hole interaction H_h is more suitable to realize CI effect at $\nu = -1$ than H_e.

Notably for H_h, Fig. 4(a) shows that the $|\mathrm{Ch}| = 1$ region persists all the way to $\epsilon = 5$ using the parameters of Ref. [28] (consistent with the results of Ref. [37]) but only to $\epsilon = 10$ for the parameter of Ref. [29]. Lastly, to check the dependence on screening length, we calculated the phase diagrams for two other screening lengths, $\xi = 60$ nm and $\xi = 150$ nm, and find no changes in the CI region for the (θ, ϵ) mesh that we choose though the gap of the CI does increase as the screening length increases (see Appendix C).

As we can see, H_h and H_e lead to different 2BPV HF phase diagrams. While both Hamiltonians were used in the literature, we argue that H_h is the only physically reasonable choice since H_h is normal ordered with respect to the charge neutrality while H_e is not. For this reason, we will not use H_e but will focus on H_h in the remainder of the paper. The CI regions then roughly correspond to $\epsilon \in [5, 25]$ for the parameter values in Ref. [28] and $\epsilon \in [10, 25]$ for the parameter values in Ref. [29].

We also performed the 2BPV HF calculations with the different values of V and w for the twist angle 3.7° and for typical values of ϵ, and found that the CI state is robust as long as V, w do not differ too much from those in Refs. [29] and [28] (see Appendix C).

As a comparison to the 2BPV case, we perform 1BPV HF calculations for H_h at $\xi = 20$ nm, which give CI at $\nu = -1$ for the entire $\theta \in [3.5^\circ, 4.0^\circ]$ and $\epsilon \in [5, 25]$ for both sets of parameters [28,29] (see Appendix C); CI at $\nu = -1$ was also found in the 1BPV HF calculation in Ref. [16] outsides the experimental angle range. So the 1BPV calculations missed the IVC-K_M states for parameters in Ref. [28] and the $\mathrm{Ch} = 0$ states for the parameters in Ref. [29] in the 2BPV results (Fig. 4) indicating the importance of the remote bands.

To summarize, at the level of 2BPV HF at $\nu = -1$, the CI regions of the phase diagram differ considerably for the parameters of Refs. [28] and [29]. To realize the CI phase for the parameters in Ref. [29], roughly $\epsilon \in [10, 25]$ is required, compared to the larger range $\epsilon \in [5, 25]$ for Ref. [28]. We will show in the following section that ED calculations at $\nu = -1/3, -2/3, -4/3$ show a better match to experiment using the parameters of Ref. [29] compared to Ref. [28].

V. ONE-BAND-PER-VALLEY EXACT DIAGONALIZATION CALCULATIONS

1BPV ED calculations have been performed at fractional fillings in previous studies [28,29,31,32,34,36,37] restricting to the top electron band in each valley. In particular, Refs. [28,29] studied the magnetic properties at $\nu = -1/3, -2/3$ within 1BPV ED calculations and found weaker ferromagnetism at $\nu = -1/3$ than that at $\nu = -2/3$. The difference in the magnetic properties between $\nu = -2/3$ and $\nu = -4/3$ was not studied.

In general, a measure of magnetic stability is the spinful gap [28,29], i.e., the energy difference between the lowest-energy state in the $S_z \neq S_{\max}$ sectors and the lowest-energy state with the same particle number in the $S_z = S_{\max}$ (ferromagnetic) sector (former minus latter). Recall that S_z is the total spin of the ground state for which we only consider $S_z \geqslant 0$ owing to the TR symmetry; note that $S_{\max}$ is the spin of the maximally spin-polarized state in the Hilbert space. If the spinful gap is positive (negative), the ground state is (is not) maximally spin polarized. When the ground states are maximally spin polarized, a larger spinful gap means increased stability. We note that in the 1BPV case, a maximally spin-polarized state of a given filling ν is a fully spin-polarized state only if $\nu > -1$. For $\nu < -1$, we cannot have all holes in one valley since one valley has only a single band. Taking $\nu = -4/3$ as an example, even a maximally spin-polarized state has a quarter of the total number of holes in the other valley, i.e., it is not a fully spin-polarized state.

In Appendix D 1, we compare the spinful gaps to the spin-1 gaps for the system sizes of 3×4, 3×5 and 3×6 for both sets of parameters, and find that the spin-1 gap is typically equal to or similar to the spinful gap, where the spin-1 gap is the gap between the lowest-energy state in $S_z = S_{\max} - 1$ sector and that in the $S_z = S_{\max}$ sector (former minus latter) with the same particle numbers. This trend is also shown in Ref. [28] for $\nu > -1$ for system sizes of 12 and 15 unit cells, while we further show it for sizes reaching 3×6. In the rest of this section, we will thus use the spin-1 gap as a proxy for the spinful gap, unless specified otherwise.

Our 1BPV ED calculations were done for four system sizes: 3×4, 3×5, 3×6, and 4×6. We show the main results on 3×6 and 4×6 in Figs. 5 and 6, while leaving 3×4 and 3×5 results to Appendix D. Throughout the paper, we determine the FCI region by the following criterion:

Proposition 1. The system is in the FCI region if (i) the three lowest states are maximally spin polarized, (ii) the momenta of the three lowest states match the momenta of FCI [68,69], and (iii) the spread of the three lowest states is smaller than the gap between the third lowest state and fourth lowest state in maximally spin-polarized sector.

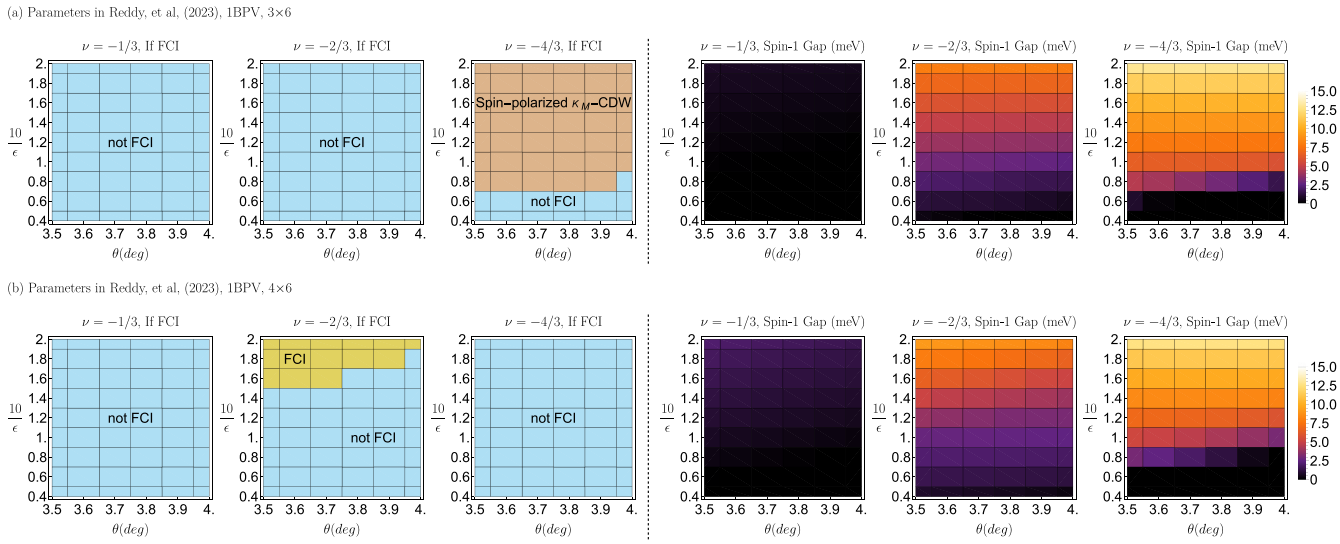

FIG. 5. 1BPV ED calculations on H_h for parameter values in Ref. [28] on 3×6 (a) and 4×6 (b) systems. 3×6 in (a) and 4×6 in (b) stand for different system sizes. In the left most three figures of (a), (b), green ("FCI") labels the region that satisfies the criterion in Prop. 1, and blue ("not FCI") means that we do not see clear signatures of FCI or maximally spin-polarized CDW. For $\nu = -4/3$ in (a) for the system size of 3×6, 1BPV results show that the system is in a maximally spin-polarized K_M-CDW phase for relatively large interaction (brown) and for experimental angles $\theta \in [3.5^\circ, 4.0^\circ]$; the K_M-CDW phase is suppressed for the system size of 4×6 since its momentum mesh do not include the K_M or K'_M point. The rightmost three figures of (a) and (b) give the spin-1 gaps, which are shown with the same color scale for all plots. If the spin-1 gap is negative, it is set to zero in the plot.

We note that Prop. 1 is a necessary condition for FCI states. In addition to this criterion, we will also probe the quality of FCI based on the standard deviation of the particle density in the momentum space—perfect FCI states have uniform particle density in the momentum space (zero standard deviation).

As shown in Figs. 5 and 6, the finite-size effects on the FCI region at $\nu = -2/3$ are non-negligible. Hence we choose the largest system size 4×6 to determine the $\nu = -2/3$ FCI region, which is roughly $\epsilon \in [5, 6.25]$ for the parameters in Ref. [28] and nearly the whole phase diagram for the parameters of Ref. [29]. Based on the particle density in the momentum, we find that the quality of the FCI states in the $\nu = -2/3$-FCI region are much worse for the parameters in Ref. [28] (standard deviation of particle density larger than 0.136) than that for Ref. [29] (standard deviation of particle density can be as small as 0.002). In the "not FCI" regions of Figs. 5 and 6, we did not see clear signatures for FCI or maximally spin-polarized CDW, and the signature of metal is

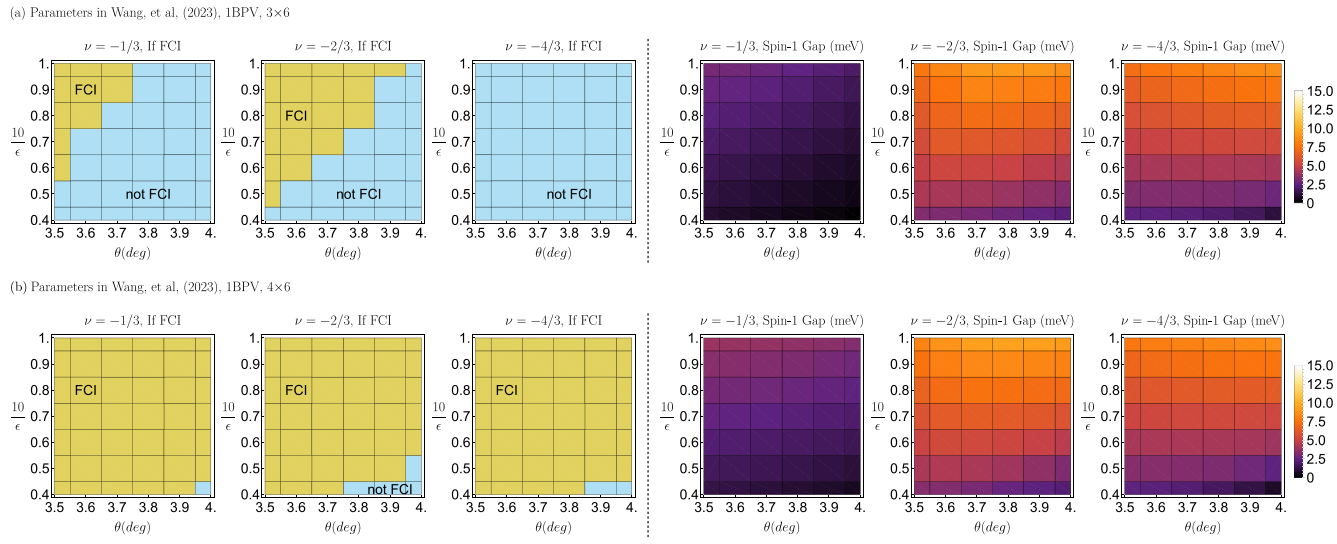

FIG. 6. 1BPV ED calculations on H_h for parameter values in Ref. [29] on 3×6 (a) and 4×6 (b) systems. In the leftmost three plots of (a) and (b), green ("FCI") labels the region that satisfies the criterion in Prop. 1, and blue ("not FCI") means that we do not see clear signatures of FCI or maximally spin-polarized CDW. The rightmost three plots of (a) and (b) given the spin-1 gaps, which are shown with the same color scale for all plots. If the spin-1 gap is negative, it is set to zero in the plot. In the "not FCI" region, the properties of the ground state(s) (other than the momentum and spin polarization) are not conclusively determined.

also not clear enough (perhaps due to finite-size effect). (See Appendix D for details.)

In the parameter region where $\nu = -2/3$ hosts FCIs, the 1BPV ED calculation shows that the ground states at $\nu = -1/3$, $-2/3$, and $-4/3$ all exhibit a positive spin-1 gap, indicating maximally spin-polarized ground states. We note that although the finite-size effect in the FCI region is considerable, the finite-size effect of the spin-1 gap is small as the spin-1 gap does not change significantly for all four system sizes we consider (see Appendix D 2 for full details). We now compare the magnetic stability of the ground states at different fillings.

We compare $\nu = -4/3$ to $\nu = -2/3$ first. In the FCI region for $\nu = -2/3$, the filling fraction $\nu = -4/3$ is in a maximally spin-polarized charge density wave phase with wavevector K_M (noted as K_M-CDW) for the parameter values in Ref. [28] (see Fig. 26 of Appendix D), while $\nu = -4/3$ is mostly in the FCI phase for the parameter values in Ref. [29] (see Fig. 30 of Appendix D). As shown in Fig. 5, the spin-1 gap at $\nu = -4/3$ is larger than that at $\nu = -2/3$ for the parameter values in Ref. [28], indicating more robust magnetism in the former than the latter, which is contrary to the experiment. Specifically, in the $\nu = -2/3$ FCI region, the ratio of the spin-1 gap at $\nu = -4/3$ and $\nu = -2/3$ takes a value in the range [1.59,1.72] for 3×4, [1.49,1.59] for 3×5, [1.62,1.77] for 3×6, and [1.37,1.64] for 4×6. In comparison, the same ratios for Ref. [29] are in [0.60,0.92] for 3×4, [0.61,0.93] for 3×5, [0.74,1.00] for 3×6, and [0.71,0.93] for 4×6. In the top left corner of the phase diagram ($\theta \in [3.5^\circ, 3.7^\circ]$ and $10/\epsilon \in [0.8, 1.0]$), the similar spin-1 gaps (shown in Fig. 6) for the parameter values in Ref. [29] can be understood from the approximate PH symmetry between $\nu = -4/3$ and $\nu = -2/3$ in this 1BPV case, as discussed in Sec. III B and Appendix D 3. Thus, within the 1BPV approximation for existing models [28,29], these results show that not only are the many-body states found at $\nu = -4/3$ magnetic, but that their magnetism is far from being significantly less robust than that of the FCI at $\nu = -2/3$. This should be contrasted with the nonmagnetic state at $\nu = -4/3$ and the magnetic FCI at $\nu = -2/3$ observed in the experiments [24–27].

On the other hand, comparing $\nu = -1/3$ and $\nu = -2/3$, we find that the spin-1 gap at $\nu = -1/3$ is indeed considerably smaller than that at $\nu = -2/3$ for both sets of parameter values. Reference [28] finds an order-of-magnitude difference between spinful gaps at $\nu = -1/3$ and $\nu = -2/3$ for the system size of 12 unit cells at $\theta = 3.5^\circ$ and $\epsilon = 5$, which is consistent with our 3×4 results on both spinful and spin-1 gaps (see Appendix D 4). Reference [29] finds the spinful gap at $\nu = -2/3$ is about five times that at $\nu = -1/3$ for $\theta = 3.5^\circ$, $\epsilon = 15$ and the system size of 3×4, which is also consistent with our 3×4 results on both spinful and spin-1 gaps (see Appendix D 4). (Reference [28] also studied the spinful gap at 15 unit cells, but for interaction strengths that do not give FCIs within the experimentally relevant angle region; nevertheless, their results are consistent with our 3×5 results.) We find that increasing the system size reduces the difference in the magnetic behavior between $\nu = -1/3$ and $\nu = -2/3$, but this difference still remains considerable (see Appendix D 4 for more details).

Although the spin properties at $\nu = -1/3$ are consistent with the nonmagnetic/weakly magnetic states observed at $\nu = -1/3$ in experiments, the FCI states at $\nu = -1/3$ given by the parameters in Ref. [29] are not consistent with the experimental signatures at $\nu = -1/3$ pointing toward a topologically trivial state, as opposed to the K_M-CDW states given by the parameters in Ref. [28].

In summary, the spin-1 gap 1BPV ED results indicate that the magnetic stability at $\nu = -4/3$ is far from being significantly weaker than that at $\nu = -2/3$, which is inconsistent with the experiments, whereas the difference between $\nu = -1/3$ and $\nu = -2/3$ is consistent with the nonmagnetic or weakly ferromagnetic states at $\nu = -1/3$ in experiments. Besides $\nu = -1/3, -2/3, -4/3$, we also studied $\nu = -3/5$ in 1BPV ED calculations with parameters in Ref. [29], as discussed in Appendix D 5. We find robust FCI states with large spin-1 gaps (e.g., $\sim$4 meV for $\epsilon = 16.67$ and $\theta = 3.7^\circ$) for experimental relevant angles $\sim 3.7^\circ$. We note that although FCI states at $\nu = -3/5$ were studied in Ref. [34]; Ref. [34] did not show the existence of them for experimentally relevant angles $\sim 3.7^\circ$ and did not study the spin properties.

In the following, we will show that our 2BPV calculations, which include one additional band per valley, the spinful and/or spin-1 gaps are reduced at $\nu = -1/3$ and $-2/3$ (even having sign changes) and the spin of the ground state at $\nu = -4/3$ is greatly changed. In this 2BPV case, we can capture the difference between $-2/3$ and $-4/3$ only for the parameter values in Ref. [29]. In addition, the difference in the stability of magnetism between (the weakly magnetic) $\nu = -1/3$ state and (the robustly magnetic) $\nu = -2/3$ state increases for both sets of parameter values.

VI. TWO-BAND-PER-VALLEY EXACT DIAGONALIZATION CALCULATIONS

We perform 2BPV ED calculations to study $\nu = -1/3$, $\nu = -2/3$ and $\nu = -4/3$ for $\xi = 20$ nm and for the hole interaction in Eq. (13). We will first discuss $\nu = -1/3$ and $\nu = -2/3$, and then compare $\nu = -4/3$ to $\nu = -2/3$. We note that although the remote bands were included in the fully spin-polarized sector in Ref. [36], the effect of remote bands in spinful calculations have not yet been considered. Our 2BPV calculations will involve the systems sizes of 3×3, 3×4, and 3×5, since the partially spin-polarized and spin-unpolarized sectors at larger sizes have very large Hilbert dimensions (taking 3×6 as an example, the $S_z = S^{\max}_{\text{2BPV}} - 1$ sector at $\nu = -2/3$ has Hilbert space dimension about 1.2×10^9 per momentum).

A. $\nu = -1/3$ and $\nu = -2/3$

In our 3×4 2BPV calculations, the spin-1 gaps are considerably larger than the spinful gaps for $\nu = -1/3$, although the spin-1 gap is a good approximation of the spinful gap for $\nu = -2/3$ (see Appendix E). The spinful gap being smaller than the spin-1 gap at $\nu = -1/3$ implies that the spin-zero states actually have lower energy than the partially spin-polarized ($S_z = 1$) states, since we only have three possible values $|S_z| = 0, 1, 2$ at $\nu = -1/3$ at the system size of 3×4. Therefore, we will compare the spinful gaps at $\nu = -1/3$ and

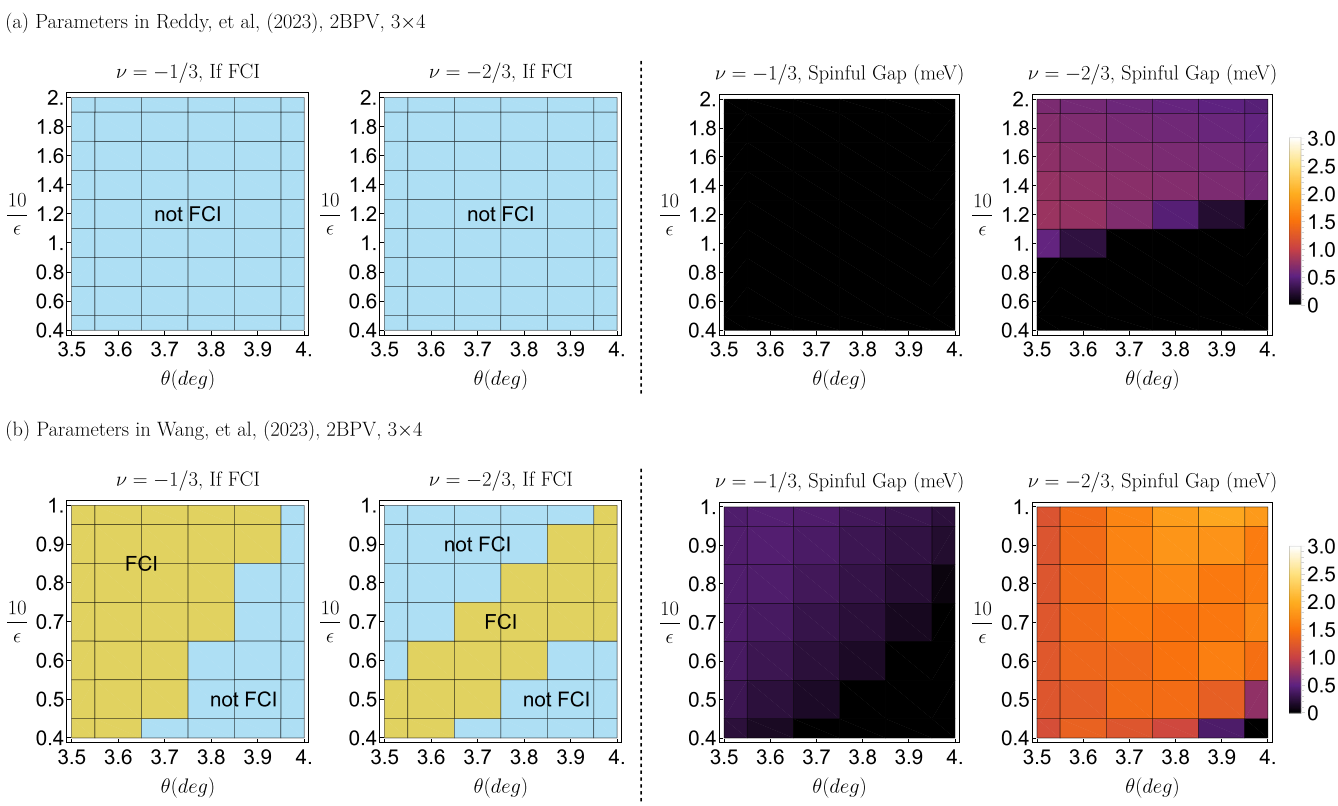

FIG. 7. 3×4 2BPV ED calculation at $\nu = -1/3, -2/3$ for the parameter values in Refs. [28,29] using H_h in Eq. (13). In the leftmost two plots of each row, green ("FCI") labels the region that satisfies the criterion in Prop. 1, and blue ("not FCI") means that we do not see clear signatures of FCI or maximally spin-polarized CDW. In rightmost two plots of (a) or (b), the spinful gap is shown with the same color functions for all plots. Conventions are the same as in Figs. 5 and 6.

$\nu = -2/3$ as shown in Fig. 7. By comparing to the spinful gaps at the system size 3×4 in the 1BPV case (see Appendix D), we can see that including one extra band per valley generally decreases the spinful gaps (and spin-1 gaps) at both fillings. For example, the spinful gap at $\nu = -2/3$ does not exceed 2 meV in the 2BPV case, while it can be as large as $\sim$8 meV with 1BPV.

For the parameter values in Ref. [28], we see the absence of FCIs at $\nu = -2/3$ in Fig. 7(a) for the 3×4 system size. However, we cannot exclude the possibility that this is due to finite-size effects, because for the same parameters, the FCI also does not appear in the 1BPV calculation for the 3×4 system size (see Appendix D). If we change the system size to 3×5 at $(\theta, \epsilon) = (3.7°, 5)$, the ground state at $\nu = -2/3$ is still not an FCI.

The magnetic properties appear to not be afflicted by finite size effects. At $(\theta, \epsilon) = (3.7°, 5)$, the ground state at $\nu = -1/3$ is spin unpolarized on 3×4 systems [Fig. 7(a)] and is minimally polarized for 3×5 (the total spin cannot be zero for five holes), and the spin-1 gaps at $\nu = -2/3$ are similar for the system sizes of 3×4 and 3×5 (0.56 meV and 0.75 meV respectively, see Appendix E). Therefore, we can see the spin properties here are much more robust against finite-size effects than the FCI phase boundary at $\nu = -2/3$. In particular, for interaction strengths $\epsilon \in [5, 6.25]$ (i.e., $10/\epsilon \in [1.6, 2]$, which can give FCIs at $\nu = -2/3$ in 1BPV 4×6 calculations), the zero-spin ground states at $\nu = -1/3$ and the maximally spin-polarized ground states at $\nu = -2/3$ on the 3×4 systems [Fig. 7(a)] for the parameters of Ref. [28] are consistent with the nonmagnetic/weakly ferromagnetic $\nu = -1/3$ and magnetic $\nu = -2/3$ in experiments [24–27] after adding the remote bands. Furthermore, the absence of the FCI states at $\nu = -1/3$ is also consistent with experiments.

For the parameter values in Ref. [29], FCI states at $\nu = -2/3$ are clearly present in a considerable "diagonal-shaped" parameter region in the phase diagram for the 3×4 system size, as shown in Fig. 7(b). The quality of the FCI states deep in the $\nu = -2/3$ FCI region is very good (standard deviation of particle density can be as small as 0.006 compared to the filling $|\nu| = 2/3 \approx 0.67$). (See Appendix E 2 for details.) Compared to the $\nu = -2/3$ FCI region for the 1BPV case in Fig. 25(a) for the 3×4 system size (Appendix D), the remote bands suppress the FCI at larger interaction when fixing the twist angle, which is consistent with the remote bands suppressing CIs at $\nu = -1$ at larger interaction shown in Fig. 4. The diagonal shape of FCI region at $\nu = -2/3$ is consistent with the experimental report [26] of $\nu = -2/3$ FCIs at $\theta = 3.7°$ but not at $\theta = 3.5°$ and $\theta = 3.9°$. The fully spin-polarized 2BPV calculation in Ref. [36] finds that the largest-gap FCI at $\nu = -2/3$ occurs at a larger angle for a stronger interaction outside the experimental angle region $\theta \in [3.5°, 4.0°]$, which shows the same trend as our results.

Among the 18 points in the phase diagram Fig. 7(b) that give FCIs at $\nu = -2/3$ on 3×4 systems, there is one point that favors spin-unpolarized (i.e., spin zero) ground states at $\nu = -1/3$. For the other 17 points, we find fully

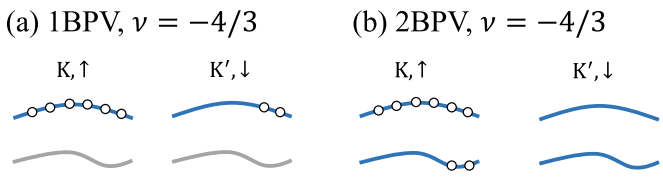

FIG. 8. Schematic plots of maximally spin-polarized states in the 1BPV (a) and 2BPV (b) cases, respectively, for six unit cells. The remote bands (gray) are frozen in (a), and the configuration in (b) is fully spin polarized. We note that the case of (a) is allowed in the 2BPV case as a partially spin-polarized state.

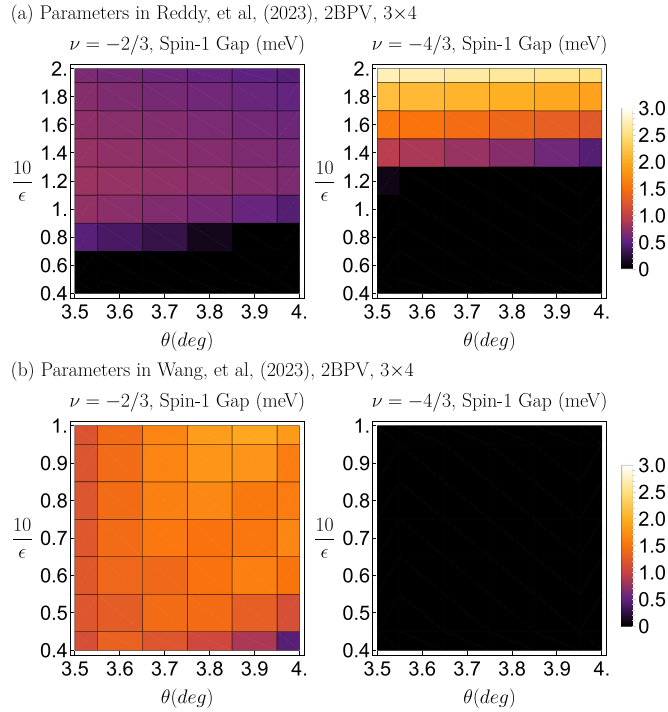

FIG. 9. Spin-1 gaps for 3×4 2BPV at $\nu = -2/3, -4/3$ for parameter values in Ref. [28] (a) and Ref. [29] (b) using H_h. The spin-1 gap is shown with the same color functions for all plots. If the spin-1 gap is negative, we set it to zero in the plots.

spin-polarized ground states at $\nu = -1/3$ (FCI states for 11 of them), but ratio between the spinful gaps at $\nu = -1/3$ and $\nu = -2/3$ (former divided by latter) takes roughly uniform values in $[0.03, 0.27]$ (see Appendix E for details). Therefore, when $\nu = -2/3$ features a fully spin-polarized FCI, the state at $\nu = -1/3$ is either spin unpolarized (at one point) or more often is fully spin polarized with magnetic stability much weaker than that at $\nu = -2/3$. This magnetic property is consistent with the experiments. However, the ground states at $\nu = -1/3$ are still mostly FCIs, which are inconsistent with the experiments. We emphasize that the results here rely on $\epsilon > 10$ within $\epsilon \in [5, 25]$. In fact, a weaker magnetic stability (i.e., smaller spinful gap) at $\nu = -1/3$ tends to happen at larger ϵ values when fixing the twist angle as shown in Fig. 7(b) and in Appendix E.

B. $\nu = -4/3$ versus $\nu = -2/3$

At $\nu = -4/3$, the spinful gap is difficult to calculate for a 3×4 system due to the large Hilbert space dimension, which is $\sim 4.5 \times 10^{10}$ per momentum in the spin-zero sector. (The largest Hilbert space dimension per spin per momentum in our 2BPV calculations is about 1.09×10^8.) Therefore, we can only compare the spin-1 gap at $\nu = -4/3$ to the spin-1 gap at $\nu = -2/3$ on the 3×4 system.

There is a subtlety regarding the spin-1 gap in the 2BPV case. Unlike for $\nu = -1/3$ and $\nu = -2/3$, the maximally spin-polarized state for $\nu = -4/3$ is different in the 1BPV and 2BPV approximations: The maximally spin-polarized state ($S_z = S_{\text{max}}^{\text{1BPV}}$) at $\nu = -4/3$ in the 1BPV case corresponds to a partially spin-polarized state in the 2BPV case as schematically shown in Fig. 8(a). This partially spin-polarized sector at $\nu = -4/3$ has the same total spin as the maximally spin-polarized states at $\nu = -2/3$: it might potentially host FCIs if the remote bands are negligible as shown in the 1BPV calculations in Fig. 6. But the 2BPV case allows for fully spin-polarized states ($S_z = S_{\text{max}}^{\text{2BPV}}$) $\nu = -4/3$ as depicted in Fig. 8(b). Since the remote bands also have nonzero Chern numbers, this situation might also potentially lead to an FCI phase, namely the product of a CI and a Laughlin-like FCI (potentially with an opposite chirality for two sets of parameters in Refs. [28,29] since they have opposite Chern numbers in the remote bands).

The spin-1 gap at $\nu = -4/3$ is the energy difference between the lowest-energy states in the $S_z = S_{\text{max}}^{\text{2BPV}}$ and $S_z = S_{\text{max}}^{\text{2BPV}} - 1$ sectors, which we first focus on for system sizes of 3×4 and 3×5. Note that even if the spin-1 gap is negative, it is conceivable that partially spin-polarized states like Fig. 8(a) might still be favored at $\nu = -4/3$ in the 2BVP calculation. However, the Hilbert space dimension of the partially spin-polarized states in Fig. 8(a) is beyond our computational capabilities for 3×4 (dimension $\sim 2.4 \times 10^9$ per momentum) and 3×5 (dimension $\sim 1.5 \times 10^{12}$ per momentum) systems and thus will be addressed later in this part by considering smaller 3×3 systems.

As shown in Fig. 9(a) for the parameters in Ref. [28], our 2BPV ED results point toward a spin-1 gap at $\nu = -4/3$ that is larger than the one at $\nu = -2/3$, when the interaction is strong enough ($\epsilon \in [5, 6.25]$) to give an FCI at $\nu = -2/3$ in 1BPV 4×6 calculations. We also see this larger spin-1 gap at $\nu = -4/3$ on 3×5 systems (see Appendix E 1), which seems to suggest that the large-spin states are favored at $\nu = -4/3$. For the parameters of Ref. [29], Fig. 9(b) shows that the ground states are not fully spin-polarized at $\nu = -4/3$; this trend persists to the system size of 3×5 as discussed in Appendix E 2.

To address the subtlety of partially spin-polarized states of Fig. 8(b), we resort to the 3×3 system. For the parameters in Ref. [28] and 3×3 systems, the large-spin states ($S_z = S_{\text{max}}^{\text{2BPV}}, S_{\text{max}}^{\text{2BPV}} - 1$ with $S_{\text{max}}^{\text{2BPV}} = 6$) are indeed strongly favored (see Appendix E) at $\nu = -4/3$, though the spin-1 gap at 3×3 becomes negative. (For comparison, the fully spin-polarized states at $\nu = -2/3$ have $S_z = 3$.) The preference for large-spin states at $\nu = -4/3$ is inconsistent with experiment [24–27]. For the parameters in Ref. [29], the 3×3 system has a similar FCI region at $\nu = -2/3$ and similar spinful gap at $\nu = -2/3$ and $\nu = -4/3$ as those of the system size 3×4, as

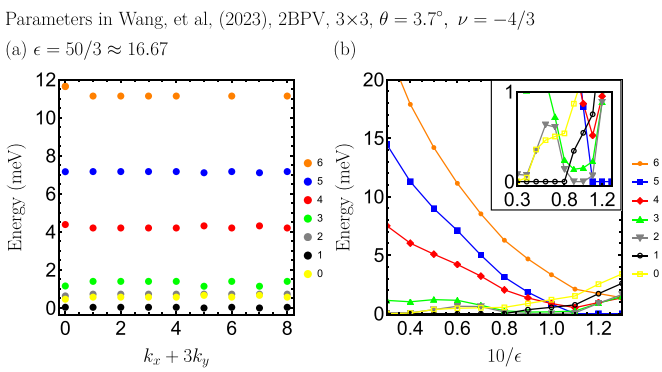

FIG. 10. (a) The 2BPV many-body energy spectrum for the parameters in Ref. [29] at $\theta = 3.7°$ and $\epsilon = 50/3 \approx 16.67$ and $\nu = -4/3$. Here we only include the lowest-energy state in per momentum and spin sector. The energy of the ground state is set to zero. (b) At each value of ϵ, we show the lowest energy of each spin sector for the parameters specified in the plot. As a comparison, the total spin of the fully spin-polarized state at $\nu = -2/3$ is $|S_z| = 3$ for the size of 3×3. The energy of the ground state is set to zero at each value of ϵ. k_x and k_y are defined as $\boldsymbol{k} = (k_x/L_1)\boldsymbol{b}_1 + (k_y/L_2)\boldsymbol{b}_2$, where $L_1 \times L_2$ is the system size, and $\boldsymbol{b}_1$ and $\boldsymbol{b}_2$ are defined in Eq. (4).

shown in Appendix E. The 3×3 results in Fig. 10 show that for $\theta = 3.7°$, the partially spin-polarized $S_z = 3$ states (which have the same spin as the 1BPV maximally spin-polarized states at $\nu = -4/3$ and as the fully spin-polarized state at $\nu = -2/3$) are not favored at $\nu = -4/3$ for the interaction strengths that give FCIs at $\nu = -2/3$ (roughly $10/\epsilon = 0.5 \sim 0.7$ at $\theta = 3.7°$). Instead it is the small-spin ($S_z = 0, 1$) states that dominate at $\nu = -4/3$, in agreement with experiments [24–27]. As the ground states at $\nu = -2/3$ are always fully spin polarized ($S_z = 3$) up for $\epsilon \in [10, 25]$ at $\theta = 3.7°$, the fact that the ground states never have $S_z = 3$ in Fig. 10 indicates the clear breaking of the approximate PH symmetry owing to the remote bands for the parameters in Ref. [29].

Finally, we would like to argue that the bands beyond 2BPV should be negligible. To show this, we use $\nu = -4/3$ as an example since it has larger hole fillings than $\nu = -1/3$ and $-2/3$ and thus is more likely to be affected by the bands beyond 2BPV. As discussed in Appendix E, the 3×3 calculations show that the weight of the low-energy states in the second bands in both valleys is about $0.1 \sim 0.3$ (with even lower occupations for S_z values close to zero), which is not negligible yet significantly smaller than the weight in the first bands ($0.7 \sim 0.9$). Such significant decrease means that the bands beyond 2BPV (including the Γ-valley bands as shown in Ref. [29]) should have negligible effects, even if they are included.

C. Summary of 2BPV results

After including remote bands, the parameters in Ref. [29] exhibit mostly a fully spin-polarized state at $\nu = -1/3$ with significantly weakened magnetic stability than that at $\nu = -2/3$ while maintaining spin-polarized FCI states at $\nu = -2/3$, which is consistent with the experiments. These parameters can also capture the observed difference between $\nu = -4/3$ and $\nu = -2/3$. Nevertheless, the fit to the experimental phase diagram relies on a weaker interaction, namely $\epsilon \geqslant 10$, and the predicted ground states at $\nu = -1/3$ are mostly FCIs, which are not consistent with experiments.

For the same system sizes, the parameter values in Ref. [28] are able to capture the difference in magnetism between $\nu = -1/3$ and $\nu = -2/3$ and the trivial ground states at $\nu = -1/3$, but we have not seen clear indications that they capture the difference between $\nu = -4/3$ and $\nu = -2/3$. We find that the desired FCI phase at $\nu = -2/3$ is missing, although this is possibly due to finite-size effects.

VII. CONCLUSIONS

We have studied the continuum moiré model in Ref. [39], including remote bands in our HF and ED calculations. We performed a comparative study of the parameter values in both Refs. [28] and [29]. For the experimental twist angles $\theta \in [3.5°, 4.0°]$, the 2BPV HF and ED calculations using the parameters of Ref. [29] show FCIs at $\nu = -2/3$, CIs with the quantum anomalous Hall effect at $\nu = -1$, fully spin-polarized states at $\nu = -1/3$ with much weaker stability than that at $\nu = -2/3$, and weakly magnetic (very small total spin) states at $\nu = -4/3$. Therefore, the magnetic phenomenology is agreement with experiments, provided that a dielectric constant of $\epsilon > 10$ (larger than $\epsilon \sim 6$ estimated from h-BN [40]) can be accounted for. However, for the region of the phase diagram compatible with a FCI state at $\nu = -2/3$, the ground states at $\nu = -1/3$ given by the parameters of Ref. [29] are mostly FCIs, which are inconsistent with experiments. On the other hand, we have not succeeded in capturing the significant difference in magnetism between $\nu = -2/3$ and $\nu = -4/3$ with the parameter values in Ref. [28] for the experimental angles $\theta \in [3.5°, 4.0°]$ and $\epsilon \in [5, 25]$.

Our results suggest that the key new magnetic features (beyond the usual FCI [1–3] phases) of the experimental phase diagram depend on remote bands. Our study demonstrates that the minimal model first proposed in Ref. [39] with the parameters of Ref. [29] is a reasonable starting point for describing the realistic phase diagram of $t\text{MoTe}_2$, although it still mostly gives FCI ground states at $\nu = -1/3$ and it needs a larger value of the dielectric constant ϵ than estimated values in bulk h-BN. A precise estimation of ϵ is important for distinguishing different theoretical models, which we leave for future work. One potential explanation for a weaker interaction could lie in modifications of the minimal model of Ref. [39]. In materials like graphene, lattice relaxation [52,53,70–72] and strain [73–79] are understood to play a key role in extending the original Bistrizter-MacDonald model [43]. Such an effect is a typical feature of moiré engineering [80–85]. They lead to higher order terms in the single-particle model that could increase the bandwidth, effectively shrinking the interaction strength. Our results are obtained with HF and ED calculations; it is interesting to study the magnetism with other numerical methods such as determinantal quantum Monte Carlo [86,87].

The now-accessible cornucopia of moiré platforms and tuning parameters promises to enrich the already large family of FCI states [88–93], further supported by the experimental characterization of lattice effects in fractional quantum Hall systems [94–97]. The successful prediction of these more

exotic FCI phases in addition to other material platforms rests on a faithful model of the underlying Hamiltonian. To that end, we have shown that multiband physics plays a crucial role in $t\mathrm{MoTe}_2$, and that its inclusion can accurately hew out the FCI region of the experimental phase diagram.

ACKNOWLEDGMENTS

The authors thank Allan H. MacDonald, Kin-Fai Mak, Jie Shan, and Xiaodong Xu for helpful discussions. Especially, the authors thank Xiaodong Xu for private communication on the weakly magnetic states at $\nu = -1/3$. N.R. is grateful to Valentin Crépel for fruitful discussions. J.Y. thanks Yang Ge, Yves H Kwan, Ramanjit Sohal, Tiancheng Song, Prashant Kumar, Pengjie Wang, and Yang Zhang for helpful discussions. J.H.-A. is appreciative of stimulating discussions with Jiaqi Cai and Trithep Devakul. M.W. and O.V. thank Xiaoyu Wang for helpful discussions. This work is partly supported by a project that has received funding from the European Research Council (ERC) under the European Unions Horizon 2020 Research and Innovation Programme (Grant Agreement No. 101020833). B.A.B.'s work was primarily supported by the DOE Grant No. DE-SC0016239, the Simons Investigator Grant No. 404513. N.R. also acknowledges support from the QuantERA II Programme that has received funding from the European Unions Horizon 2020 research and innovation programme under Grant Agreement No. 101017733. O.V. was funded by the Gordon and Betty Moore Foundation's EPiQS Initiative Grant No. GBMF11070, National High Magnetic Field Laboratory through NSF Grant No. DMR-1157490 and the State of Florida. J.H.-A. is supported by a Hertz Fellowship, with additional support from DOE Grant No. DE-SC0016239 by the Gordon and Betty Moore Foundation through Grant No. GBMF8685 towards the Princeton theory program, the Gordon and Betty Moore Foundations EPiQS Initiative (Grant No. GBMF11070), Office of Naval Research (ONR Grant No. N00014-20-1-2303), BSF Israel US Foundation No. 2018226 and NSF-MERSEC DMR. J.Y. is supported by the Gordon and Betty Moore Foundation through Grant No. GBMF8685 towards the Princeton theory program.

APPENDIX A: SINGLE-PARTICLE MODELS

In this Appendix, we discuss the single-particle continuum models of the twisted transition metal dichalcogenides (TMD) homobilayer Hamiltonians with an emphasis on their symmetries and topology.

1. Momentum space model

In TMD materials, strong spin-orbit coupling breaks spin $SU(2)$ and leads to spin polarization: The low-energy states in the K valley are spin polarized, and those in the K′ valley are oppositely spin polarized by spinful time-reversal symmetry. Thus the full TMD Hamiltonian only has $U(1)$ valley symmetry (locked to spin), and no $SU(2)$ spin symmetry.

This paper focuses specifically on twisted MoTe_2. The bulk material typically grows in the 2H configuration [41] although other configurations are possible [98,99]. When exfoliated down to a monolayer (1H), this configuration results in a gapped 2D band structure with peaked and opposite Berry curvature in each valley due to explicit inversion symmetry breaking from the Te atom positions. (Note that the 1H monolayer band gap is opened due to a trivial inversion-breaking mass, so the model is not a topological insulator [41]). The band near the K, K' points are well described by a gapped Dirac Hamiltonian written in the orbital basis of the Mo d electrons [39]. Explicitly, the $k \cdot p$ theory near the K point is $v_F \boldsymbol{k} \cdot \boldsymbol{\sigma} + \frac{1}{2}\Delta\sigma_3$ where $\Delta \sim 1$ eV is the gap, and the basis is $d_{z^2}, d_{x^2-y^2} + id_{xy}$ orbitals (for a single-spin species due to spin-orbital coupling). The d_{z^2} orbitals are at high energy, and Ref. [39] obtained an effective quadratic Hamiltonian on only the $d_{x^2-y^2} + id_{xy}$ basis element (in both layers), which reads

$$H_K(\boldsymbol{r}) = \begin{pmatrix} \frac{\hbar^2\nabla^2}{2m_*} + V_+(\boldsymbol{r}) & t(\boldsymbol{r}) \\ t^*(\boldsymbol{r}) & \frac{\hbar^2\nabla^2}{2m_*} + V_-(\boldsymbol{r}) \end{pmatrix}. \tag{A1}$$

The matrix acts on the $d_{x^2-y^2} + id_{xy}$ orbital in each layer. The Hamiltonian acts on wavepacket states in the upper $(+)$ and lower $(-)$ layers with momenta centered around, respectively,

$$\boldsymbol{\kappa}_\pm = \frac{\boldsymbol{b}_1}{2} \pm \frac{\boldsymbol{q}_1}{2} \tag{A2}$$

where

$$\boldsymbol{b}_1 = k_\theta(1,0), \quad \boldsymbol{q}_1 = k_\theta\left(0, \frac{1}{\sqrt{3}}\right), \quad \boldsymbol{b}_{i+1} = C_{3z}\boldsymbol{b}_i,$$
$$\boldsymbol{q}_{i+1} = C_{3z}\boldsymbol{q}_1, \quad k_\theta = \frac{4\pi}{\sqrt{3}}\frac{2\sin\frac{\theta}{2}}{a_0}, \tag{A3}$$

and $a_0 = 3.52$ Å is the MoTe_2 lattice constant such that the moiré reciprocal lattice is spanned by $\boldsymbol{b}_1, \boldsymbol{b}_2$ corresponding to a moiré real space lattice $\boldsymbol{a}_i$ obeying $\boldsymbol{a}_i \cdot \boldsymbol{b}_j = 2\pi\delta_{ij}$. Hence, similar to twisted bilayer graphene [43], the TMD Hamiltonians are defined by a honeycomb momentum space lattice, but with only a scalar degree of freedom at each site (the single $d_{x^2-y^2} + id_{xy}$ orbital) as opposed to a sublattice spinor. (See Fig. 11.) We obtain the momentum-space Hamiltonian by Fourier transforming into the variables (N is the number of moiré unit cells)

$$\psi_{\boldsymbol{k}}(\boldsymbol{r}) = \frac{1}{\sqrt{N}}\sum_{\boldsymbol{b},l} e^{i(\boldsymbol{k}+\boldsymbol{b}+\boldsymbol{\kappa}_l)\cdot\boldsymbol{r}} U_{\boldsymbol{b},l}(\boldsymbol{k}), \tag{A4}$$

which naturally lie on a honeycomb lattice given by $\boldsymbol{Q} = \boldsymbol{b} + \boldsymbol{\kappa}_l$, where $\boldsymbol{b}$ ranges over the whole reciprocal lattice. This leads to the momentum space Hamiltonian

$$\begin{aligned} H^K_{\boldsymbol{Q},\boldsymbol{Q}'}(\boldsymbol{k}) = &-\frac{\hbar^2}{2m_*}(\boldsymbol{k}+\boldsymbol{Q})^2\delta_{\boldsymbol{Q}\boldsymbol{Q}'} \\ &+ V\sum_i \left(e^{i\psi\zeta_{\boldsymbol{Q}}}\delta_{\boldsymbol{Q}-\boldsymbol{Q}',\boldsymbol{b}_i} + e^{-i\psi\zeta_{\boldsymbol{Q}}}\delta_{\boldsymbol{Q}-\boldsymbol{Q}',-\boldsymbol{b}_i}\right) \\ &+ w\sum_i \left(\delta_{\boldsymbol{Q}-\boldsymbol{Q}',\boldsymbol{q}_i} + \delta_{\boldsymbol{Q}-\boldsymbol{Q}',-\boldsymbol{q}_i}\right) \end{aligned} \tag{A5}$$

where $\zeta_{\boldsymbol{Q}} = \pm 1$ for $\boldsymbol{Q} = \boldsymbol{b} + \boldsymbol{\kappa}_l$ in the $l = \pm$ layer. The eigenvectors of $H^K_{\boldsymbol{Q},\boldsymbol{Q}'}(\boldsymbol{k})$ in the nth band at momentum $\boldsymbol{k}$ are denoted $U_{\boldsymbol{Q},n}(\boldsymbol{k})$, leading to the eigenstates

$$\psi_{\boldsymbol{k},n}(\boldsymbol{r}) = \frac{1}{\sqrt{N}}\sum_{\boldsymbol{Q}} e^{i(\boldsymbol{k}+\boldsymbol{Q})\cdot\boldsymbol{r}} U_{\boldsymbol{Q},n}(\boldsymbol{k}). \tag{A6}$$

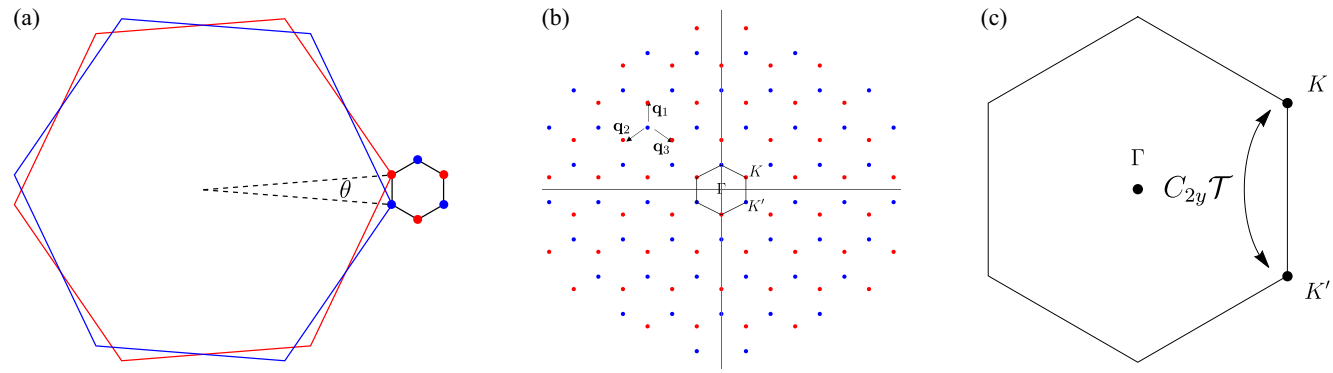

FIG. 11. (a) Brillouin zones of the top (red) and bottom (blue) layers with a relative twist angle θ, and the emergent moiré BZ in the TMD K valley. (b) Momentum space lattice with red sites (moiré K point) corresponding states in the upper layer and blue sites (moiré K' point) in the lower layer. There is a single degree of freedom per site. (c) Moiré Brillouin zone with C_{3z}-symmetric points, with K and K' points exchanged by $C_{2y}\mathcal{T}$.

Note that the spectrum of $H^K(\boldsymbol{k})$ is periodic over the moiré BZ due to

$$H^K_{\boldsymbol{Q},\boldsymbol{Q}'}(\boldsymbol{k}+\boldsymbol{b}) = H^K_{\boldsymbol{Q}+\boldsymbol{b},\boldsymbol{Q}'+\boldsymbol{b}}(\boldsymbol{k}) = [V_{\boldsymbol{b}} H^K(\boldsymbol{k}) V_{\boldsymbol{b}}^\dagger]_{\boldsymbol{Q},\boldsymbol{Q}'},$$
$$[V_{\boldsymbol{b}}]_{\boldsymbol{Q},\boldsymbol{Q}'} = \delta_{\boldsymbol{Q}+\boldsymbol{b},\boldsymbol{Q}'}, \tag{A7}$$

where $V_{\boldsymbol{b}}$ is the unitary embedding matrix. (Imposing a finite momentum space cutoff breaks the momentum space periodicity and spoils the unitarity of $V_{\boldsymbol{b}}$ due to the cutoff boundary. However, since the low-energy eigenstates $U(\boldsymbol{k})$ decay exponentially for large $\boldsymbol{b}$, this effect is negligible.) Thus we employ a periodic convention where

$$U(\boldsymbol{k}+\boldsymbol{b}) = V_{\boldsymbol{b}} U(\boldsymbol{k}), \quad U_{\boldsymbol{Q},n}(\boldsymbol{k}+\boldsymbol{b}) = U_{\boldsymbol{Q}+\boldsymbol{b},n}(\boldsymbol{k}),$$
$$\psi_{\boldsymbol{k}+\boldsymbol{b},n}(\boldsymbol{r}) = \frac{1}{\sqrt{N}} \sum_{\boldsymbol{Q}} e^{i(\boldsymbol{k}+\boldsymbol{b}+\boldsymbol{Q})\cdot\boldsymbol{r}} U_{\boldsymbol{Q}+\boldsymbol{b},n}(\boldsymbol{k}) = \psi_{\boldsymbol{k},n}(\boldsymbol{r}). \tag{A8}$$

In practice, this means one need only compute $U(\boldsymbol{k})$ in the first BZ. Band structures at the experimentally relevant angle $\theta = 3.7^\circ$ are show in Fig. 12 for all sets of parameters in Table II.

2. Space group symmetries and topology

We now discuss the intravalley space group G of the model. The symmetry representations are obtained from the transformation properties of the $d_{x^2-y^2} + id_{xy}$ orbitals in the top and bottom layers for valley K. A C_3 operation takes

$$C_3 \begin{pmatrix} d_{x^2-y^2} \\ d_{xy} \end{pmatrix} = \begin{pmatrix} -\frac{1}{2} & \frac{\sqrt{3}}{2} \\ -\frac{\sqrt{3}}{2} & -\frac{1}{2} \end{pmatrix} \begin{pmatrix} d_{x^2-y^2} \\ d_{xy} \end{pmatrix} \tag{A9}$$

so that the $d_{x^2-y^2} + id_{xy}$ orbital has C_3 eigenvalue $e^{i2\pi/3}$. Similarly $C_{2y}\mathcal{T}$ acts trivially on the $d_{x^2-y^2} + id_{xy}$ orbital, but interchanges the layer. Thus we have the representations

$$D[C_{3z}] = e^{\frac{2\pi i}{3}\sigma_0}, \quad D[C_{2y}\mathcal{T}] = \sigma_1 \mathcal{K} \tag{A10}$$

where σ_i are the Pauli matrices, $\mathcal{K}$ is complex conjugation, and the representations obey $D[g]H_K(\boldsymbol{r})D^\dagger[g] = H_K(g\boldsymbol{r})$ [see Eq. (A1)]. We take $C_{3z}\boldsymbol{r} = R(2\pi/3)\boldsymbol{r}$ and $C_{2y}\mathcal{T}(x,y) = (-x,y)$. Remarkably, the Hamiltonian inherits another symmetry due to the lowest-order harmonic approximation in Eq. (A1): a pseudo-inversion symmetry $D[\mathcal{I}] = \sigma_1$, which obeys

$$D[\mathcal{I}]H_K(\boldsymbol{r})D^\dagger[\mathcal{I}] = H_K(-\boldsymbol{r})\,. \tag{A11}$$

We emphasize that there is no microscopic inversion symmetry in the moiré system. Indeed, keeping higher-order terms will break $D[\mathcal{I}]$. One example is $t(\boldsymbol{r}) \to t(\boldsymbol{r}) + t'(\boldsymbol{r})$ where (with w' a real number)

$$t'(\boldsymbol{r}) = iw' \sum_{n=1}^{3} e^{i(-2\boldsymbol{q}_n)\cdot\boldsymbol{r}}, \tag{A12}$$

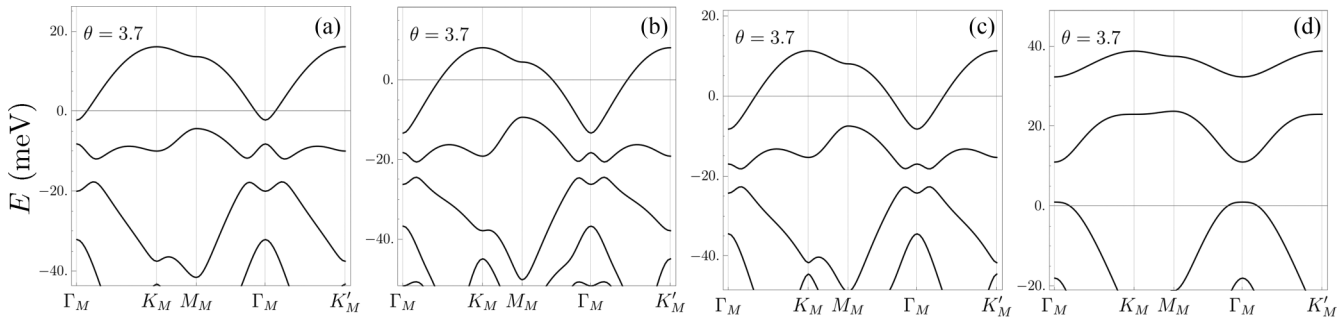

FIG. 12. Comparison of band structures for the parameter values in Table II, where (a)–(d) correspond to rows 1–4. We see that (a)–(c), which are in the Ch $= (-1,-1)$ phase, are quite similar (see main text), whereas (d) in the Ch $= (-1,+1)$ phase (see main text) has a significantly different dispersion. For this reason, we focus our comparative study on the parameters in (a) and (d).

which preserves C_{3z} and $C_{2y}\mathcal{T}$. The *ab initio* spectrum in Ref. [29] does indeed show small-$\mathcal{I}$ breaking in the band structure, but these effects appear to be less than ∼1 meV and can be neglected at leading order.

Using the symmetries of the model, the *generic* appearance of Chern bands can be predicted from topological quantum chemistry [57,100]. Consider the large V limit where interlayer hopping w and kinetic energy are subleading terms. Then we expect the valence band eigenstates to be formed from "atomically" localized wavefunctions at $\boldsymbol{r}_\pm$, the minima of $-V_\pm(\boldsymbol{r})$ in each layer. We find that

$$\boldsymbol{r}_\pm = \begin{cases} \pm\frac{1}{3}(\boldsymbol{a}_1+\boldsymbol{a}_2), & -\pi < \psi < -\pi/3 \\ \boldsymbol{0}, & |\psi| < \pi/3 \\ \mp\frac{1}{3}(\boldsymbol{a}_1+\boldsymbol{a}_2), & \pi/3 < \psi < \pi \end{cases} \tag{A13}$$

meaning that, if $|\psi| > \pi/3$, the atomic states are centered at opposite corners of the moiré unit cell related by $C_{2y}\mathcal{T}$. This is the 2b Wyckoff position. Consulting the Bilbao crystallographic server [101,102], we find that any atomic states induced from this position realize a decomposable elementary band representation formed by two disconnected bands with Chern number $\pm 1 \bmod 3$ [55,56]. This is in agreement with the numerically calculated Chern numbers for the parameters of Ref. [29] where $V/w > 1$, as shown in the main text. This shows that topology is inherent in this model, no matter what terms are added (as long as they are small), in a similar way as in twisted bilayer graphene.

We now turn to the representations in momentum space. A space group symmetry $g \in G$ has a matrix representation $D[g]$ on the momentum-space Hamiltonian Eq. (A5) obeying

$$D[g]H^K(\boldsymbol{k})D[g]^{-1} = H^K(g\boldsymbol{k})\,. \tag{A14}$$

Similarly, the (unitary and anti-unitary) momentum space representations of the true space group symmetries are

$$\begin{aligned} &D_{\boldsymbol{Q},\boldsymbol{Q}'}[C_{3z}] = e^{i\frac{2\pi}{3}}\delta_{\boldsymbol{Q},C_{3z}\boldsymbol{Q}'}, \quad D_{\boldsymbol{Q},\boldsymbol{Q}'}[C_{2y}\mathcal{T}] = \delta_{\sigma_3\boldsymbol{Q},\boldsymbol{Q}'}\mathcal{K}, \\ &D_{\boldsymbol{Q},\boldsymbol{Q}'}[\mathcal{I}] = \delta_{\boldsymbol{Q},-\boldsymbol{Q}'}, \end{aligned} \tag{A15}$$

where we abuse notation by taking $C_{2y}\mathcal{T}(k_x,k_y) = (k_x,-k_y) = \sigma_3\boldsymbol{k}$ as the momentum vector representation [the position space representation is $C_{2y}\mathcal{T}(x,y) = (-x,y)$ since $\mathcal{T}$ is local], and $\mathcal{K}$ is complex conjugation. Note that $C_{2y}\mathcal{T}$ and pseudo-inversion $\mathcal{I}$ flip the layers, while C_{3z} does not. These symmetries form the 3D magnetic space group 164.89 ($P\bar{3}m'1$), which is isomorphic in 2D to the magnetic wallpaper group $6m'm'$ where the sixfold pseudorotation is $C_{3z}^{-1}\mathcal{I}$. We refer to $\mathcal{I}$ as a pseudo-inversion because it is intravalley, while a true inversion symmetry would exchange the K and $K' = -K$ valleys. Finally, the Hamiltonian in the K' valley can be obtained from the spinful time-reversal symmetry of the underlying TMD model, which acts as $i\tau_2\mathcal{K}$ and maps, e.g., the $d_{x^2-y^2}+id_{xy}$ spin ↑ orbitals in valley K to $d_{x^2-y^2}-id_{xy}$ spin ↓ orbitals at valley K'. (Here τ is the valley matrix.) Thus the Hamiltonian at K' is

$$H^{K'}_{\boldsymbol{Q},\boldsymbol{Q}'}(\boldsymbol{k}) = H^K_{-\boldsymbol{Q},-\boldsymbol{Q}'}(-\boldsymbol{k})^*\,. \tag{A16}$$

Since the two valleys are related by time reversal and the model preserves $U(1)$ valley symmetry, we can choose a gauge $U^\eta_{\boldsymbol{Q},n}(\boldsymbol{k}) = \overline{U}^\eta_{\eta\boldsymbol{Q},n}(\eta\boldsymbol{k})$ where $\eta = \pm$ denotes the K/K' a valley, and $\overline{x}^+ = x, \overline{x}^- = x^*$.

To compute the Berry curvature and quantum geometry of the bands, we use the integrals [103]

$$\begin{aligned} \frac{\mathrm{Ch}}{2\pi} &= \int \frac{d^2k}{(2\pi)^2}\frac{i}{2}\epsilon_{ij}\mathrm{Tr}P(\boldsymbol{k})[\partial_iP(\boldsymbol{k}),\partial_jP(\boldsymbol{k})], \\ \frac{G}{2\pi} &= \int \frac{d^2k}{(2\pi)^2}\frac{1}{2}\mathrm{Tr}\partial_iP(\boldsymbol{k})\partial_iP(\boldsymbol{k}), \end{aligned} \tag{A17}$$

where $P(\boldsymbol{k}) = U(\boldsymbol{k})U^\dagger(\boldsymbol{k})$ is the gauge-invariant projector on the single-particle eigenvector $U(\boldsymbol{k})$. The advantage of the projector formalism is that no smooth gauge is necessary, and discretization can be done efficiently [104]. The integrands of Eq. (A17) are the Berry curvature and Fubini-Study metric respectively. We report the Chern numbers Ch and integrated Fubini-Study metric G, along with their structure over the moiré Brillouin zone in Figs. 13 and 14 for the two bands included in our interacting calculations.

APPENDIX B: MORE DETAILS ON INTERACTION AND PARTICLE-HOLE SYMMETRY

In this Appendix, we discuss two types of the interaction and the PH transformations of the projected Hamiltonians.

1. Interaction in the electron and hole language

In the previous theoretical studies [16,28,29,31,32,34,36,37] on FCIs in tMoTe$_2$, two types of interactions are mainly used. One is the Coulomb interaction among holes, used in Ref. [28], for which the explicit Hamiltonian is

$$\begin{aligned} H_h = &\int d^2r \sum_{\eta,ll'} \widetilde{c}^\dagger_{\eta,l,\boldsymbol{r}}[-H_\eta(\boldsymbol{r})]_{ll'}\widetilde{c}_{\eta,l',\boldsymbol{r}} \\ &+ \frac{1}{2}\sum_{l\eta,l'\eta'}\int d^2rd^2r'V(\boldsymbol{r}-\boldsymbol{r}')\widetilde{c}^\dagger_{\eta,l,\boldsymbol{r}}\widetilde{c}^\dagger_{\eta',l',\boldsymbol{r}'}\widetilde{c}_{\eta',l',\boldsymbol{r}'}\widetilde{c}_{\eta,l,\boldsymbol{r}}, \end{aligned} \tag{B1}$$

where $\widetilde{c}^\dagger_{\eta,l,\boldsymbol{r}}$ creates a hole at position $\boldsymbol{r}$ in the lth layer in the η valley and $H_\eta(\boldsymbol{r})$ is the single-particle electron Hamiltonian, and $V(\boldsymbol{r})$ is the double-gated screened Coulomb potential with gate distance ξ,

$$\begin{aligned} V(\boldsymbol{r}) &= \int_{\mathbb{R}^2}\frac{d^2p}{(2\pi)^2}V(\boldsymbol{p})e^{i\boldsymbol{p}\cdot\boldsymbol{r}}, \\ V(\boldsymbol{p}) &= \pi\xi^2V_\xi\frac{\tanh(\xi|\boldsymbol{p}|/2)}{\xi|\boldsymbol{p}|/2}, \quad V_\xi = \frac{e^2}{4\pi\epsilon\epsilon_0\xi}. \end{aligned} \tag{B2}$$

Here ϵ_0 is the vacuum permittivity, and ϵ is the dielectric constant. The vacuum state of $\widetilde{c}_{\eta,l,\boldsymbol{r}}$ is the charge neutrality point$|\nu=0\rangle$ with $\widetilde{c}_{\eta,l,\boldsymbol{r}}|\nu=0\rangle = 0$, which corresponding to fully filling all the electron states of the single-particle Hamiltonian, and the Hilbert space is just given by acting various powers of $\widetilde{c}^\dagger_{\eta,l,\boldsymbol{r}}$ on $|\nu=0\rangle$.

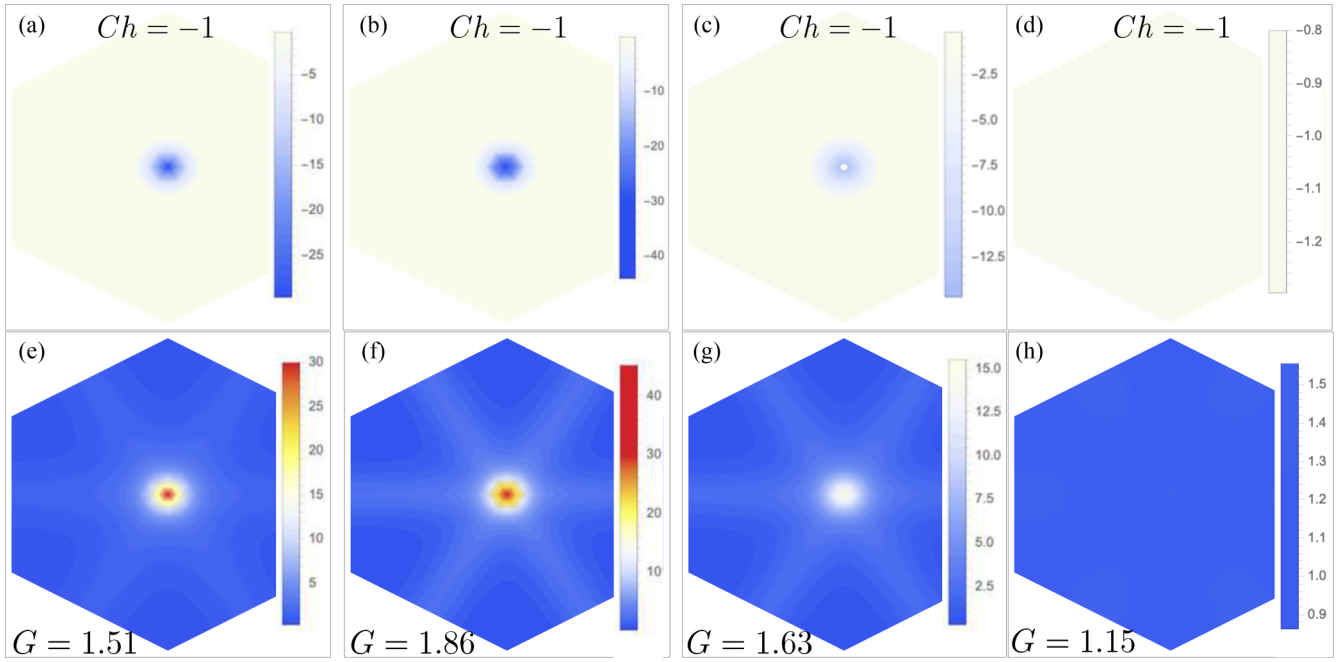

FIG. 13. Comparison of the highest valence band Berry curvature [(a)–(d)] and Fubini-Study metric [(e)–(h)] for the parameter values in Table II, corresponding to rows 1–4. Again we see strong similarity between the first three rows where the Γ_M point shows a strong peak in the quantum geometry, compared to the nearly uniform features in (d) and (h). Color bars are consistent across all plots.

The other common Hamiltonian is the Coulomb interaction among electrons, which is used in Refs. [16,29],

$$H_e = \int d^2r \sum_{\eta,ll'} c^\dagger_{\eta,l,\boldsymbol{r}} [H_\eta(\boldsymbol{r})]_{ll'} c_{\eta,l',\boldsymbol{r}} + \frac{1}{2} \sum_{l\eta,l'\eta'} \int d^2r d^2r' V(\boldsymbol{r}-\boldsymbol{r}') c^\dagger_{\eta,l,\boldsymbol{r}} c^\dagger_{\eta',l',\boldsymbol{r}'} c_{\eta',l',\boldsymbol{r}'} c_{\eta,l,\boldsymbol{r}}, \tag{B3}$$

where $c^\dagger_{\eta,l,\boldsymbol{r}}$ creates an electron at position $\boldsymbol{r}$ in the lth layer in the η valley. Importantly, charge neutrality $|\nu = 0\rangle$ is not the vacuum of $c_{\eta,l,\boldsymbol{r}}$, i.e., $c_{\eta,l,\boldsymbol{r}}|\nu = 0\rangle \neq 0$. Instead, the Fock vacuum obeys $c_{\eta,l,\boldsymbol{r}}|0\rangle = 0$.

The Hilbert space of H_e is the same as H_h, as $c^\dagger_{\eta,l,\boldsymbol{r}}$ is related to $\tilde{c}_{\eta,l,\boldsymbol{r}}$ by

$$\mathcal{K} c^\dagger_{\eta,l,\boldsymbol{r}} \mathcal{K}^{-1} = \tilde{c}_{\eta,l,\boldsymbol{r}}\,, \tag{B4}$$

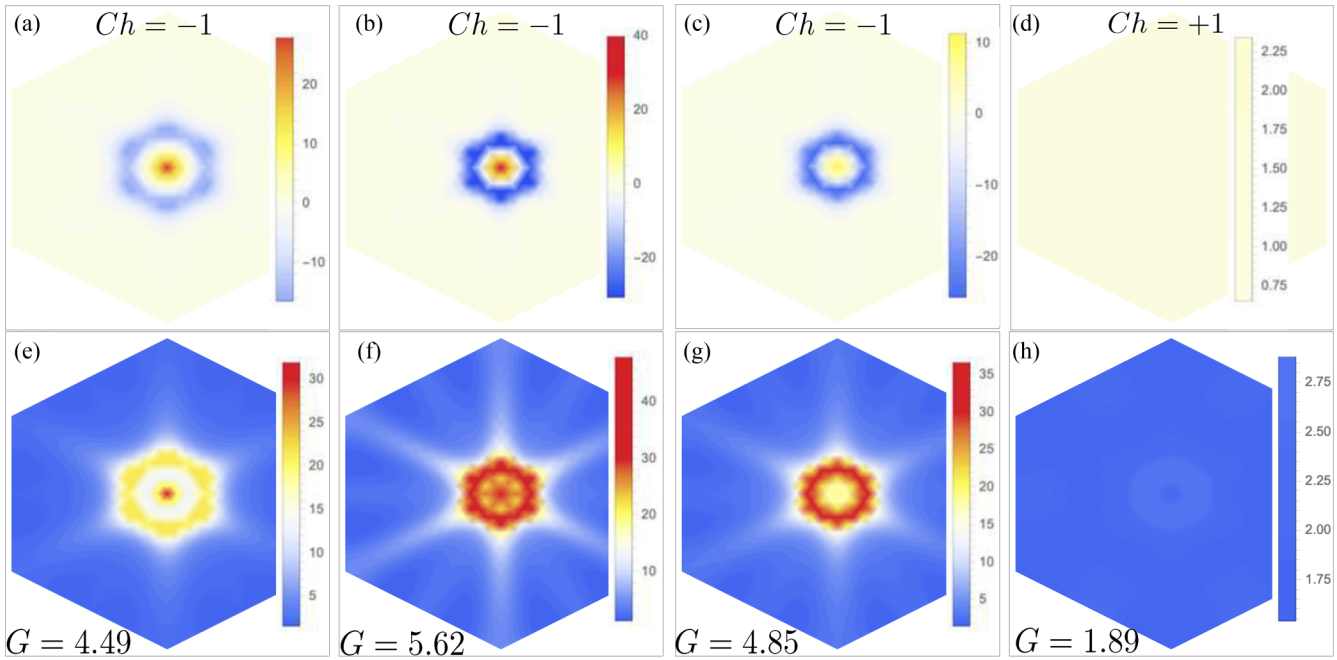

FIG. 14. Comparison of the second highest valence band Berry curvature [(a)–(d)] and Fubini-Study metric [(e)–(h)] for the parameter values in Table II, corresponding to rows 1–4. Color bars are consistent across all plots.

where $\mathcal{K}$ is a complex conjugate. As a result, H_e differs from H_h by the complex conjugate and a single-body term,

$$\mathcal{K}H_e\mathcal{K}^{-1} = H_h + \Delta H + \text{const.}, \tag{B5}$$

where

$$\Delta H = \left(V(\mathbf{0}) - 4\int d^2r' V(\boldsymbol{r}')\delta(0)\right)\sum_{l\eta}\int d^2r \widetilde{c}^\dagger_{\eta,l,\boldsymbol{r}}\widetilde{c}_{\eta,l,\boldsymbol{r}}\,, \tag{B6}$$

and we have used that $V(\boldsymbol{r})$ is real. Naively, ΔH is proportional to the particle-number operator, and thus one may think in a fixed-particle-number sector, ΔH becomes a constant, and the two Hamiltonian are related by a complex conjugate up to a constant. However, in reality, we can never use the continuous Hamiltonian to do HF or ED calculations; instead, we will project the Hamiltonian into a finite set of bands. We will see in the following that after the projection, the two Hamiltonians are not necessarily related due to one-body terms that appear from the different normal orderings.

As just mentioned, we project the Hamiltonian into a finite set of band spanned by the operators

$$\widetilde{\gamma}^\dagger_{n,\eta,\boldsymbol{k}} = \sum_{\boldsymbol{Q}}\widetilde{c}^\dagger_{\eta,\boldsymbol{k},\boldsymbol{Q}}[U_{n,\eta,\boldsymbol{k}}]_{\boldsymbol{Q}}\,, \tag{B7}$$

where the band index n only takes a finite set of values. The projected Hamiltonian in this basis is

$$H_h = -\sum_{\boldsymbol{k},\eta,n}\widetilde{\gamma}^\dagger_{\eta,n,\boldsymbol{k}}\widetilde{\gamma}_{\eta,n,\boldsymbol{k}}E_{\eta,n}(\boldsymbol{k}) + \frac{1}{2}\sum_{\boldsymbol{k},\boldsymbol{k}',\boldsymbol{q}}\sum_{\eta,\eta'}\sum_{m,m',n'}V_{\eta\eta',mm'n'n}(\boldsymbol{k},\boldsymbol{k}',\boldsymbol{q})\widetilde{\gamma}^\dagger_{\eta,m,\boldsymbol{k}+\boldsymbol{q}}\widetilde{\gamma}^\dagger_{\eta',m',\boldsymbol{k}'-\boldsymbol{q}}\widetilde{\gamma}_{\eta',n',\boldsymbol{k}'}\widetilde{\gamma}_{\eta,n,\boldsymbol{k}}, \tag{B8}$$

where

$$V_{\eta\eta',mm'n'n}(\boldsymbol{k},\boldsymbol{k}',\boldsymbol{q}) = \frac{1}{N}\sum_{\boldsymbol{b}}\frac{V(\boldsymbol{q}+\boldsymbol{b})}{\Omega}M_{\eta,mn}(\boldsymbol{k},\boldsymbol{q}+\boldsymbol{b})M^*_{\eta',n'm'}(\boldsymbol{k}'-\boldsymbol{q},\boldsymbol{q}+\boldsymbol{b}),$$
$$M_{\eta,mn}(\boldsymbol{k},\boldsymbol{q}) = U^\dagger_{\eta,m,\boldsymbol{k}+\boldsymbol{q}}U_{\eta,n,\boldsymbol{k}}, \quad \Omega^{-1} = \boldsymbol{b}_1\times\boldsymbol{b}_2/(2\pi)^2, \tag{B9}$$

are the matrix elements, form factors, and (inverse) moiré unit-cell area respectively.

Hermiticity requires

$$V^*_{\eta\eta',nn'm'm}(\boldsymbol{k}+\boldsymbol{q},\boldsymbol{k}'-\boldsymbol{q},-\boldsymbol{q}) = V_{\eta\eta',mm'n'n}(\boldsymbol{k},\boldsymbol{k}',\boldsymbol{q})\,, \tag{B10}$$

and the fermion statistics gives

$$V_{\eta'\eta,m'mnn'}(\boldsymbol{k}',\boldsymbol{k},-\boldsymbol{q}) = V_{\eta\eta',mm'n'n}(\boldsymbol{k},\boldsymbol{k}',\boldsymbol{q})\,. \tag{B11}$$

On the other hand, after projection into the band basis $\gamma^\dagger_{n,\eta,\boldsymbol{k}} = \sum_{\boldsymbol{Q}}c^\dagger_{\eta,\boldsymbol{k},\boldsymbol{Q}}[U_{n,\eta,\boldsymbol{k}}]_{\boldsymbol{Q}}$, H_e becomes

$$H_e = \sum_{\boldsymbol{k},\eta,n}\gamma^\dagger_{\eta,n,\boldsymbol{k}}\gamma_{\eta,n,\boldsymbol{k}}E_{\eta,n}(\boldsymbol{k}) + \frac{1}{2}\sum_{\boldsymbol{k},\boldsymbol{k}',\boldsymbol{q}}\sum_{\eta,\eta'}V_{\eta\eta',mm'n'n}(\boldsymbol{k},\boldsymbol{k}',\boldsymbol{q})\gamma^\dagger_{m,\eta,\boldsymbol{k}+\boldsymbol{q}}\gamma^\dagger_{m',\eta',\boldsymbol{k}'-\boldsymbol{q}}\gamma_{n',\eta',\boldsymbol{k}'}\gamma_{n,\eta,\boldsymbol{k}}. \tag{B12}$$

Now we show the relation between the two Hamiltonian after the projection. According to Eq. (B4), we have $\widetilde{c}^\dagger_{\eta,\boldsymbol{k},\boldsymbol{Q}} = \mathcal{K}c_{\eta,\boldsymbol{k},\boldsymbol{Q}}\mathcal{K}$, and then $\gamma_{n,\eta,\boldsymbol{k}}$ and $\widetilde{\gamma}^\dagger_{n,\eta,\boldsymbol{k}}$ are related by

$$\mathcal{K}\gamma_{n,\eta,\boldsymbol{k}}\mathcal{K}^{-1} = \widetilde{\gamma}^\dagger_{n,\eta,\boldsymbol{k}}\,. \tag{B13}$$

Under the $\mathcal{K}$, now the projected Hamiltonians are related as

$$\mathcal{K}H_e\mathcal{K}^{-1} = \sum_{\eta,\boldsymbol{k},nm}\widetilde{\gamma}^\dagger_{\eta,n,\boldsymbol{k}}\widetilde{\gamma}_{\eta,m,\boldsymbol{k}}\epsilon_{\eta,nm}(\boldsymbol{k}) + H_h\,, \tag{B14}$$

where

$$\begin{aligned}\epsilon_{\eta,nm}(\boldsymbol{k}) = -\frac{1}{2}\sum_{\boldsymbol{k}',\eta',n'}&[V^*_{\eta\eta',mn'n'n}(\boldsymbol{k},\boldsymbol{k}',0)\\ &+ V_{\eta\eta',nn'n'm}(\boldsymbol{k},\boldsymbol{k}',0)]\\ &+\frac{1}{2}\sum_{\boldsymbol{q}n'}[V_{\eta\eta,n'nn'm}(\boldsymbol{k},\boldsymbol{k}+\boldsymbol{q},\boldsymbol{q})\\ &+ V^*_{\eta\eta,n'mn'n}(\boldsymbol{k},\boldsymbol{k}+\boldsymbol{q},\boldsymbol{q})],\end{aligned} \tag{B15}$$

which in general is not zero as we only consider a finite sets of n and m. The nonvanishing $\epsilon_{\eta,nm}(\boldsymbol{k})$ is consistent with the different HF phase diagrams given by H_e and H_h in Fig. 4. Physically, $\epsilon_{\eta,nm}(\boldsymbol{k})$ represents the different background potential felt by the electron interaction.

2. Particle-hole symmetry

In this part, we only talk about H_h and H_e after projection to a finite set of bands. Neither of the Hamiltonians H_h and H_e preserves the PH symmetry exactly in general after the projection. Here the PH transformation for H_e is defined as

$$\mathcal{C}\gamma^\dagger_{\eta,n,\boldsymbol{k}}\mathcal{C}^{-1} = \gamma_{\eta,n,\boldsymbol{k}}\,, \tag{B16}$$

where $\mathcal{C}$ is an anti-unitary operator. Under this PH transformation, H_e would gain two extra terms,

$$\begin{aligned}\mathcal{C}H_e\mathcal{C}^{-1} = H_e &+ \sum_{\eta,\boldsymbol{k},n}\gamma^\dagger_{\eta,n,\boldsymbol{k}}\gamma_{\eta,n,\boldsymbol{k}}(-2E_{\eta,n}(\boldsymbol{k}))\\ &+\sum_{\eta,\boldsymbol{k},nm}\gamma^\dagger_{\eta,n,\boldsymbol{k}}\gamma_{\eta,m,\boldsymbol{k}}\epsilon_{\eta,nm}(\boldsymbol{k}) + \text{const.}\,,\end{aligned} \tag{B17}$$

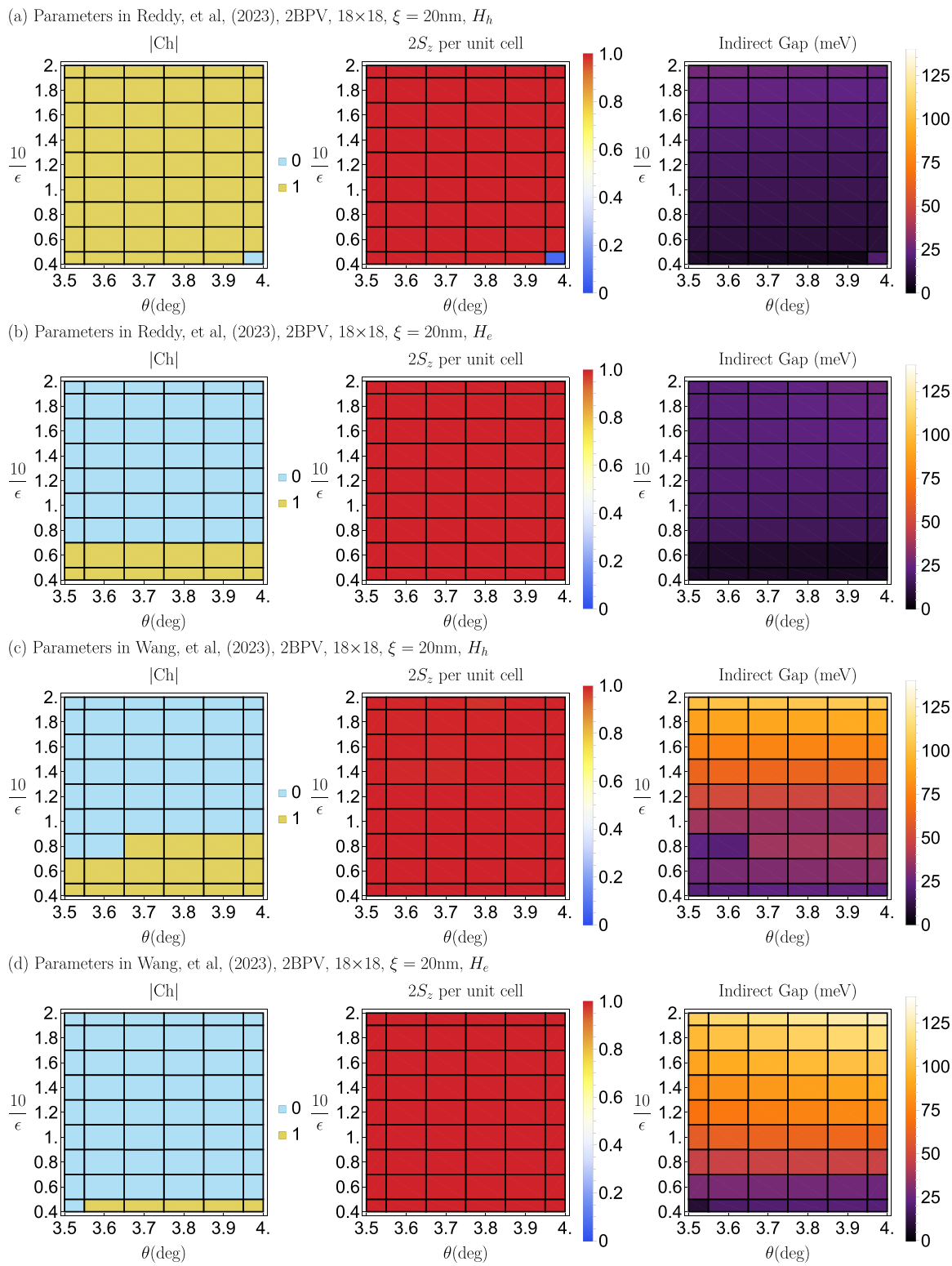

FIG. 15. The 2BPV Hartree-Fock results for $\xi = 20$ nm at $\nu = -1$ for the parameters in Ref. [28] [(a) and (b)] and the parameters in Ref. [29] [(c) and (d)]. 18×18 labels the system size. H_h [(a) and (c)] and H_e [(b) and (d)] refer to the Hamiltonian used. Ch refers to the Chern number (leftmost panel), the middle panel shows the value of $2S_z$ per unit cell, and the indirect gap (right panel) is the indirect gap of the HF band structure. The spin-unpolarized state in (a) is intervalley coherent translationally breaking state with wavevector K_M.

where $(-2E_{\eta,n}(\boldsymbol{k}))$ accounts for the sign flipping of the single-particle dispersion, and $\epsilon_{\eta,nm}(\boldsymbol{k})$ is given in Eq. (B15). The reason that $\epsilon_{\eta,nm}(\boldsymbol{k})$ in Eq. (B17) is the same as that in Eq. (B14) is that the transformation in Eq. (B13) will become the PH transformation in Eq. (B16) if we identify $\widetilde{\gamma}_{\eta,n,\boldsymbol{k}}$ in Eq. (B13) with $\gamma^{\dagger}_{\eta,n,\boldsymbol{k}}$.

For H_h, the PH transformation is given by replacing $\gamma_{\eta,n,\boldsymbol{k}}$ in Eq. (B16) by $\widetilde{\gamma}_{\eta,n,\boldsymbol{k}}$, and the PH breaking term $\mathcal{C}H_h\mathcal{C}^{-1} - H_h$

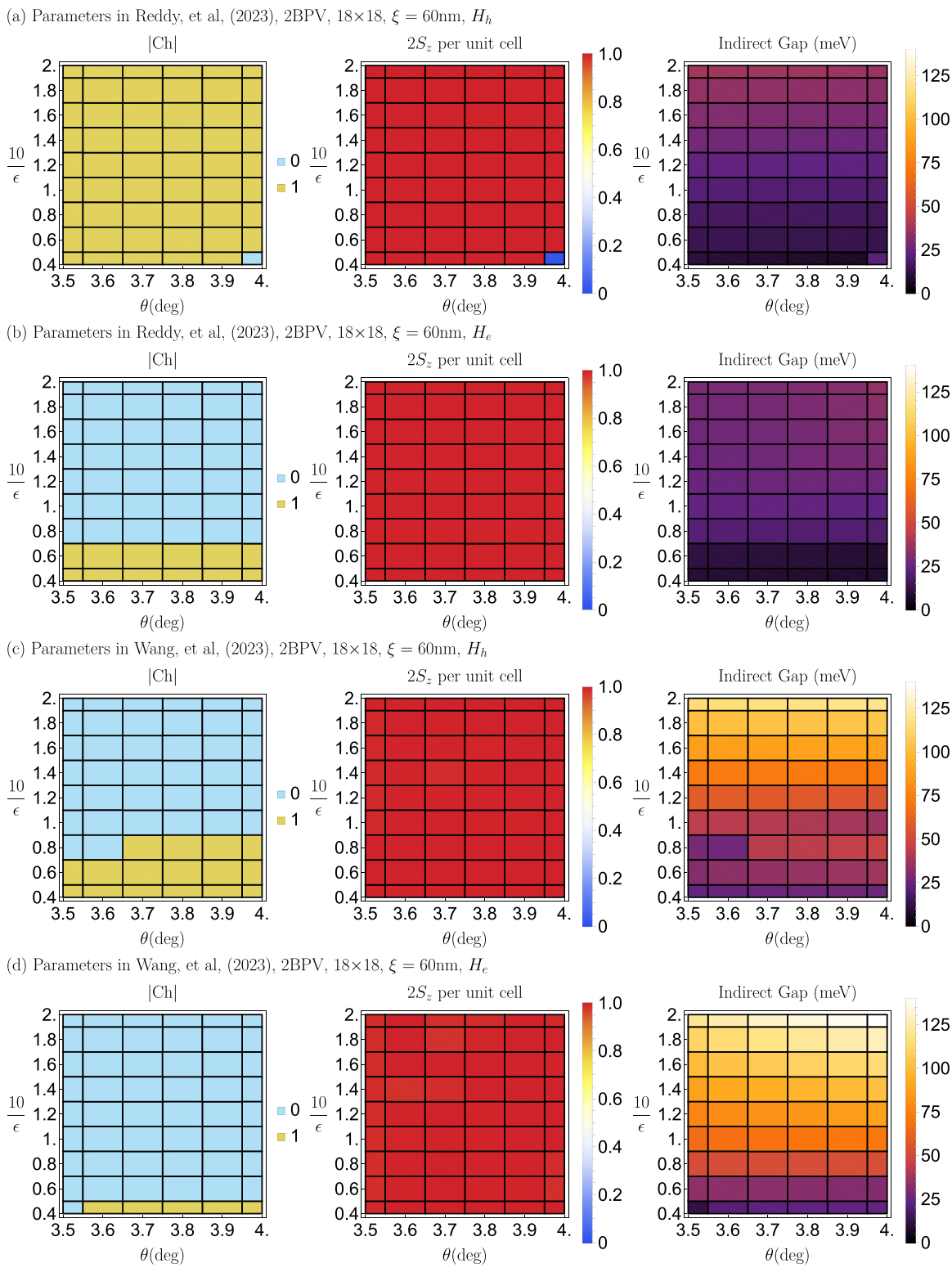

FIG. 16. The 2BPV Hartree-Fock results for $\xi = 60$ nm at $\nu = -1$ for the parameters in Ref. [28] [(a),(b)] and the parameters in Ref. [29] [(c),(d)]. The notations are identical to those in Fig. 15.

is just given by performing $E_{\eta,n}(\boldsymbol{k}) \to -E_{\eta,n}(\boldsymbol{k})$ in the PH-breaking term in Eq. (B17),

$$\mathcal{C}H_h\mathcal{C}^{-1} = H_h + \sum_{\eta,\boldsymbol{k},n} \widetilde{\gamma}^{\dagger}_{\eta,n,\boldsymbol{k}}\widetilde{\gamma}_{\eta,n,\boldsymbol{k}}(2E_{\eta,n}(\boldsymbol{k})) + \sum_{\eta,\boldsymbol{k},nm} \widetilde{\gamma}^{\dagger}_{\eta,n,\boldsymbol{k}}\widetilde{\gamma}_{\eta,m,\boldsymbol{k}}\epsilon_{\eta,nm}(\boldsymbol{k}) + \text{const.}\,. \quad \text{(B18)}$$

The extra one-body term given by the PH transformation is in general nonvanishing, meaning that H_e and H_h are not invariant under this transformation.

When the PH breaking effect is strong, i.e., $\epsilon_{\eta,nm}(\boldsymbol{k})$ is large, the two fillings related by PH transformation would have considerable difference. It is also important to note

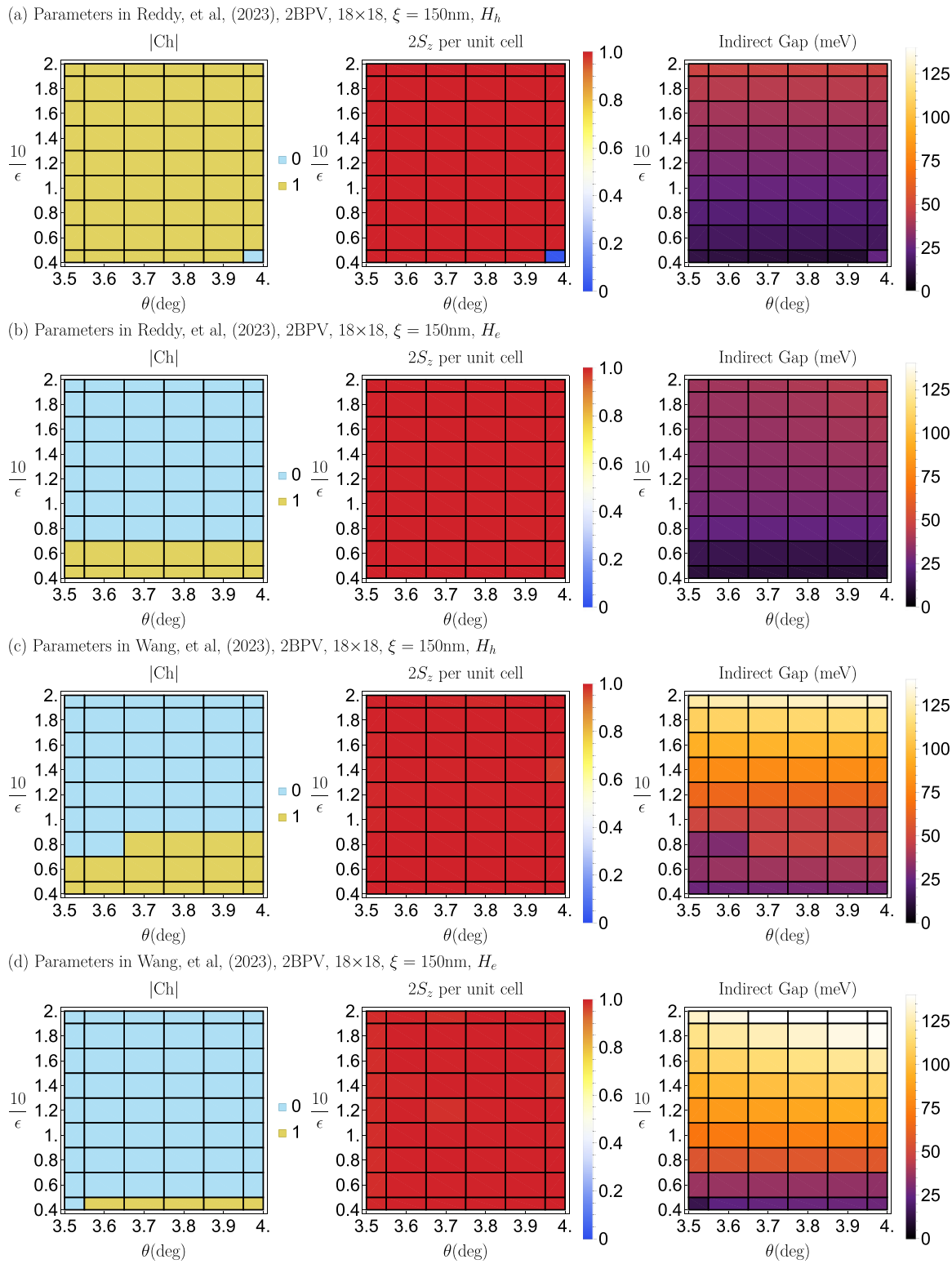

FIG. 17. The 2BPV Hartree-Fock results for $\xi = 150$ nm at $\nu = -1$ for the parameters in Ref. [28] [(a),(b)] and the parameters in Ref. [29] [(c),(d)]. The notations are identical to those in Fig. 15.

that as we are talking about the PH transformation of the projected Hamiltonian, the PH transformation only acts on the finite projected subspace, and thus the PH-related fillings depend on the how many bands we keep in the projected model. If we consider the fully spin-polarized case where we only keep one valley (spin) and one band in that valley, the PH transformation maps ν to $-1-\nu$ (e.g., $-1/3$ to $-2/3$) electron filling. If we keep two valleys and one band per valley, the PH transformation maps ν to $-2-\nu$ (e.g., $-2/3$ to $-4/3$) electron filling. In general, if we keep two valleys and N band per valley, the PH transformation maps ν to $-2N-\nu$.

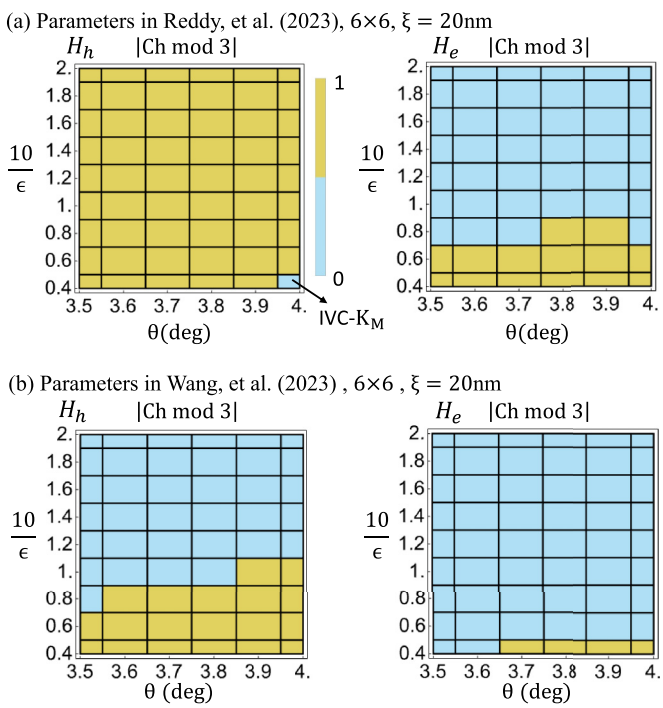

FIG. 18. The 2BPV 6 × 6 results for $\xi = 20$ nm at $\nu = -1$. The notations are analogous to Fig. 4 in the main text. H_h and H_e refer to the Hamiltonian used, Ch refers to the Chern number, and we take Ch mod 3 $\in \{-1, 0, 1\}$. The $|\text{Ch mod 3}| = 0$ region for H_h in (a) comes from a *non*ferromagnetic ground state, which is intervalley coherent translationally breaking state with wavevector K_M. Owing to the small sizes, we only use Eq. (7) to compute Ch mod 3 as it does not require a Berry curvature integral.

APPENDIX C: ADDITIONAL HARTREE-FOCK RESULTS AT $\nu = -1$

In this Appendix, we provide more details on the Hartree-Fock (HF) calculations at $\nu = -1$. We note that system size $L_1 \times L_2$ means that the momenta included in the calculation are $(n/L_1)\boldsymbol{b}_1 + (m/L_2)\boldsymbol{b}_2$ with $n = 0, \ldots, L_1 - 1$ and $m = 0, \ldots, L_2 - 1$, where $\boldsymbol{b}_1$ and $\boldsymbol{b}_2$ are defined in Eq. (A2).

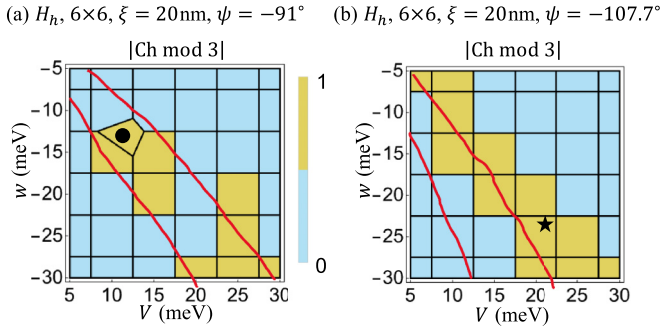

FIG. 19. The 6 × 6 2BPV Hartree-Fock results for $\xi = 20$ nm at $\nu = -1$ for the m_*, ψ parameters in Ref. [28] (a) and Ref. [29] (b). We choose $\epsilon = 5$ in (a) and $\epsilon = 50/3 \approx 16.67$ in (b). The boundaries of the three single-particle parameter regions are marked in red according to Fig. 3. The dot and the star correspond to the parameters in Ref. [28] and Ref. [29], respectively.

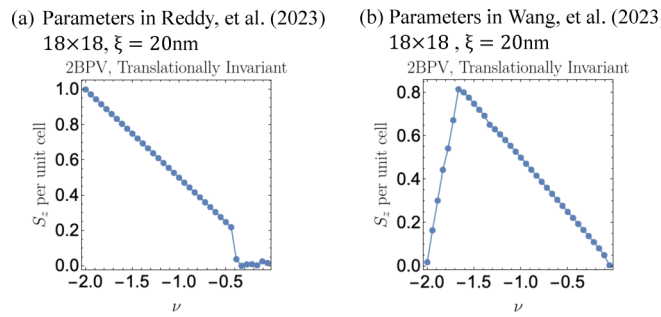

FIG. 20. The 2BPV Hartree-Fock results for H_h and $\xi = 20$ nm at $\nu = -1$ done by restricting to the translationally invariant subspace. We choose $\epsilon = 5$ in (a) and $\epsilon = 50/3 \approx 16.67$ in (b). 18 × 18 labels the system size. The spinful gap is smallest energy cost to change the total spin of the ground state according to the HF band structure. In (a), the nonmagnetic states for $\nu > -0.4$ in (a) are consistent with experiments [24–27], but the fact that the ferromagnetic ground states persists to $\nu = -2$ differs from the experiments. In (b), the ferromagnetic ground states start from nearly zero ν and persist to $\nu = -1.6$, which is not consistent with experiments. Therefore, the translationally invariant HF cannot fully capture the behaviors of ferromagnetism observed in experiments.

As mentioned in the main text, we have considered the effect of the screening length ξ. We provide the HF phase diagrams for the system size of 18 × 18 in Fig. 15 for $\xi = 20$ nm, in Fig. 16 for $\xi = 60$ nm, and in Fig. 17 for $\xi = 150$ nm (as a reminder, we used $\xi = 20$ nm in the main text). We choose two types of initial states: (i) translationally invariant initial

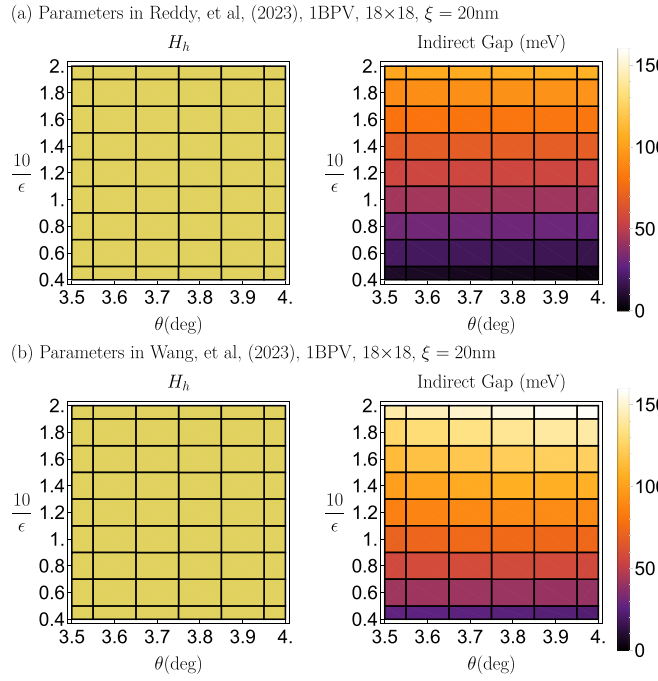

FIG. 21. The 1BPV Hartree-Fock results for H_h with $\xi = 20$ nm at $\nu = -1$. 18 × 18 labels the system size, and and Ch refers to the Chern number. The ground states are always spin-polarized and thus has nonzero Chern number; the indirect gap is the indirect gap of the HF band structure.

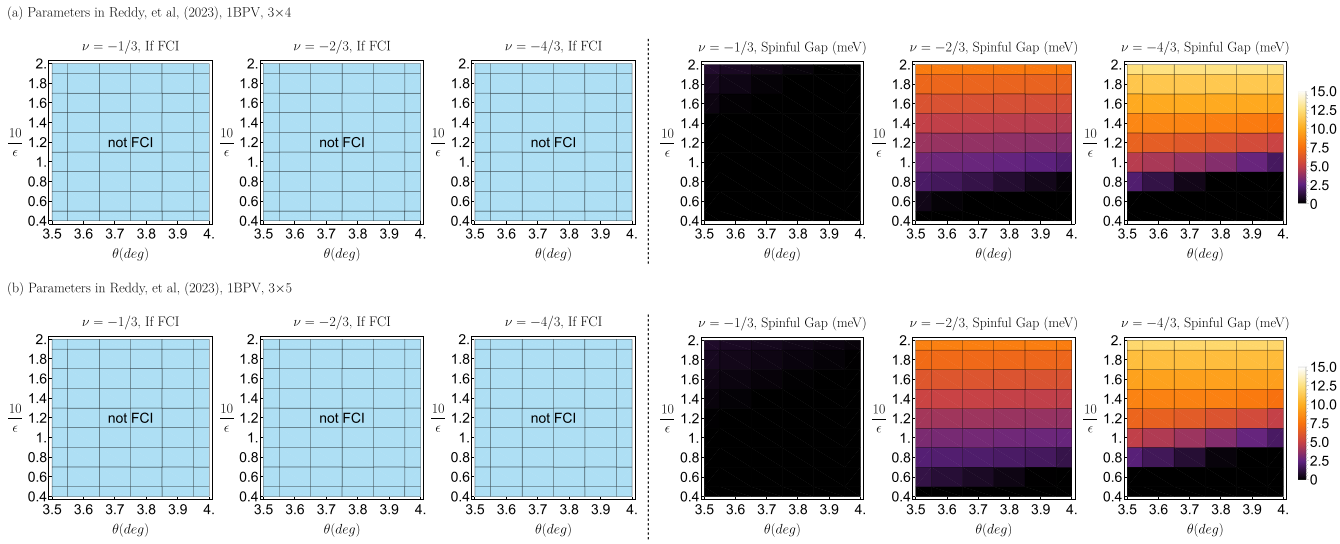

FIG. 22. The summary of 1BPV spinful gaps for the parameter values of Ref. [28] for the system sizes of 3×4 and 3×5. In the left most three figures, blue ("not FCI") means that we do not see clear signatures of FCI or maximally spin-polarized CDW. The rightmost three figures of give the spinful gaps, which are shown with the same color functions for all plots. If the spinful gap is negative, it is set to zero in the plot.

states (with random band mixing), and (ii) translationally breaking intervalley-coherent states with wavevector K_M [37]. We can see the phase diagrams of the ferromagnetism are the same for all three values of ξ: the ground states are always ferromagnetic except the lower right corner of the phase diagram of H_h for the parameters in Ref. [28], which is IVC-K_M; IVC-K_M is also found at small interaction in Ref. [37] for the parameters in Ref. [28]. The phase diagrams of Chern number are also the same for all three values of ξ and for the (θ, ϵ) mesh that we choose. The $\mathrm{Ch} = 0$ phase that occurs as the interaction increases comes form the band inversion at K_M or K'_M between two bands in one valley. The only notable effect of the screening length is that as ξ increases, the indirect gap of the HF bands increases, which makes sense as larger screening length means stronger interaction.

Since our ED calculations are done for much smaller sizes than 18×18, we would like to check whether the phase diagram of the Chern numbers have qualitative changes if we go to much smaller sizes. For this purpose, we perform 6×6 HF calculations, and map out the phase diagram for the Chern number in Fig. 18. Compared to the Chern number phase diagrams in Fig. 15, we found that the Chern phase diagrams are very similar to those at 18×18, meaning that the finite-size effect of the Chern phase diagrams is very

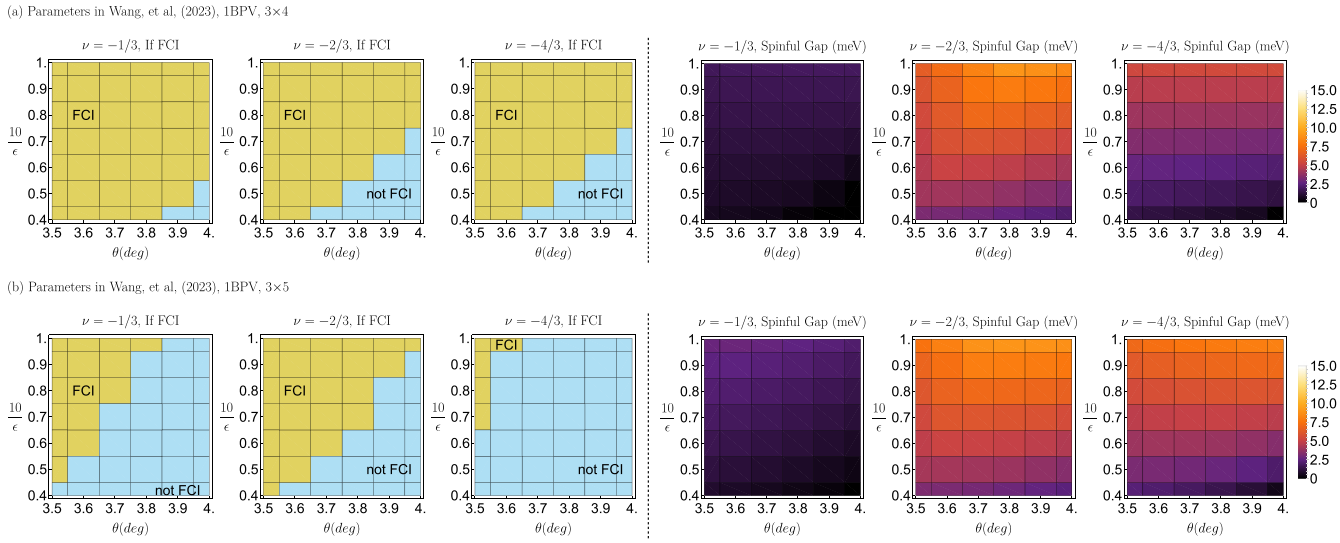

FIG. 23. The summary of 1BPV spinful gaps for the parameter values of Ref. [29] for the system sizes of 3×4 and 3×5. In the leftmost three figures of each row, green ("FCI") labels the region that satisfies the criterion in Prop. 1, and blue ("not FCI") means that we do not see clear signatures of FCI or maximally spin-polarized CDW. The rightmost three figures of each row give the spinful gaps, which are shown with the same color functions for all plots. If the spinful gap is negative, it is set to zero in the plot.

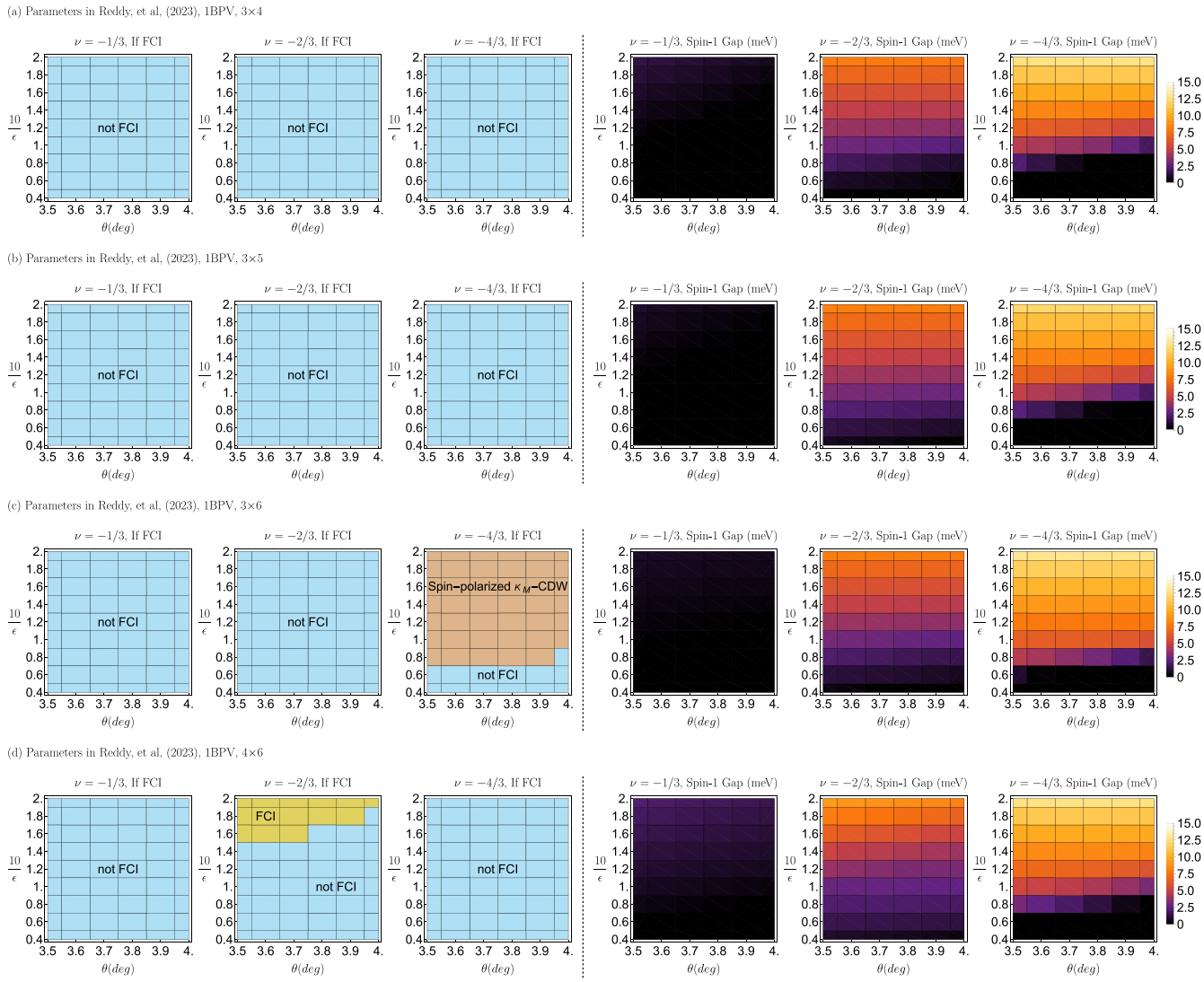

FIG. 24. The summary of 1BPV spin-1 gaps for the parameter values of Ref. [28] for the system sizes of 3×4, 3×5, 3×6, and 4×6. In the leftmost three figures of each row, green ("FCI") labels the region that satisfies the criterion in Prop. 1, and blue ("not FCI") means that we do not see clear signatures of FCI or maximally spin-polarized CDW. For $\nu = -4/3$ in (c) for the system size of 3×6, 1BPV results show that the system is in a maximally spin-polarized K_M-CDW phase for relatively large interaction (brown) and for experimental angles $\theta \in [3.5^\circ, 4.0^\circ]$; the K_M-CDW phase is suppressed for the system sizes of 3×4, 3×5, and 4×6 since their momentum meshes do not include the K_M or K'_M point. The rightmost three figures of each row give the spin-1 gaps, which are shown with the same color functions for all plots. If the spin-1 gap is negative, it is set to zero in the plot.

small. Exploiting this small finite-size effect, we perform HF calculations across various values of (V, w) for the system size of 6×6, $\theta = 3.7^\circ$, and $\xi = 20$ nm. The results are shown in Fig. 19. We choose $\epsilon = 5$ for $\psi = -91^\circ$ [28] and $\epsilon \approx 16.67$ for $\psi = -107.7^\circ$ [29], since $\epsilon = 5$ and $\epsilon = 50/3 \approx 16.67$ are deep in the FCI region at $\nu = -2/3$ in later ED calculations for the parameters in Refs. [28] and [29], respectively. As shown in Fig. 19, the CI is robust as long as the parameters do not differ too much from those in Refs. [28] and [29].

In Fig. 20, we perform the translationally invariant subspace 2BPV Hartree-Fock calculations beyond $\nu = -1$, and reasonably the results are not reliable. Specifically, for the parameters in Ref. [28] in Fig. 20(a), the nonmagnetic states for $\nu > -0.4$ are consistent with experiments [24–27], but the fact that the ferromagnetism persists to $\nu = -2$ is different from the experiments, meaning that the calculation is not completely reliable. For the parameters in Ref. [29] in Fig. 20(b), the ferromagnetic ground states start from nearly zero ν and persist to $\nu = -1.6$, which is not consistent with experiments, meaning that the calculation is not reliable.

As last, we also perform the 1BPV Hartree-Fock calculations for H_h with $\xi = 20$ nm at $\nu = -1$ as shown in Eq. (21). The ground states are always spin polarized and thus has nonzero Chern number for $\theta \in [3.5^\circ, 4.0^\circ]$, $\epsilon \in [5, 25]$ and both sets of parameters in Refs. [28] and [29]. CI at $\nu = -1$ was also found in the 1BPV HF calculation in Ref. [16] outsides the experimental angle range. Therefore, the 1BPV calculations missed the IVC-K_M states for parameters in Ref. [28] and the Ch $= 0$ states for the parameters in Ref. [29]

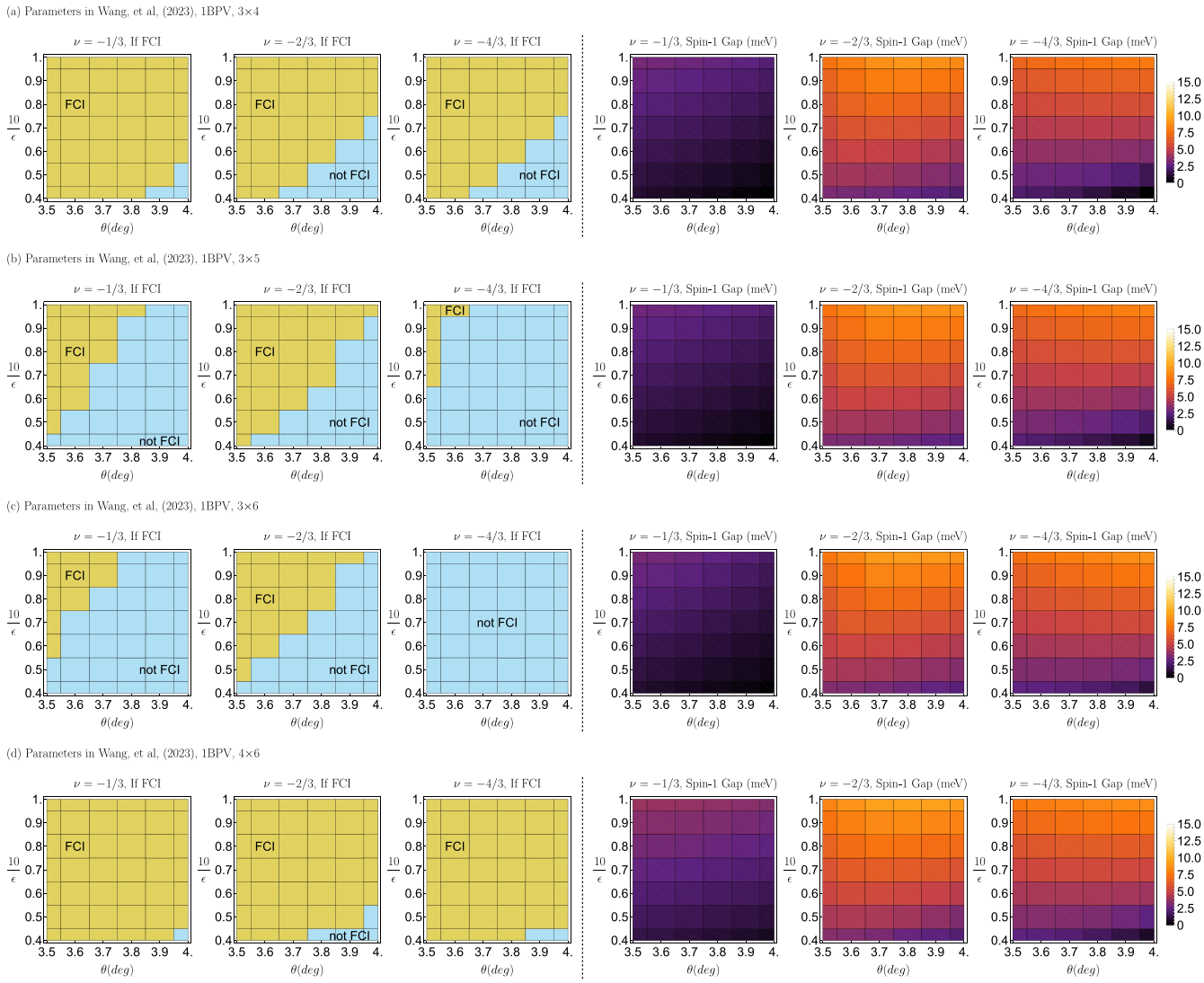

FIG. 25. The summary of 1BPV spin-1 gaps for the parameter values of Ref. [29] for the system sizes of 3×4, 3×5, 3×6, and 4×6. In the leftmost three figures of each row, green ("FCI") labels the region that satisfies the criterion in Prop. 1, and blue ("not FCI") means that we do not see clear signatures of FCI or maximally spin-polarized CDW. The rightmost three figures of each row give the spin-1 gaps, which are shown with the same color functions for all plots. If the spin-1 gap is negative, it is set to zero in the plot.

in the 2BPV results (Fig. 15), indicating the importance of the remote bands.

APPENDIX D: 1BPV ED RESULTS

In this Appendix, we provide more in-depth analysis of the 1BPV ED results. Before going into details, we first present the definitions of the spinful and spin-1 gaps of the model that we study.

Definition 1 (Spinful gap). Given a fixed particle number, the spinful gap of the system with the spin-U(1) symmetry and TR symmetry is defined as the energy difference between the lowest-energy state in all $S_z \neq S_{\max}$ sectors and the lowest-energy state in the $S_z = S_{\max}$ sector (former minus latter), where we only consider $S_z \geqslant 0$ owing to the TR symmetry.

Definition 2 (Spin-1 gap). Given a fixed particle number, the spin-1 gap of the system with the spin-U(1) symmetry and TR symmetry is defined as the energy difference between the lowest-energy state in the $S_z = S_{\max} - 1$ sector and the lowest-energy state in the $S_z = S_{\max}$ sector (former minus latter), where we only consider $S_z \geqslant 0$ owing to the TR symmetry.

We note that in the 1BPV case, the maximally spin-polarized sector at $\nu = -4/3$ has the same spin as the maximally spin-polarized sector at $\nu = -2/3$.

1. Spin-1 gap as an approximation of the spinful gap

We first benchmark that the spin-1 gap is a good approximation of the spinful gap at the fractional fillings of interest in our 1BPV calculations.

(i) System size of 3×4 (1BPV): When the spinful gaps are positive, the ratio between the spinful gaps and spin-1 gaps (former divided by latter) in average takes value of 0.36 at $\nu = -1/3$, of 0.93 at $\nu = -2/3$ and of 1 at $\nu = -4/3$ for the parameters of Ref. [28], as shown in Figs. 22(a) and 24(a),

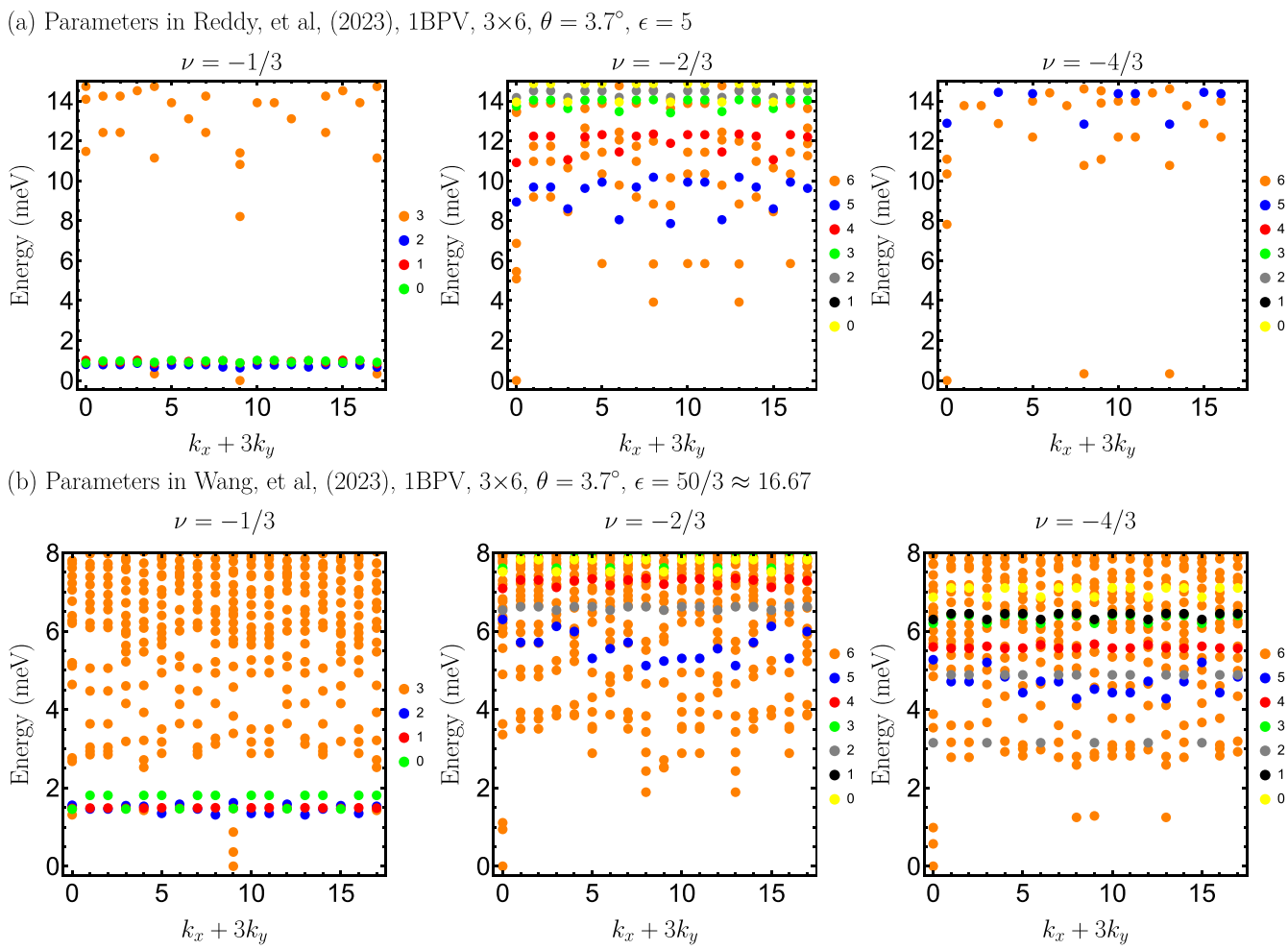

FIG. 26. The 1BPV ED many-body spectrum for the system size of 3×6. The dots of different colors correspond to different spin S_z sectors. The ground-state energy is chosen to be zero. In the partially spin-polarized sectors, we only show the lowest-energy state for each momentum and each spin, which are enough to determine the spinful and spin-1 gaps. Here, the FCI states, if they occur, have momenta at $(k_x, k_y) = (0, 3), (0, 3), (0, 3)$ at $\nu = -1/3$, and have momenta at $(k_x, k_y) = (0, 0), (0, 0), (0, 0)$ for $\nu = -2/3$ and $\nu = -4/3$. In (a), the maximally spin-polarized sector at $\nu = -1/3$ shows a CDW with wavevector K_M, since it has three ground states at (1,1), (0,3), and (2,5), which have relative momentum differences $\pm\mathrm{K}_M$. In (a), the ground states at $\nu = -4/3$ also show a maximally spin-polarized CDW with wavevector K_M, as it has three ground states at (0,0), (2,2), and (1,4), which have relative momentum differences $\pm\mathrm{K}_M$ In (b), although the lowest-energy three states at $\nu = -1/3, -2/3, -4/3$ have the right FCI momentum, their spread is larger than the gap between the third lowest-energy state and the fourth lowest-energy state in the maximally spin-polarized sector; thus they are not FCI states according to the criterion in Prop. 1. At $\nu = -4/3$ of (b), if we combine the third lowest-energy state at (0,0) with the lowest energy states at (2,2) and (1,4), this combination would give us a K_M-CDW around energy 1 meV; however, such combination is not reliable since we have a state at (0,3) that has close to 1 meV.

respectively. For the parameters of Ref. [29], the same ratio in average takes value of 0.65 at $\nu = -1/3$, of 0.98 at $\nu = -2/3$ and of 0.71 at $\nu = -4/3$, as shown in Figs. 23(a) and 25(a), respectively.

(ii) System size of 3×5 (1BPV): When the spinful gaps are positive, the ratio between the spinful gaps and spin-1 gaps (former divided by latter) takes value of 1 at $\nu = -1/3$, of 0.95 at $\nu = -2/3$ and of 1 at $\nu = -4/3$ for the parameters of Ref. [28], as shown in Figs. 22(b) and 24(b), respectively. For the parameters of Ref. [29], the same ratio in average take the value of 0.97 at $\nu = -1/3$, of 1 at $\nu = -2/3$ and of 1 at $\nu = -4/3$, as shown in Figs. 23(b) and 25(b), respectively.

(iii) System size of 3×6 (1BPV): We choose $\theta = 3.7°$ and $\epsilon = 5$ as the representative point for the parameter values in Ref. [28], and $\theta = 3.7°$ and $\epsilon \approx 16.67$ ($10/\epsilon = 0.6$) for the parameters of Ref. [29], as those points are in the ($\nu = -1$)-CI region shown in Fig. 4 of the main text and in the ($\nu = -2/3$)-FCI region for 4×6 (Figs. 24 and 25). As shown by Fig. 26(a), which is for the parameters in Ref. [28], the spinful gap and spin-1 gap are equal for all three fillings—they take values 0.63 meV, 7.86 meV, and 12.84 meV for $\nu = -1/3$, $\nu = -2/3$, and $\nu = -4/3$, respectively. As shown by Fig. 26(b), which is for the parameters in Ref. [29], the spinful gap and spin-1 gap are equal for $\nu = -1/3$ and $\nu = -2/3$, and they take values 1.31 meV and 5.12 meV for $\nu = -1/3$

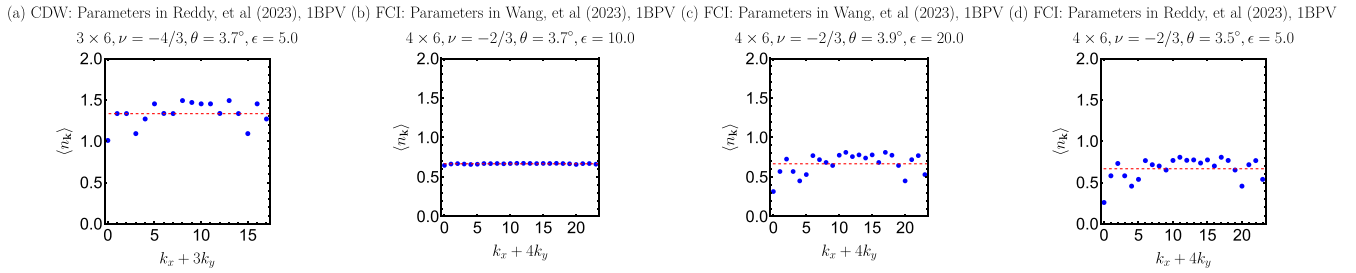

FIG. 27. Representative plots of the $\langle n_{\boldsymbol{k}}\rangle$ in Eq. (D1). In (a), we plot it for the K_M-CDW states at $\nu=-4/3$ for $\theta=3.7^\circ$, $\epsilon=5$, the 3×6 system size, and the parameters in Ref. [28]. In (a), we consider for $\langle n_{\boldsymbol{k}}\rangle$ the three K_M-CDW states—the maximally spin-polarized lowest-energy states at the CDW momenta (0,0), (2,2), and (1,4) as shown in Fig. 26(a). In (b)-(d), we plot $\langle n_{\boldsymbol{k}}\rangle$ for the FCI states at $\nu=-2/3$, where ρ is the projection operator for the subspace spanned by three-FCI states—the maximally spin-polarized lowest-energy states at the FCI momenta $(k_x,k_y)=(0,0),(0,2),(0,4)$. The red dashed line mark the mean value of $\langle n_{\boldsymbol{k}}\rangle$, which equals to $-\nu$.

and $\nu=-2/3$, respectively; the spinful gap and spin-1 gap are not identical but similar for $\nu=-4/3$—they take values 3.15 meV and 4.28 meV, respectively, and the ratio (former divided by latter) reads 0.74.

Our results on 3×4 and 3×5 the spin-1 gap becomes better approximation of the spinful gap as sizes grow; the trend persists to our examples on 3×6, except for $\nu=-4/3$ for parameters in Ref. [29]. Nevertheless, for $\nu=-4/3$ for parameters in Ref. [29], the ratio between the spin-1 gap and spinful gap is still close to 1 for the largest size 3×6. Thus, for the 1BPV calculations, our results on 3×4 and 3×5 and our examples on 3×6 clearly show that the spin-1 gap is a good approximation of the spinful gap.

2. Ground states at $\nu=-1/3,-2/3,-4/3$

The 1BPV ED calculations for the system sizes of 3×4, 3×5, 3×6, and 4×6 are summarized in Figs. 24 and 25 for

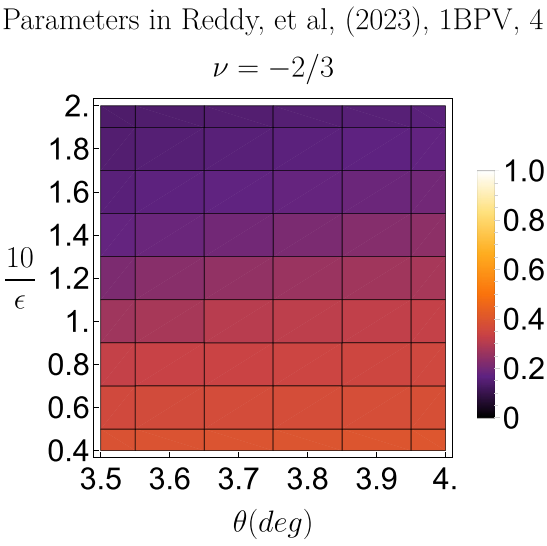

FIG. 28. 1BPV ED calculations of the standard deviation of the $\langle n_{\boldsymbol{k}}\rangle$ in Eq. (D1) for the system size of 4×6 by using the parameters in Ref. [28] at $\nu=-2/3$. $\langle n_{\boldsymbol{k}}\rangle$ is plotted for the maximally spin-polarized lowest-energy states at the FCI momenta—$(k_x,k_y)=(0,0),(0,2),(0,4)$.

both sets of parameters in Refs. [28] and [29]. We first discuss the ground states at $\nu=-1/3,-2/3,-4/3$.

(i) $\nu=-2/3$ (1BPV): As shown in Figs. 24 and 25, the finite-size effect on the FCI region at $\nu=-2/3$ is non-negligible, so we choose the largest system size 4×6 to determine the $\nu=-2/3$ FCI region. The $\nu=-2/3$ FCI region is roughly $\epsilon\in[5,6.25]$ for the parameters of Ref. [28]; the FCI region at $\nu=-2/3$ basically covers the entire phase diagram in Fig. 25 for the parameters of Ref. [29].

(ii) $\nu=-4/3$ (1BPV): In the parameter region where $\nu=-2/3$ hosts an FCI, the 1BPV ED calculation shows that the ground states at $\nu=-4/3$ exhibit a positive spin-1 gap for both sets of parameters in Refs. [28] and [29], indicating maximally spin-polarized ground states. In this region, $\nu=-4/3$ is in the spin-polarized K_M-CDW phase for the parameter values in Ref. [28], which is indicated by the fact that we have three nearly degenerate ground states for $\nu=-4/3$ in Fig. 26 with a considerable gap ~7 meV and their momentum difference is $\pm\boldsymbol{K}_M=\pm(\frac{1}{3}\boldsymbol{b}_1+\frac{2}{3}\boldsymbol{b}_2)$ for the system size of 3×6. It is not an FCI since the three FCI states at the system size of 3×6 are all in the (0,0) sector for $\nu=-4/3$, and such K_M-CDW phase cannot be detected for the system sizes of 3×4, 3×5, and 4×6 as their momentum meshes do not include the K_M point. For the parameter values in Ref. [29], $\nu=-4/3$ are mostly in the FCI phase for the parameters that give FCI at $\nu=-2/3$, as shown in Fig. 30 for $\theta=3.5^\circ$ and $\epsilon=10$ deep in the FCI region at $\nu=-2/3$.

(iii) $\nu=-1/3$ (1BPV): In the parameter region where $\nu=-2/3$ hosts an FCI, the 1BPV ED calculation shows that the ground states at $\nu=-1/3$ exhibit a positive spin-1 gap for both sets of parameters in Refs. [28] and [29], indicating maximally spin-polarized ground states. In the parameter region where $\nu=-2/3$ hosts an FCI, if we focus on the fully spin-polarized sector of $\nu=-1/3$, we have a K_M-CDW phase for the system size of 3×6 for the parameters of Ref. [28] (Fig. 26), which is consistent with the results in Ref. [28]. However, the partially spin-polarized sector has energies too low to solidly claim the presence of the fully spin-polarized K_M-CDW as the ground state (finite-size effects or disorder might change this). For the parameter values in Ref. [29], $\nu=-1/3$ is mostly in the FCI phase for the parameters that

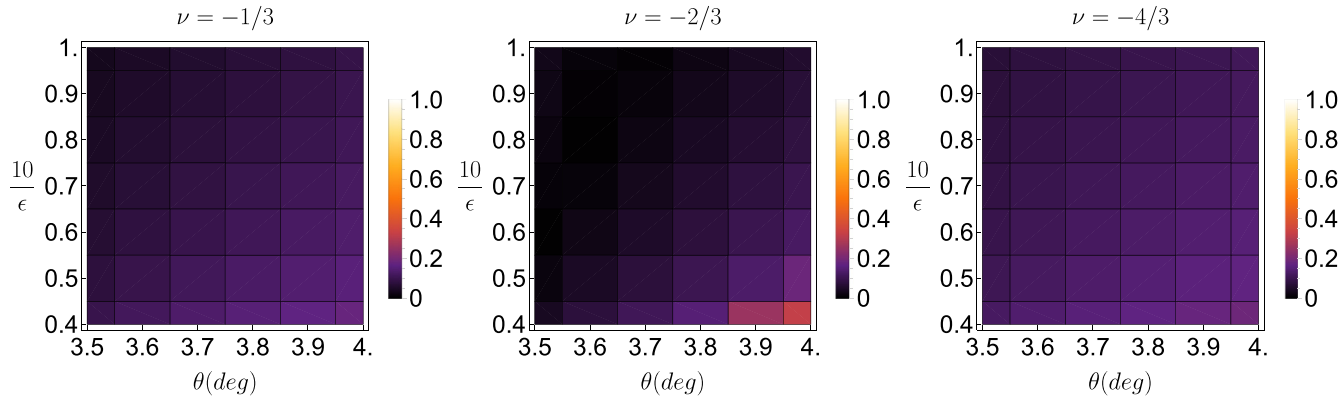

FIG. 29. 1BPV ED calculations of the standard deviation of the $\langle n_{\boldsymbol{k}} \rangle$ in Eq. (D1) for the system size of 4×6 by using the parameters in Ref. [29]. $\langle n_{\boldsymbol{k}} \rangle$ is plotted for the maximally spin-polarized lowest-energy states at the FCI momenta—$(k_x, k_y) = (0, 0), (0, 2), (0, 4)$ at $\nu = -1/3, -2/3, -4/3$.

give FCI at $\nu = -2/3$, as shown in Fig. 30 for $\theta = 3.5^\circ$ and $\epsilon = 10$ deep in the FCI region at $\nu = -2/3$, where the $\nu = -1/3$ FCI phase is consistent with the 1BPV ED calculations in Ref. [29].

We now discuss the qualities of the FCI states based on $\langle n_{\boldsymbol{k}} \rangle$, where

$$\langle n_{\boldsymbol{k}} \rangle = \frac{\mathrm{Tr}[\rho n_{\boldsymbol{k}}]}{\mathrm{Tr}[\rho]}, \tag{D1}$$

where ρ is the projection operator for the states of interest; for three FCI states $|\psi_i^{FCI}\rangle$ with $i = 1, 2, 3$ (such as $|1\rangle$, $|2\rangle$, and $|3\rangle$ at $\nu = -2/3$ in Fig. 30), ρ reads

$$\rho = \sum_{i=1}^{3} |\psi_i^{FCI}\rangle\langle\psi_i^{FCI}| . \tag{D2}$$

$n_{\boldsymbol{k}} = \sum_{n,\eta} \widetilde{\gamma}^{\dagger}_{\eta,n,\boldsymbol{k}} \widetilde{\gamma}_{\eta,n,\boldsymbol{k}}$ is the hole number operator at $\boldsymbol{k}$ (n only takes one value in this section). As a benchmark, we show in Fig. 27(a) the $\langle n_{\boldsymbol{k}} \rangle$ for the K_M-CDW states at $\nu = -4/3$ for $\theta = 3.7^\circ$, $\epsilon = 5$, the 3×6 system size, and the parameters in Ref. [28]. As we can see, $\langle n_{\boldsymbol{k}} \rangle$ the K_M-CDW states have considerable fluctuations with standard deviation 0.144. In Fig. 27(b), we show $n_{\boldsymbol{k}}$ of the FCI states deep in the FCI region at $\nu = -2/3$ for the 4×6 system size and the parameters in Ref. [29], which is very uniform with standard deviation 0.006. If we move close to the boundary of the FCI region, the fluctuations become much stronger—standard deviation increases to 0.134 as shown in Fig. 27(c), which is close to the fluctuations of the CDW. As shown by Fig. 27(d), the quality of the FCI states at $\nu = -2/3$ for the 4×6 system size and the parameters in Ref. [28] (standard deviation

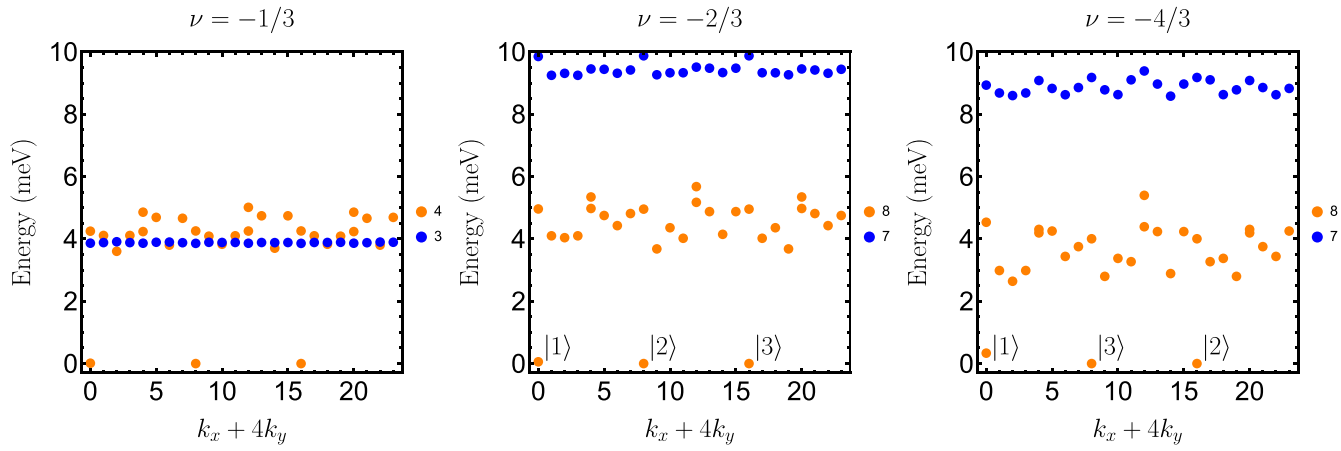

FIG. 30. The 1BPV ED many-body spectrum for the system size of 4×6. The dots of different colors correspond to different spin S_z sectors. The ground-state energy is chosen to be zero. Here we only show the lowest-energy state per momentum for the sector $S_z = S_{\mathrm{max}} - 1$ (using blue dots). For the sector $S_z = S_{\mathrm{max}}$ (using orange dots), we show the lowest-energy state per momentum, except for $k_x = 0$ where we show the two lowest-energy states per momentum in order to make sure there are two states per momentum for the FCI momenta $(k_x, k_y) = (0, 0), (0, 2), (0, 4)$. According to the criterion in Prop. 1, FCI states exist for all three fillings for the parameters of interest. $|1\rangle$, $|2\rangle$, and $|3\rangle$ label the threefold degenerate ground states at $\nu = -2/3$ and $\nu = -4/3$ for the FCI, which are used in verifying the approximate PH symmetry between $\nu = -2/3$ and $\nu = -4/3$ in Eq. (D3).

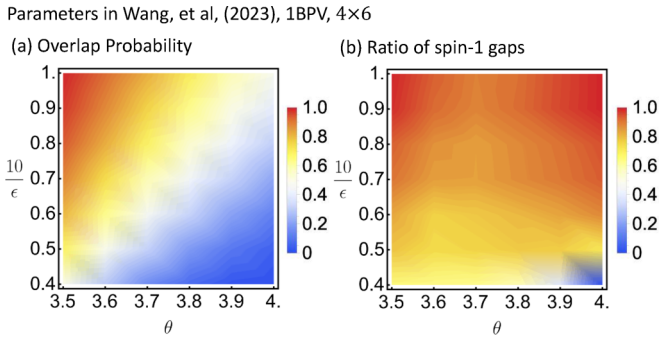

FIG. 31. (a) The overlap probability of the rank-3 lowest-energy subspaces with the FCI quantum numbers between $\nu = -2/3$ and $\nu = -4/3$ [see Eq. (D3)] for the system size of 4×6, the parameters in Ref. [29], and for the 1BPV calculations. Explicitly, the rank-3 lowest-energy subspace with the FCI quantum numbers is spanned by the lowest-energy states at the FCI momenta $(k_x, k_y) = (0, 0), (0, 2), (0, 4)$ in the maximally spin-polarized sector at $\nu = -2/3$ or $\nu = -4/3$, as shown in Fig. 30. If the criterion in Prop. 1 is satisfied, the three states at $\nu = -2/3$ or $\nu = -4/3$ are in the FCI phase, which is true for most parts of the phase diagram, as shown in Fig. 25(d). (b) The ratio between the spin-1 gaps at $\nu = -4/3$ and $\nu = -2/3$ (former divided by latter) for the system size of 4×6, the parameters in Ref. [29], and for the 1BPV calculations.

of n_k is 0.137) is as bad as those close to the boundary of the FCI region for the same size and the parameters in Ref. [29].

We further calculate $\langle n_k \rangle$ for the maximally spin-polarized lowest-energy states at the FCI momenta—$(k_x, k_y) = (0, 0), (0, 2), (0, 4)$—in the phase diagrams that involve FCI at the 4×6 system size as shown in Figs. 28 and 29. As shown in Fig. 28 [compared to Fig. 24(d)], the standard deviation of $\langle n_k \rangle$ at $\nu = -2/3$ does minimize in the region where the three states become FCI according to the criterion in Prop. 1 for the parameters in Ref. [28]; the same

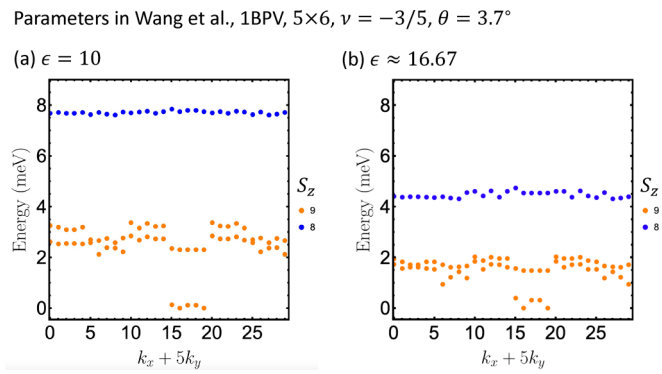

FIG. 32. The 1BPV ED many-body spectrum for the system size of 5×6, $\nu = -3/5$ at $\theta = 3.7°$ with $\epsilon = 10$ (a) and $\epsilon = 16.67$ (b). The dots of different colors correspond to different spin S_z sectors. The ground-state energy is chosen to be zero. In the partially spin-polarized sectors, we only show the lowest-energy state for each momentum and spin $S_{\max} - 1$, which are enough to determine the spin-1 gaps. Here, the FCI states, if they occur, have momenta at $(k_x, k_y) = (0, 3), (1, 3), (2, 3), (3, 3), (4, 3)$. In both (a) and (b), we have clear FCI ground states and large spin-1 gap.

holds for each for the three fillings $\nu = -1/3, -2/3, -4/3$ for the parameters in Ref. [29] as shown in Fig. 29. The FCI states at $\nu = -1/3, -2/3, -4/3$ for the parameters in Ref. [29] can have good quality—standard deviations of $\langle n_k \rangle$ take values in [0.037, 0.166] at $\nu = -1/3$, in [0.002, 0.134] at $\nu = -2/3$ and in [0.077, 0.181] at $\nu = -4/3$. Yet, the FCI states at $\nu = -2/3$ for the parameters in Ref. [28] has large fluctuations in $\langle n_k \rangle$ with the standard deviation in the range [0.136, 0.169], well beyond the minimum values for the FCI states for the parameters in Ref. [29].

In the parameter region where $\nu = -2/3$ hosts an FCI, the ground states at $\nu = -1/3$ and $\nu = -4/3$ are maximally spin polarized in 1BPV calculations for both sets of parameters in Refs. [28] and [29]. Although the finite-size effects on the FCI region are substantial, the finite size effect of the spin-1 gap is small: the spin-1 gap does not change significantly for all four different system sizes. In the following, we compare the magnetic stability of the ground states at different fillings based on the spin-1 gaps.

3. Magnetic stability at $\nu = -4/3$ and $\nu = -2/3$

We now compare the magnetic stability of the ground states between $\nu = -4/3$ and $\nu = -2/3$ first in the 1BPV calculations.

(i) $\nu = -2/3$ versus $\nu = -4/3$ for the parameters in Ref. [28] (1BPV): We find that the spin-1 gap at $\nu = -4/3$ is larger than that at $\nu = -2/3$; specifically, in the $\nu = -2/3$ FCI region, the ratio of the spin-1 gap at $\nu = -4/3$ and $\nu = -2/3$ takes values in the range [1.59,1.72] for 3×4, [1.49,1.59] for 3×5, [1.62,1.77] for 3×6, and [1.37,1.64] for 4×6.

(ii) $\nu = -2/3$ versus $\nu = -4/3$ for the parameters in Ref. [29] (1BPV): We find that the spin-1 gap at $\nu = -4/3$ is similar to that at $\nu = -2/3$; specifically, in the $\nu = -2/3$ FCI region, the ratio of the spin-1 gap at $\nu = -4/3$ and $\nu = -2/3$ takes values in the range [0.60,0.92] for 3×4, [0.61,0.93] for 3×5, [0.74,1.00] for 3×6, and [0.71,0.93] for 4×6.

These 1BPV results show that the magnetic stability at $\nu = -4/3$ cannot be significantly weaker than that at $\nu = -2/3$, which is dramatically different from the clearly nonmagnetic state at $\nu = -4/3$ and the magnetic FCI at $\nu = -2/3$ observed in the experiments [24–27].

In the 1BPV results, the similarity between the spin-1 gaps at $\nu = -4/3$ and $\nu = -2/3$ for the parameter values in Ref. [29] can be understood from the approximate PH symmetry roughly for $\theta \in [3.5°, 3.7°]$ and for $10/\epsilon \in [0.8, 1]$. As discussed in Sec. III B and Appendix B 2, $\nu = -4/3$ and $\nu = -2/3$ is allowed to be PH partners in the 1BPV case, as we have two bands in total (PH transforms ν to $-2 - \nu$). Let us first take $\theta = 3.5°$ and $\epsilon = 10$ as an example. As shown in Fig. 30 for $\theta = 3.5°$ and $\epsilon = 10$, we have the extremely similar the low-energy spectra (including the $S_z = S_{\max} - 1$ sector) at $\nu = -2/3$ and $\nu = -4/3$, indicating the approximate (almost exact) PH symmetry. We can be more quantitative and compute the overlap probability between the ground states at $\nu = -2/3$ and the PH-transformed ground states at $\nu = -4/3$ at the system size 4×6. We note that the ground states at the system size 4×6 for $\theta = 3.5°$ and $\epsilon = 10$ are FCI states at both $\nu = -2/3$ and $\nu = -4/3$, and the FCI

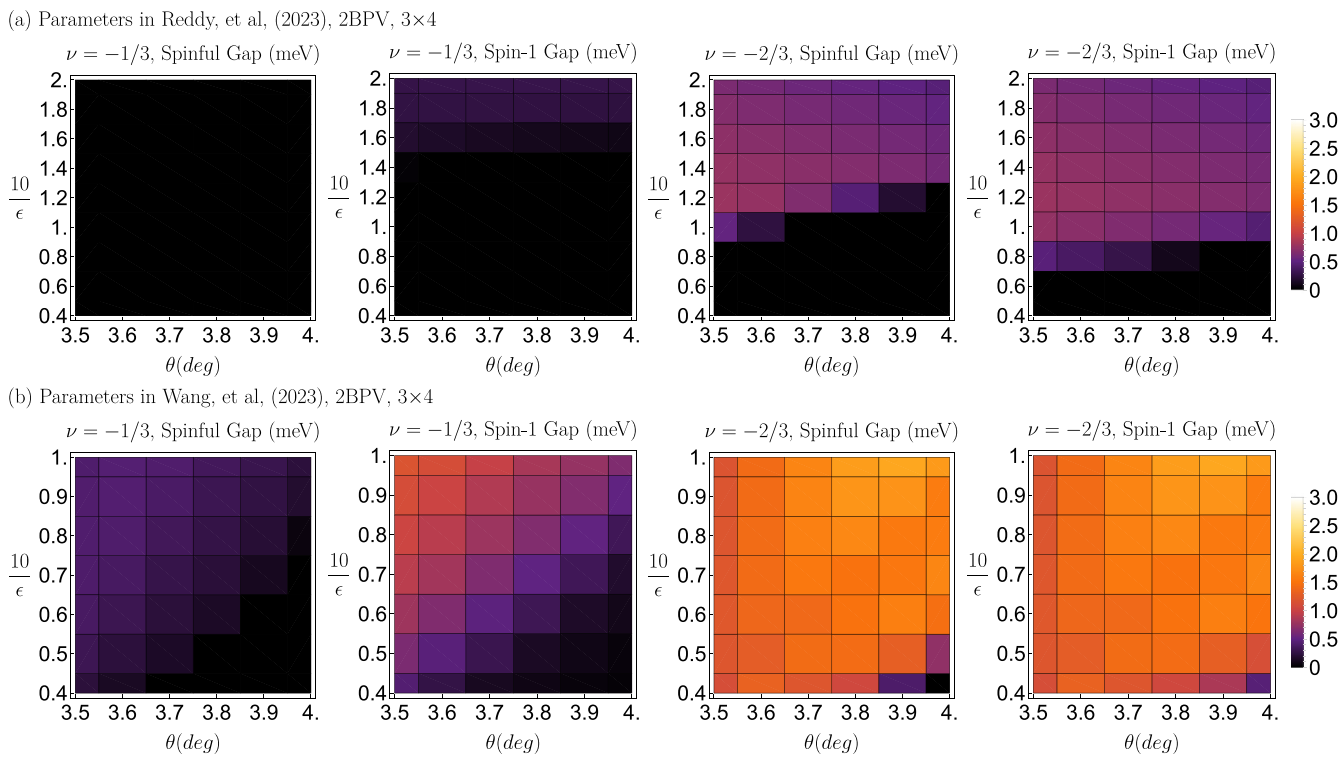

FIG. 33. The comparison of the spinful gap and spin-1 gap for 3×4 in 2D 2BPV ED calculations at $\nu = -1/3$ and $\nu = -2/3$ (a) using the parameters of Ref. [28] and (b) using the parameters of Ref. [29]. Spinful and spin-1 gaps are set to zero if they are negative.

momenta are (0,0), (0,2), and (0,4) at both $\nu = -2/3$ and $\nu = -4/3$. We label the three FCI states at ν by $i = 1, 2, 3$, and making sure that $|\nu = -2/3, i\rangle$ and $\mathcal{C}|\nu = -4/3, i\rangle$ have the same momentum as shown in Fig. 30, where $\mathcal{C}$ is the PH transformation operator defined in Eq. (15). We obtain

$$\frac{1}{3}\mathrm{Tr}\Bigg[\sum_{i=1}^{3}|\nu=-2/3,i\rangle\langle\nu=-2/3,i| \times\sum_{j=1}^{3}(\mathcal{C}|\nu=-4/3,j\rangle)(\langle\nu=-4/3,j|\mathcal{C}^{-1})\Bigg] =\frac{1}{3}\sum_{i=1}^{3}|\langle\nu=-2/3,i|\mathcal{C}|\nu=-4/3,i\rangle|^2=0.95, \quad \text{(D3)}$$

which is close to 1, verifying the approximate PH symmetry. Here we have used $\langle\nu = -2/3, i|\mathcal{C}|\nu = -4/3, j\rangle = 0$ for $i \neq j$ owing to the different momenta, and we also have used

$$|\langle\nu=-2/3,1|\mathcal{C}|\nu=-4/3,1\rangle|^2=0.96,$$
$$|\langle\nu=-2/3,2|\mathcal{C}|\nu=-4/3,2\rangle|^2=0.95,$$
$$|\langle\nu=-2/3,3|\mathcal{C}|\nu=-4/3,3\rangle|^2=0.95. \quad \text{(D4)}$$

For completeness, we give in Fig. 31(a) the phase diagram indicating the overlap quantifying the approximate PH symmetry between $\nu = -2/3$ and $\nu = -4/3$ in the 1BPV calculations. We note that the three states $|\nu, 1\rangle$, $|\nu, 2\rangle$, and $|\nu, 3\rangle$ with $\nu = 2/3$ or $\nu = -4/3$ are chosen to be the lowest-energy states at the FCI momenta $(k_x, k_y) = (0, 0), (0, 2), (0, 4)$ in the maximally spin-polarized sector. In the phase diagram, $|\nu, 1\rangle$, $|\nu, 2\rangle$, and $|\nu, 3\rangle$ are not always the absolute ground states, but they become the absolute ground states and form FCI for most part of the phase diagram as shown in Fig. 25(d). In Fig. 31(b), we can see extreme similarity between the spin-1 gaps at $\nu = -3/4$ and $\nu = -2/3$ in the top left corner, where the approximate PH symmetry is good. Specifically, for $\theta \in [3.5°, 3.7°]$ and for $10/\epsilon \in [0.8, 1]$, the overlap probability in Eq. (D3) is no less than 0.66, indicating the fairly good approximate PH symmetry [Fig. 31(a)], and the ratio between the spin-1 gaps at $\nu = -3/4$ and $\nu = -2/3$ (former divided by latter) is no less than 0.84 [Fig. 31(b)]. Nevertheless, the extreme similarity between the spin-1 gaps at $\nu = -3/4$ and $\nu = -2/3$ in the top right corner of Fig. 31(b) (i.e., θ close to 4.0° and $10/\epsilon$ close to 1) happens when the overlap probability in Eq. (D3) is relatively small (smaller than ∼0.5), of which the explanation we leave for future work.

4. Magnetic stability at $\nu = -1/3$ and $\nu = -2/3$

We now compare the magnetic stability at $\nu = -1/3$ and $\nu = -2/3$ based on the spin-1 gaps in the 1BPV calculations. As itemized in the following, when $\nu = -2/3$ is an FCI, we find that the spin-1 gap at $\nu = -1/3$ is indeed considerably smaller than that at $\nu = -2/3$ for both sets of parameter values of Refs. [28,29], although the difference between $\nu = -1/3$ and $\nu = -2/3$ is reduced at larger system sizes, compared to the numbers reported in Refs. [28,29] on smaller systems.

(i) $\nu = -2/3$ versus $\nu = -1/3$ for the parameters in Ref. [28] (1BPV): In the $\nu = -2/3$ FCI region, the ratio between the spin-1 gap at $\nu = -1/3$ and that at $\nu = -2/3$

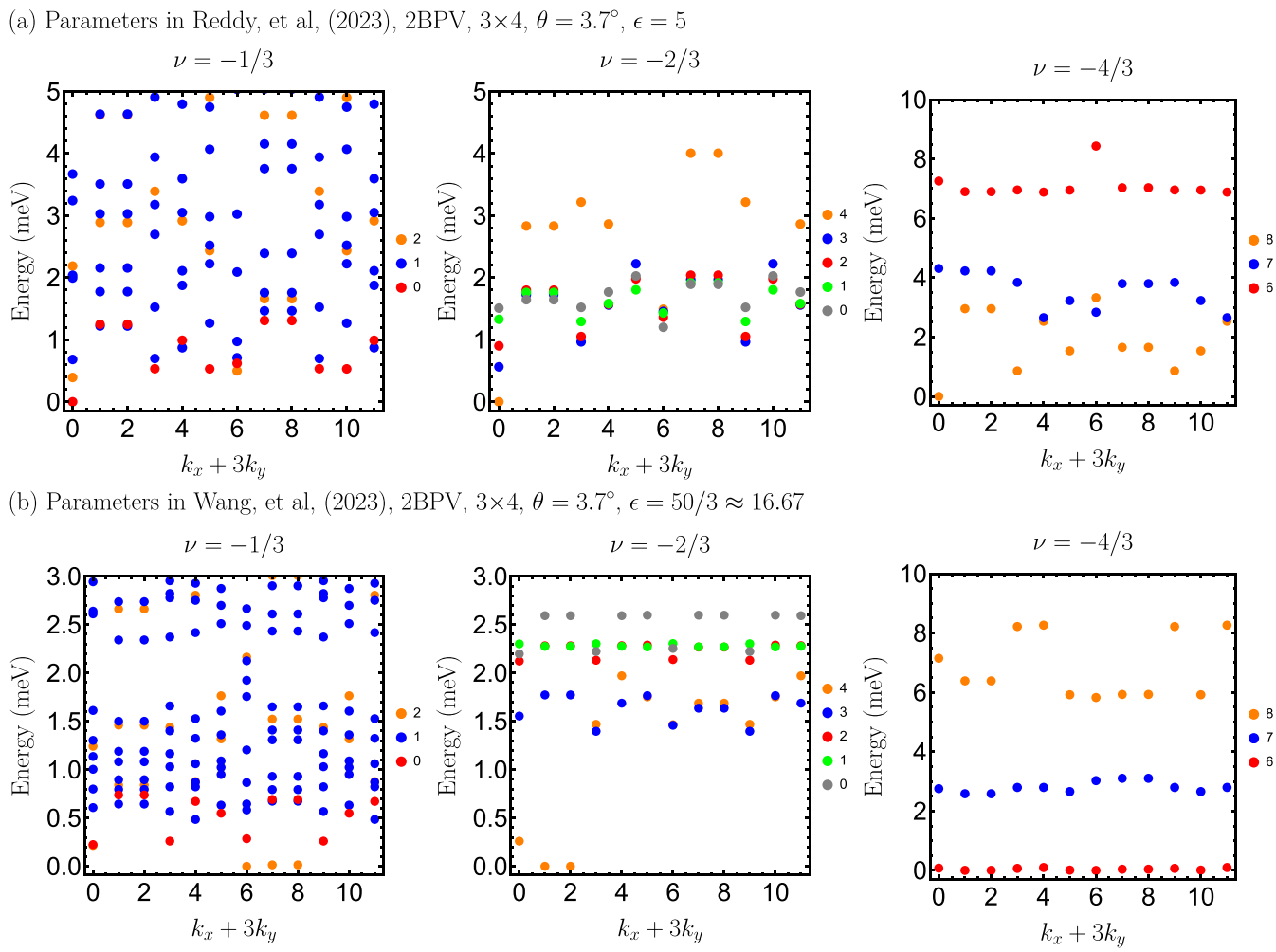

FIG. 34. The many-body spectrum at 3×4 for 2BPV at $\nu = -1/3, -2/3, -4/3$ (a) for the parameters of Ref. [28] and (b) for the parameters of Ref. [29]. For $\nu = -2/3$ and for the spin-zero sector at $\nu = -1/3$, we only show the lowest-energy state for each momentum. For $\nu = -4/3$, we only show three spin sectors, and the lowest-energy state for each momentum and for each spin. Note that for this system size $S^{\text{2BPV}}_{\text{max}} = 8$ and $S^{\text{1BPV}}_{\text{max}} = 4$; the $S^{\text{1BPV}}_{\text{max}} = 4$ sector at $\nu = -4/3$ has Hilbert dimension about 2.3 billion per momentum, which is hard to address. The ground-state energy is chosen to be zero. Here, the FCI states, if any, should have momenta at $(k_x, k_y) = (0, 2), (1, 2), (2, 2)$ at $\nu = -1/3$, and have momenta at $(k_x, k_y) = (0, 0), (1, 0), (2, 0)$ for $\nu = -2/3$ and $\nu = -4/3$. According to the criterion in Prop. 1, the FCI states exist for both $\nu = -1/3$ and $\nu = -2/3$ in (b). However, one can clearly see the minuscule FCI gap at $\nu = -1/3$ and the large FCI gap at $\nu = -2/3$.

takes the value in the range [0.07, 0.17] for 3×4, [0.02, 0.10] for 3×5, [0.07, 0.09] for 3×6, and [0.18, 0.23] for 4×6. Ref. [28] finds an order-of-magnitude difference between the spinful gaps at $\nu = -1/3$ and $\nu = -2/3$ for the system size of 12 unit cells for $\theta = 3.5°$ and $\epsilon = 5$, which is consistent with our 3×4 spinful gaps (Fig. 22) and spin-1 gaps.

(ii) $\nu = -2/3$ versus $\nu = -1/3$ for the parameters in Ref. [29] (1BPV): In the $\nu = -2/3$ FCI region, the ratio between the spin-1 gap at $\nu = -1/3$ and that at $\nu = -2/3$ takes the value in the range [0.17,0.41] for 3×4, [0.16,0.38] for 3×5, [0.16,0.39] for 3×6, and [0.35,0.47] for 4×6. Therefore, increasing the system size does increase the ratio between the spin-1 gaps at $\nu = -1/3$ and $\nu = -2/3$ (former divided by latter), but the effect is not significant enough to rule out the trend that the spin-1 gap at $\nu = -1/3$ is considerably smaller than that at $\nu = -2/3$. Ref. [29] finds the spinful gap at $\nu = -2/3$ is about five times that at $\nu = -1/3$ for $\theta = 3.5°$, $\epsilon = 15$ and the system size of 3×4, which is consistent with our 3×4 spinful gaps (Fig. 23) and spin-1 gaps.

To summarize, the spin-1 gap 1BPV ED results indicate that the magnetic stability at $\nu = -4/3$ cannot be significantly weaker than that at $\nu = -2/3$, which is inconsistent with the experiments, although the fact that the spin-1 gap at $\nu = -1/3$ is much smaller than that at $\nu = -2/3$ is consistent with the nonmangetic or weakly ferromagnetic states at $\nu = -1/3$ in experiments. In addition, the ground states at $\nu = -1/3$ are mostly FCIs for the parameters of Ref. [29] but are mostly K_M-CDW for parameters of Ref. [28]; only the latter is consistent with the topologically trivial states at $\nu = -1/3$ in experiments).

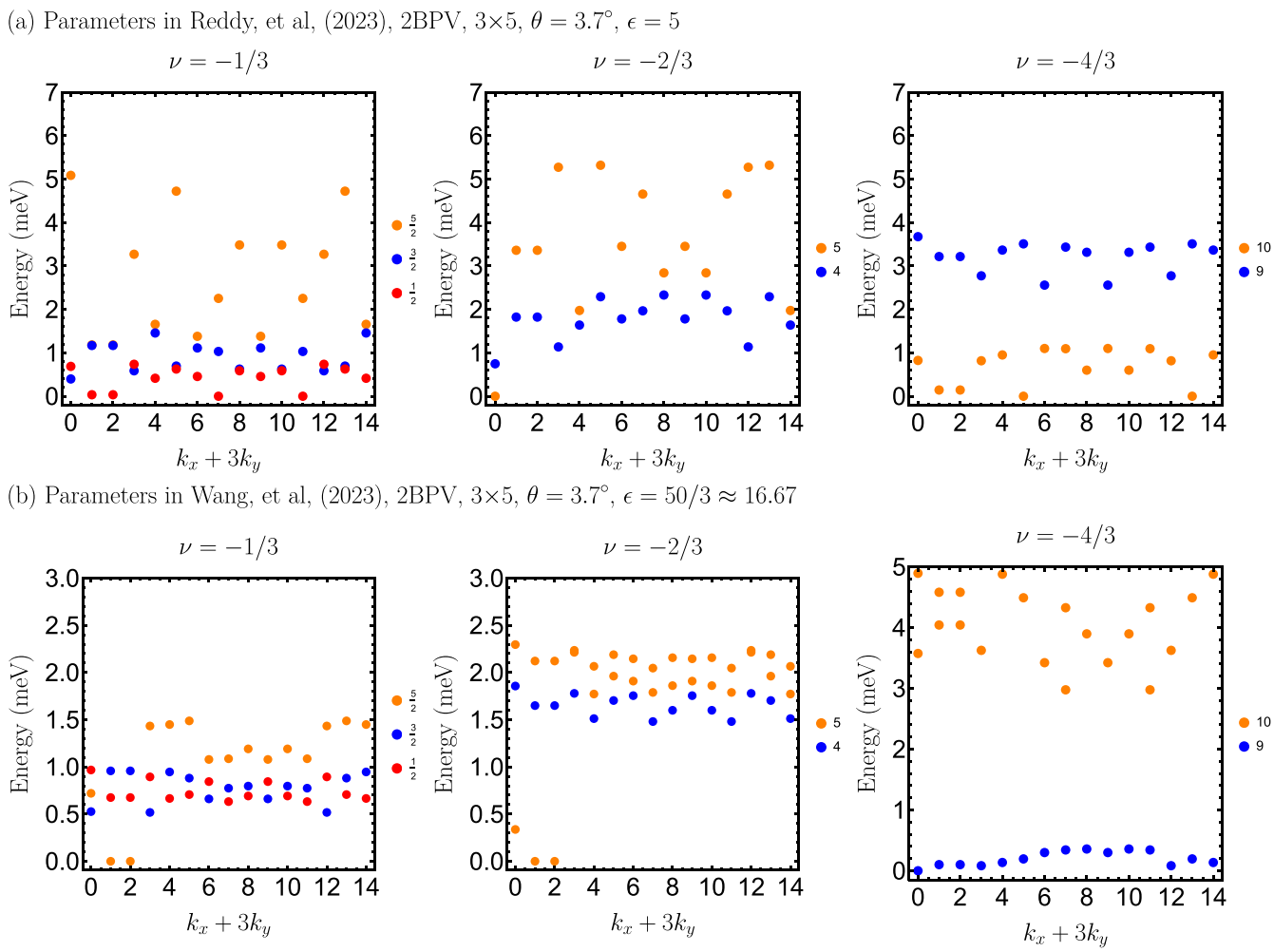

FIG. 35. The many-body spectrum at 3×5 for 2BPV at $\nu = -1/3, -2/3, -4/3$ and for the parameter values specified. We include all spin sectors at $\nu = -1/3$ and the lowest-energy state per momentum in each spin sector to obtain the spinful gap. We only include two spin sectors $S_z = S^{\text{2BPV}}_{\text{max}}, S^{\text{2BPV}}_{\text{max}} - 1$ at $\nu = -2/3, -4/3$ to show the spin-1 gap and the lowest-energy state per momentum per spin, except that we keep two lowest-energy states per momentum in $S_z = S^{\text{2BPV}}_{\text{max}}$ sector for possible FCIs in (b). Here, the FCI states, if occur, have momenta at $(k_x, k_y) = (0, 0), (1, 0), (2, 0)$ at $\nu = -1/3$, $\nu = -2/3$, and $\nu = -4/3$. According to the criterion in Prop. 1, FCI states exist for $\nu = -2/3$ in (b). For $\nu = -1/3$ in (b), it is not an FCI state according to the criterion Prop. 1 for two reasons. First, the lowest three states at the FCI momenta (0,0), (1,0), and (2,0) in the fully spin-polarized sector are not the absolute ground states, since the lowest-energy fully spin-polarized state at (0,0) has higher energy than the partially spin-polarized state at the same momentum, violating the combination of (i) and (ii) in the criterion Prop. 1. Second, the lowest three fully spin-polarized states at the FCI momenta (0,0), (1,0) and (2,0) for $\nu = -1/3$ have a spread larger than the gap between the third lowest state and the 4th lowest state in the fully spin-polarized sector, violating (iii) in the criterion Prop. 1. Therefore, even if the partially spin-polarized states have much higher energies than the three lowest fully spin-polarized states [as $\nu = -2/3$ in (b)], $\nu = -1/3$ in (b) is still not an FCI due to the second reason. We note that lowest two states at momenta (1,0) and (2,0) are guaranteed to be exactly degenerate due to the effective inversion symmetry for $\nu = -1/3$ in (b).

5. $\nu = -3/5$ for parameters in Ref. [29]

In this section, we discuss the FCI states at $\nu = -3/5$ in 1BPV ED results.

FCI states at $\nu = -3/5$ were already observed in Ref. [26] at $\theta = 3.7°$. We find that 1BPV ED calculations with the parameters in Wang *et al.* [37] can clearly show FCI ground states at $\nu = -3/5$ at the experimentally-relevant angle $\theta = 3.7°$ with considerable spin-1 gap (e.g., $\sim$4 meV for $\epsilon = 16.67$), as shown in Fig. 32. We note that although FCI states at $\nu = -3/5$ were studied in Ref. [34]; Ref. [34] did not show the existence of them at experimentally relevant angles $\sim 3.7°$ and did not study the spin excitations.

APPENDIX E: 2BPV ED RESULTS

In this Appendix, we provide more details on the 2BPV ED results.

1. Parameters in Ref. [28]

First we start with the parameters of Ref. [28]. The ground states are fully polarized at $\nu = -2/3$ in more than 70% of the 2BPV phase diagram [Fig. 7(a)] on a 3×4 system, but the FCI phase is absent at $\nu = -2/3$ in the entire 2BPV phase diagram. However, as mentioned in the main text and from the discussion about the 1BPV, we cannot determine whether this

absence of FCI at $\nu = -2/3$ on a 3×4 system is due to the finite-size effect, since 3×4 systems do not exhibit FCIs at $\nu = -2/3$ even in the 1BPV calculations for the parameters in Ref. [28]. In 1BPV calculations, we found the $\nu = -2/3$ FCI only at 4×6, not for 3×6, 3×5, or 3×4. 2BPV calculations for 4×6 at $\nu = -2/3$ are beyond our numerical accessibility, as the Hilbert space dimension per momentum at 4×6 at $\nu = -2/3$ in the full-spin-polarized sector is larger than 90 billion. In fact, for all the 1BPV and 2BPV calculations that we did with the parameters in Ref. [28], we only find FCI at $\nu = -2/3$ for the system size 4×6 and the interaction strength $\epsilon \in [5, 6.25]$ in 1BPV calculations. Therefore, we will study the 2BPV results for the parameters of Ref. [28] in the 1BPV $\nu = -2/3$ FCI region within $\epsilon \in [5, 6.25]$.

We first discuss $\nu = -1/3$ and $\nu = -2/3$ at the system sizes of 3×4 and 3×5.

(i) The spin-1 gaps are positive but the spinful gaps are negative at $\nu = -1/3$ for the 3×4 system size and for $\epsilon \in [5, 6.25]$, as shown in Fig. 33(a). The negative spinful gaps and the positive spin-1 gaps at $\nu = -1/3$ for $\epsilon \in [5, 6.25]$ imply that the ground states are spin unpolarized for the 3×4 system size, as exemplified in the spectra of Fig. 34(a). This is in contrast to the fully spin-polarized states at $\nu = -2/3$ for $\epsilon \in [5, 6.25]$ and the system size 3×4.

(ii) As a test of the finite-size effects, we calculate the spinful gap at $\nu = -1/3$ and the spinful gap at $\nu = -2/3$ for the system size of 3×5 and $(\theta, 10/\epsilon) = (3.7^\circ, 2.0)$ [see Fig. 33(a)], which read -1.18 meV and 0.75 meV, respectively. Compared to the corresponding values -0.39 meV and 0.56 meV for the 3×4 system, we see that the difference between $-1/3$ and $-2/3$ is even stronger at a larger size, indicating different magnetic behaviors for these two filling factors.

In contrast to the different the spin-1 and spinful gaps for $\nu = -1/3$ and the system size of 3×4 in first item, the spin-1 gap is equal to the spinful gap at $\nu = -2/3$ for $\epsilon \in [5, 6.25]$ for the same system size. Nevertheless, we should not compare the spin-1 gaps between $\nu = -1/3$ and $\nu = -2/3$; instead we compare the spinful gaps between $\nu = -1/3$ and $\nu = -2/3$ as shown in Fig. 7(a) of the main text. Our findings clearly show a significant contrast in the spin polarization between $\nu = -1/3$ and $\nu = -2/3$, which is consistent with the experimentally observed difference in magnetism between $\nu = -1/3$ and $\nu = -2/3$. In addition, the ground states at $\nu = -1/3$ are not FCIs, which is consistent with the topologically trivial states at $\nu = -1/3$ in experiments.

Although there is a clear difference between $\nu = -1/3$ and $\nu = -2/3$, there is no obvious indication that the difference between $\nu = -2/3$ and $\nu = -4/3$ can be captured at the system size of 3×4 or 3×5 for the parameters in Ref. [28].

(i) The spin-1 gap away from the fully spin-polarized sector at $\nu = -4/3$ is larger than the spin-1 gap at $\nu = -2/3$ for 3×4 systems [see Fig. 9(a) in the main text].

(ii) Even on system size 3×5, the spin-1 gap is still much larger at $\nu = -4/3$ than that at $\nu = -2/3$, as shown in Fig. 35(a). Specifically, at representative parameters $(\theta, \epsilon) = (3.7^\circ, 5)$, the spin-1 gaps at $\nu = -2/3, -4/3$ respectively read 0.56 meV and 2.65 meV for the system size 3×4, and respectively 0.75 meV and 2.56 meV for the system size 3×5, where we can see that the spin-1 gap is roughly the same for the two sizes.

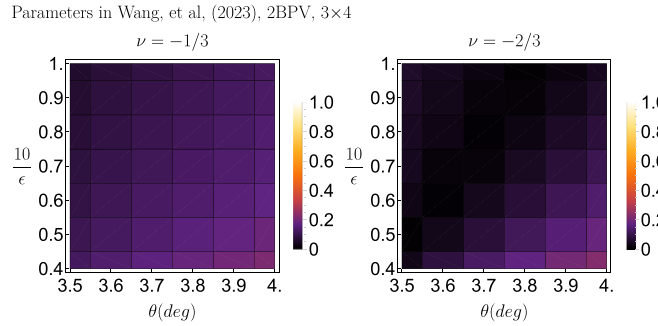

FIG. 36. 2BPV ED calculations of the standard deviation of the $\langle n_k \rangle$ [see Eq. (D1)] for the parameters in Ref. [29] the system size of 3×4. $\langle n_k \rangle$ is calculated for the maximally spin-polarized lowest-energy states at the FCI momenta—$(k_x, k_y) = (0, 2), (1, 2), (2, 2)$ at $\nu = -1/3$ and $(k_x, k_y) = (0, 0), (1, 0), (2, 0)$ for $\nu = -2/3$.

(iii) If we consider the $S_z = S_{\text{max}}^{\text{2BPV}} - 2 = 8 - 2 = 6$ sector at $\nu = -4/3$ for 3×4, $\theta = 3.7^\circ$ and $\epsilon = 5$, the lowest-energy state in the $S_z = 6$ sector has energy higher than the lowest-energy state in the $S_z = S_{\text{max}}^{\text{2BPV}} = 8$ sector by about 7 meV and higher than the lowest-energy states in the $S_z = S_{\text{max}}^{\text{2BPV}} = 7$ sector by about 4.5 meV as shown in Fig. 34(a).

These findings indicate that the large-spin states might be favored. Nevertheless, as discussed in Sec. VI of the main text, the 1BPV maximally spin-polarized state at $\nu = -4/3$ corresponds to the 2BPV partially spin-polarized states at $\nu = -4/3$; we need to check whether such 2BPV partially spin-polarized states at $\nu = -4/3$ (with $S_z = S_{\text{max}}^{\text{1BPV}}$) are also energetically favored. In all the three items, we have not got close to the $S_z = S_{\text{max}}^{\text{1BPV}} = 4$ sector for the system size of 3×4. To fully address this question, we use 3×3 systems where all sectors are numerically feasible. In this case, the finite-size effect of the spin-1 gap becomes strong [see Fig. 37(a) for $\theta = 3.7^\circ$ and $\epsilon = 5$], which makes the spin-1 gap at $\nu = -4/3$ negative (about –0.5 meV). Nevertheless, the large-spin states are still the ground states for the interaction strength $\epsilon \in [5, 6.25]$ at $\theta = 3.7^\circ$ as shown in Fig. 37(b), which is significantly different from the clear spin-zero ground states at $\nu = -1/3$ and small-spin ground states at $\nu = -4/3$ for the parameters in Ref. [29] discussed in the following. In fact, the large-spin states at $\nu = -4/3$ are the ground states even for ϵ going to ~ 7 at $\theta = 3.7^\circ$, although the smaller spin states start to become more competitive at smaller interaction [see Fig. 37(b)]. Therefore, we do not see clear numerical evidence that the parameters in Ref. [28] explain the experimental difference between $\nu = -4/3$ and $\nu = -2/3$ at the available system sizes, even if we include remote bands.

Finally, we address the weight of the remote bands in the low-energy states at $\nu = -4/3$. To characterize the weight, we introduce the following quantity to capture the average probability in the remote bands for each spin sector S_z,

$$p_{2,S_z} = \frac{1}{N} \sum_{\boldsymbol{k}} \frac{\langle s_z, \boldsymbol{k} | \hat{n}_2 | s_z, \boldsymbol{k} \rangle}{n}, \tag{E1}$$

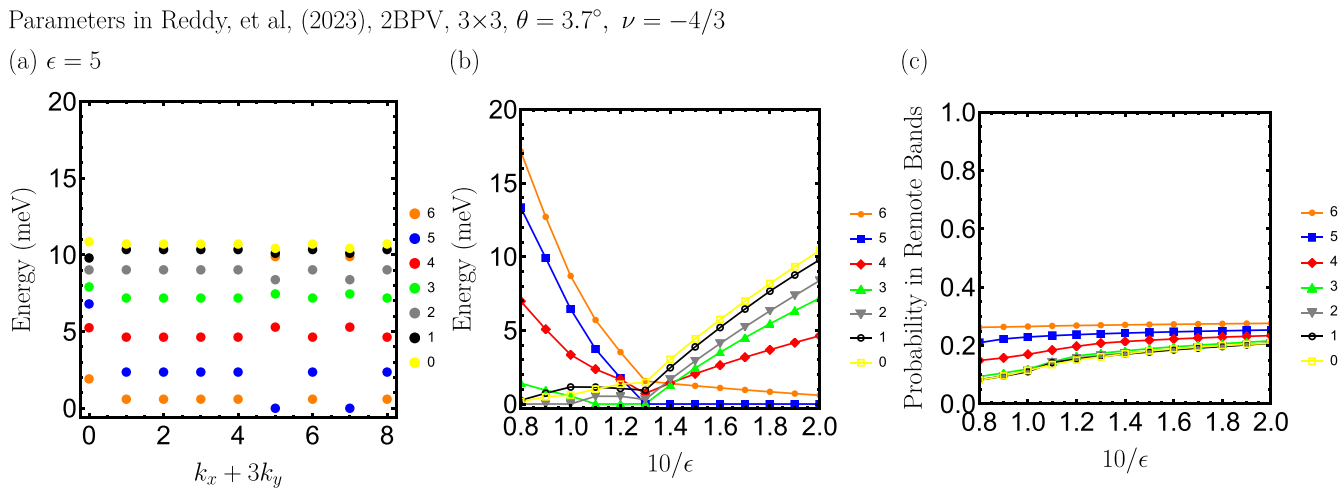

FIG. 37. [(a),(b)] Analogs of Fig. 10 in the main text but for the parameters in Ref. [28]. (a) The many-body 2BPV spectrum at $\nu = -4/3$ for 3×3, the parameters in Ref. [28], $\epsilon = 5$ and $\theta = 3.7°$. We only include the lowest-energy state per momentum per partially spin-polarized sector. For this system size, the FCI states (in the $S^{\text{2BPV}}_{\text{max}} = 6$ and $S^{\text{1BPV}}_{\text{max}} = 3$ sectors) should appear as an (almost) threefold degenerate ground-state manifold at $(k_x, k_y) = (0, 0)$. According to the criterion in Prop. 1, we cannot have FCI states here, since the ground states are not even at (0,0) momentum. The energy of the ground state is set to zero. (b) At each value of ϵ, we show the lowest energy of each spin sector for the parameters specified in the plot. As a comparison of the spin, we note that the spin of the fully spin-polarized state at $\nu = -2/3$ is $S_z = 3$ for the size of 3×3. The energy of the ground state is set to zero at each value of ϵ. (c) At each value of ϵ, we show the average probability in the remote bands p_{2,S_z} in Eq. (E1) for the low-energy states in each spin sector. The parameters are specified in the plot.

where $\hat{n}_2 = \sum_{\boldsymbol{k}',\eta} \widetilde{\gamma}^{\dagger}_{\eta,2,\boldsymbol{k}'} \widetilde{\gamma}_{\eta,2,\boldsymbol{k}'}$ is the holes number operator on the remote bands, $\widetilde{\gamma}^{\dagger}_{\eta,2,\boldsymbol{k}'}$ creates a hole in the second top valence band in the valley η, N is the number of $\boldsymbol{k}$ points, n is the total number of holes, and $|S_z, \boldsymbol{k}\rangle$ is the lowest-energy many-body state in the momentum-$\boldsymbol{k}$ spin-S_z sector. If all (no) holes are in the remote bands, we would have $p_{2,S_z} = 1$ ($p_{2,S_z} = 0$). As shown in Fig. 37(c), p_{2,S_z} is about $0.1 \sim 0.3$, which is non-negligible but reasonable enough to envision perturbation schemes to elucidate the loss of ferromagnetism at this filling factor. Nevertheless, there is a clear decay in the probability compared to that in the top pair of valence bands (about $0.7 \sim 0.9$), meaning the effect of bands beyond the second top pair of valence bands should be negligible even if they are included.

2. Parameters in Ref. [29]

We now turn to the parameters in Ref. [29]. At $\nu = -2/3$ on a 3×4 system, Fig. 7(b) in the main text shows a diagonal region hosting an FCI phase, with neighboring non-FCI phases (see Fig. 39). For the system size of 3×4, we again evaluate the standard deviation of $\langle n_{\boldsymbol{k}} \rangle$ [see Eq. (D1)] for the maximally spin-polarized lowest-energy states at the FCI momenta—$(k_x, k_y) = (0, 0), (1, 0), (2, 0)$ for $\nu = -2/3$. We find that standard deviation at $\nu = -2/3$ can be very small in the FCI region, taking values in [0.006,0.104], which is similar to the 1BPV FCI states at $\nu = -2/3$ for the 4×6 system size and for the parameters in Ref. [29], as discussed in Eq. (D2). As a side note, the standard deviation $\langle n_{\boldsymbol{k}} \rangle$ at $\nu = -1/3$ minimizes in the FCI region without reaching the extremely small values obtained at $\nu = -1/3$. Indeed, the minimum standard deviation of $\langle n_{\boldsymbol{k}} \rangle$ at $\nu = -1/3$ is 0.058 whereas that at $\nu = -2/3$ is 0.006 (Fig. 36).

We focus on the parameter region that gives an FCI phase at $\nu = -2/3$.

(i) In the $\nu = -2/3$ FCI region on a 3×4 system, the spin-1 gaps are mostly about twice the spinful gaps at $\nu = -1/3$, though the spin-1 gap is equal to the spinful gap at $\nu = -2/3$, as shown in Fig. 33(b). So we should use the spinful gaps (instead of spin-1 gaps) as a measure of the magnetic stability at $\nu = -1/3$ and $\nu = -2/3$ as done in the main text.

(ii) Among the 18 points in the phase diagram Fig. 7(b) that give FCIs at $\nu = -2/3$ at the 3×4 system size, there is one point that favors spin-unpolarized (i.e., spin zero) ground states at $\nu = -1/3$.

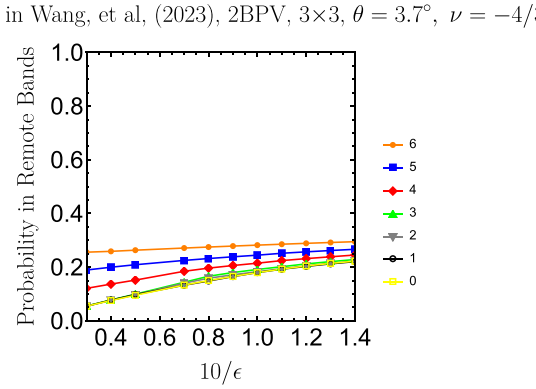

FIG. 38. Analog of Fig. 37(c) but for the parameters in Ref. [29]. At each value of ϵ, we show the average probability in the remote bands p_{2,S_z} in Eq. (E1) for the low-energy states in each spin sector.

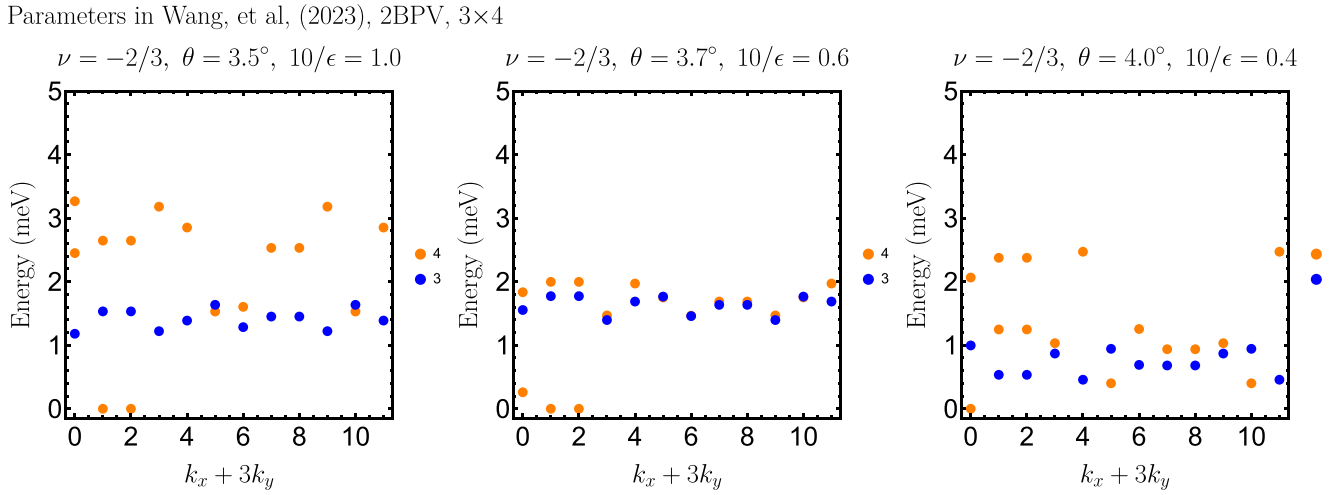

FIG. 39. The many-body spectrum at 3×4 for 2BPV at $\nu = -2/3$ and for the parameter values of Ref. [29]. The ground-state energy is chosen to be zero. We only include two spin sectors $S_z = S^{\text{2BPV}}_{\text{max}}, S^{\text{2BPV}}_{\text{max}} - 1$ at $\nu = -2/3$, and the lowest-energy state per momentum in each spin sector except at the momenta where FCI states might occur, namely $(k_x, k_y) = (0, 0), (1, 0), (2, 0)$. According to the criterion in Prop. 1, FCI states only exist in the middle plot.

(iii) For the other 17 points of the 18 points in the last item, we find fully spin-polarized ground states at $\nu = -1/3$ (FCI states for 11 of them), but ratio between the spinful gaps at $\nu = -1/3$ and $\nu = -2/3$ (former divided by latter) takes values in $[0.03, 0.27]$ with the mean value 0.13, as shown in Table III. [For these 17 points, the spin-zero state again has lower energy than the partially spin-polarized state at $\nu = -1/3$, as exemplified in Fig. 33(b).]

(iv) As a test of the finite-size effect, the spinful gaps at $\nu = -1/3$ and $\nu = -2/3$ $(\theta, 10/\epsilon) = (3.7^\circ, 0.6)$ respectively read 0.22 meV and 1.40 meV for the 3×4 system, where the ratio (former divided by latter) is 0.16; the spinful gaps at $\nu = -1/3$ and $\nu = -2/3$ $(\theta, 10/\epsilon) = (3.7^\circ, 0.6)$ read 0.52 meV and 1.48 meV for the 3×5 system, where the ratio (former divided by latter) is 0.35.

Therefore, when $\nu = -2/3$ features a fully spin-polarized FCI, the state at $\nu = -1/3$ is either spin unpolarized (1/18 of the region) or fully spin polarized with magnetic stability much weaker than that at $\nu = -2/3$ (17/18 of the region) at the 3×4 system size. The difference between the $\nu = -1/3$ and $\nu = -2/3$ spin-1 gap is decreased as the size increases (ratio changes from 0.16 to 0.35), but not significant enough to eliminate the trend that $\nu = -1/3$ has much weaker magnetic stability than $\nu = -2/3$, hinting towards different

TABLE III. The summary of the spin-1 gap and spinful gap values for the parameters in Ref. [29] and for system size 3×4 at $\nu = -1/3, -2/3$ in 2BPV calculations. We only include the angles and dielectric constant values in the phase diagram that leads to an FCI phase at $\nu = -2/3$.

θ	$10/\epsilon$	Spinful Gap$_{\nu=-1/3}$ (meV)	Spin-1 Gap$_{\nu=-1/3}$ (meV)	Spinful Gap$_{\nu=-2/3}$ (meV)	Spin-1 Gap$_{\nu=-2/3}$ (meV)	$\frac{\text{Spinful Gap}_{\nu=-1/3}}{\text{Spinful Gap}_{\nu=-2/3}}$
3.5	0.40	0.23	0.44	1.12	1.12	0.21
3.5	0.50	0.32	0.63	1.20	1.20	0.27
3.6	0.40	0.14	0.27	1.33	1.33	0.10
3.6	0.50	0.23	0.47	1.27	1.27	0.18
3.6	0.60	0.32	0.66	1.38	1.38	0.23
3.7	0.50	0.15	0.30	1.42	1.42	0.10
3.7	0.60	0.22	0.48	1.40	1.40	0.16
3.7	0.70	0.29	0.65	1.54	1.54	0.19
3.8	0.60	0.15	0.33	1.49	1.49	0.10
3.8	0.70	0.22	0.50	1.49	1.49	0.15
3.8	0.80	0.27	0.66	1.67	1.67	0.16
3.9	0.70	0.12	0.34	1.54	1.54	0.08
3.9	0.80	0.21	0.51	1.55	1.55	0.13
3.9	0.90	0.26	0.66	1.77	1.77	0.15
4.0	0.70	−0.15	0.18	1.66	1.66	−0.09
4.0	0.80	0.06	0.34	1.57	1.57	0.04
4.0	0.90	0.18	0.50	1.57	1.57	0.12
4.0	1.00	0.23	0.65	1.83	1.83	0.13

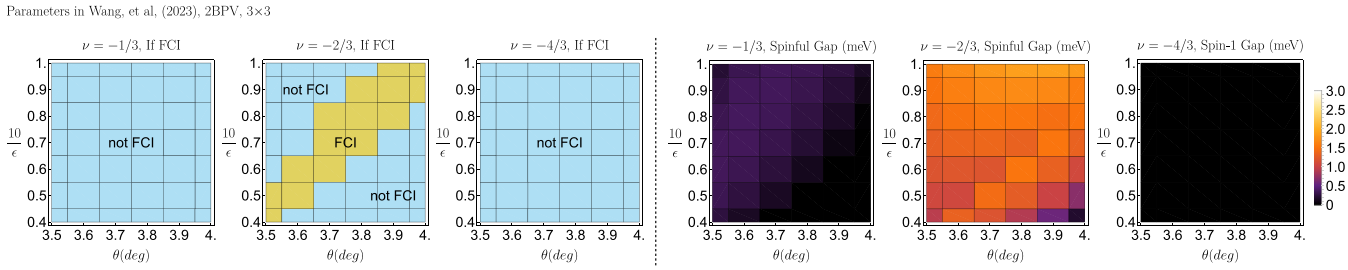

FIG. 40. The 2BPV ED calculation done for parameter values in Ref. [29] on a 3×3 system. In the leftmost three figures, green ("FCI") labels the region that satisfies the criterion in Prop. 1, and blue ("not FCI") means that we do not see clear signatures of FCI or maximally spin-polarized CDW. The rightmost three figures give the spin-1 or spinful gaps, which are shown with the same color scale for all plots. If the spin-1 or spinful gap is negative, it is set to zero in the plot.

magnetic behaviors at $\nu = -1/3$ and $\nu = -2/3$. Such difference between $\nu = -1/3$ and $\nu = -2/3$ is consistent with the experiments. However, the ground states at $\nu = -1/3$ are still mostly FCIs for the parameters of Ref. [29], which is inconsistent with the topologically trivial states at $\nu = -1/3$ in experiments.

Now we discuss the difference between $\nu = -4/3$ and $\nu = -2/3$.

(i) Figure 9(b) in the main text for the system size of 3×4 shows that the fully spin-polarized state is not favored at $\nu = -4/3$ for the parameter values in Ref. [29], according to the negative spin-1 gaps.

(ii) The fact that the fully spin-polarized state is not favored at $\nu = -4/3$ persists to the system size of 3×5 at $(\theta, \epsilon) = (3.7^\circ, 50/3)$ (which leads to an FCI at $\nu = -2/3$ for the experimentally relevant angle) as shown in Fig. 35(b).

(iii) At $\nu = -4/3$ for 3×4, $\theta = 3.7^\circ$ and $\epsilon = 50/3 \approx 16.67$, the lowest-energy state in the $S_z = 6$ sector has energy lower than the lowest-energy state in the $S_z = S_{\text{max}}^{\text{2BPV}} = 8$ sector by about 6 meV and lower than the lowest-energy states in the $S_z = S_{\text{max}}^{\text{2BPV}} = 7$ sector by about 2.5 meV as shown in Fig. 34(b).

These findings indicate that the small-spin states might be favored. Still, we are away from the $S_z = S_{\text{max}}^{\text{1BPV}} = 4$ sector for the system size of 3×4, where a potential FCI phase similar to the 1BPV case could emerge. Since it is technically difficult to probe lower S_z sectors on a 3×4 system, we look at the smaller 3×3 case. Despite its moderate size, it has a similar FCI region at $\nu = -2/3$ and similar spinful gap at $\nu = -2/3$ and similar spin-1 gap $\nu = -4/3$ as those of the system size 3×4, as indicated by the comparison of Fig. 40 and Figs. 7(b) and 9(b) in the main text. The results for the system size of 3×3 for $\nu = -4/3$ suggest that the partially spin-polarized states that correspond to the 1BPV maximally spin-polarized states are not favored at $\nu = -4/3$; instead it is the small spin ($S_z = 0, 1$) states that are favored for the parameters that give FCIs at $\nu = -2/3$ (roughly $10/\epsilon = 0.5 \sim 0.7$ at $\theta = 3.7^\circ$). Interestingly, as shown in Fig. 38 the weight of the remote bands in the low-energy states at $\nu = -4/3$ (about $0.1 \sim 0.3$) is similar to that for the parameters in Ref. [28], which is considerable. Still, there is a clear decay in the probability compared to that in the top pair of valence bands (about $0.7 \sim 0.9$), meaning that the bands beyond the two bands per valley are negligible even if they are included. Therefore, the parameters in Ref. [29] can capture the observed difference between $\nu = -4/3$ and $\nu = -2/3$, although this fit to the experimental phase diagram relies on a weaker interaction, namely $\epsilon > 10$.

[1] T. Neupert, L. Santos, C. Chamon, and C. Mudry, Phys. Rev. Lett. **106**, 236804 (2011).

[2] D. N. Sheng, Z.-C. Gu, K. Sun, and L. Sheng, Nat. Commun. **2**, 389 (2011).

[3] N. Regnault and B. A. Bernevig, Phys. Rev. X **1**, 021014 (2011).

[4] E. Tang, J.-W. Mei, and X.-G. Wen, Phys. Rev. Lett. **106**, 236802 (2011).

[5] K. Sun, Z. Gu, H. Katsura, and S. Das Sarma, Phys. Rev. Lett. **106**, 236803 (2011).

[6] Y. Cao, V. Fatemi, A. Demir, S. Fang, S. L. Tomarken, J. Y. Luo, J. D. Sanchez-Yamagishi, K. Watanabe, T. Taniguchi, E. Kaxiras *et al.*, Nature (London) **556**, 80 (2018).

[7] Y. Cao, V. Fatemi, S. Fang, K. Watanabe, T. Taniguchi, E. Kaxiras, and P. Jarillo-Herrero, Nature (London) **556**, 43 (2018).

[8] E. J. Bergholtz and Z. Liu, Int. J. Mod. Phys. B **27**, 1330017 (2013).

[9] S. A. Parameswaran, R. Roy, and S. L. Sondhi, C. R. Phys. **14**, 816 (2013).

[10] A. Abouelkomsan, Z. Liu, and E. J. Bergholtz, Phys. Rev. Lett. **124**, 106803 (2020).

[11] P. J. Ledwith, G. Tarnopolsky, E. Khalaf, and A. Vishwanath, Phys. Rev. Res. **2**, 023237 (2020).

[12] C. Repellin and T. Senthil, Phys. Rev. Res. **2**, 023238 (2020).

[13] D. Parker, P. Ledwith, E. Khalaf, T. Soejima, J. Hauschild, Y. Xie, A. Pierce, M. P. Zaletel, A. Yacoby, and A. Vishwanath, arXiv:2112.13837.

[14] P. Wilhelm, T. C. Lang, and A. M. Läuchli, Phys. Rev. B **103**, 125406 (2021).

[15] Y. Sheffer and A. Stern, Phys. Rev. B **104**, L121405 (2021).

[16] H. Li, U. Kumar, K. Sun, and S.-Z. Lin, Phys. Rev. Res. **3**, L032070 (2021).

[17] V. Crépel and L. Fu, Phys. Rev. B **107**, L201109 (2023).

[18] J. Dong, J. Wang, and L. Fu, arXiv:2208.10516.

[19] A. Abouelkomsan, K. Yang, and E. J. Bergholtz, Phys. Rev. Res. **5**, L012015 (2023).

[20] N. Morales-Durán, J. Wang, G. R. Schleder, M. Angeli, Z. Zhu, E. Kaxiras, C. Repellin, and J. Cano, Phys. Rev. Res. **5**, L032022 (2023).

[21] Y.-M. Wu, D. Shaffer, Z. Wu, and L. H. Santos, arXiv:2309.07222.

[22] Y. Xie, A. T. Pierce, J. M. Park, D. E. Parker, E. Khalaf, P. Ledwith, Y. Cao, S. H. Lee, S. Chen, P. R. Forrester *et al.*, Nature (London) **600**, 439 (2021).

[23] E. M. Spanton, A. A. Zibrov, H. Zhou, T. Taniguchi, K. Watanabe, M. P. Zaletel, and A. F. Young, Science **360**, 62 (2018).

[24] J. Cai, E. Anderson, C. Wang, X. Zhang, X. Liu, W. Holtzmann, Y. Zhang, F. Fan, T. Taniguchi, K. Watanabe *et al.*, Nature (London) **622**, 63 (2023).

[25] Y. Zeng, Z. Xia, K. Kang, J. Zhu, P. Knüppel, C. Vaswani, K. Watanabe, T. Taniguchi, K. F. Mak, and J. Shan, Nature (London) **622**, 69 (2023).

[26] H. Park, J. Cai, E. Anderson, Y. Zhang, J. Zhu, X. Liu, C. Wang, W. Holtzmann, C. Hu, Z. Liu *et al.*, Nature (London) **622**, 74 (2023).

[27] F. Xu, Z. Sun, T. Jia, C. Liu, C. Xu, C. Li, Y. Gu, K. Watanabe, T. Taniguchi, B. Tong, J. Jia, Z. Shi, S. Jiang, Y. Zhang, X. Liu, and T. Li, Phys. Rev. X **13**, 031037 (2023).

[28] A. P. Reddy, F. F. Alsallom, Y. Zhang, T. Devakul, and L. Fu, Phys. Rev. B **108**, 085117 (2023).

[29] C. Wang, X.-W. Zhang, X. Liu, Y. He, X. Xu, Y. Ran, T. Cao, and D. Xiao, arXiv:2304.11864.

[30] W.-X. Qiu, B. Li, X.-J. Luo, and F. Wu, Phys. Rev. X **13**, 041026 (2023).

[31] J. Dong, J. Wang, P. J. Ledwith, A. Vishwanath, and D. E. Parker, Phys. Rev. Lett. **131**, 136502 (2023).

[32] H. Goldman, A. P. Reddy, N. Paul, and L. Fu, Phys. Rev. Lett. **131**, 136501 (2023).

[33] N. Morales-Durán, N. Wei, and A. H. MacDonald, arXiv:2308.03143.

[34] A. P. Reddy and L. Fu, arXiv:2308.10406.

[35] X.-Y. Song, Y.-H. Zhang, and T. Senthil, arXiv:2308.10903.

[36] C. Xu, J. Li, Y. Xu, Z. Bi, and Y. Zhang, arXiv:2308.09697.

[37] T. Wang, T. Devakul, M. P. Zaletel, and L. Fu, arXiv:2306.02501.

[38] X. Liu, C. Wang, X.-W. Zhang, T. Cao, and D. Xiao, arXiv:2308.07488.

[39] F. Wu, T. Lovorn, E. Tutuc, I. Martin, and A. H. MacDonald, Phys. Rev. Lett. **122**, 086402 (2019).

[40] A. Laturia, M. L. Van de Put, and W. G. Vandenberghe, npj 2D Mater. Appl. **2**, 6 (2018).

[41] D. Xiao, G.-B. Liu, W. Feng, X. Xu, and W. Yao, Phys. Rev. Lett. **108**, 196802 (2012).

[42] C. Robert, R. Picard, D. Lagarde, G. Wang, J. P. Echeverry, F. Cadiz, P. Renucci, A. Högele, T. Amand, X. Marie, I. C. Gerber, and B. Urbaszek, Phys. Rev. B **94**, 155425 (2016).

[43] R. Bistritzer and A. H. MacDonald, Proc. Natl. Acad. Sci. USA **108**, 12233 (2011).

[44] Z.-D. Song, Z. Wang, W. Shi, G. Li, C. Fang, and B. A. Bernevig, Phys. Rev. Lett. **123**, 036401 (2019).

[45] C. Xu, J. Li, Y. Xu, Z. Bi, and Y. Zhang, arXiv:2308.09697.

[46] R. Roy, Phys. Rev. B **90**, 165139 (2014).

[47] B. Estienne, N. Regnault, and V. Crépel, Phys. Rev. Res. **5**, L032048 (2023).

[48] P. J. Ledwith, A. Vishwanath, and D. E. Parker, arXiv:2209.15023.

[49] J. Wang, J. Cano, A. J. Millis, Z. Liu, and B. Yang, Phys. Rev. Lett. **127**, 246403 (2021).

[50] J. Wang, S. Klevtsov, and Z. Liu, Phys. Rev. Res. **5**, 023167 (2023).

[51] Y. Hu, Y. Xu, and B. Lian, arXiv:2310.04070.

[52] O. Vafek and J. Kang, Phys. Rev. B **107**, 075123 (2023).

[53] J. Kang and O. Vafek, Phys. Rev. B **107**, 075408 (2023).

[54] C. Fang, M. J. Gilbert, and B. A. Bernevig, Phys. Rev. B **86**, 115112 (2012).

[55] M. G. Vergniory, L. Elcoro, Z. Wang, J. Cano, C. Felser, M. I. Aroyo, B. A. Bernevig, and B. Bradlyn, Phys. Rev. E **96**, 023310 (2017).

[56] J. Cano, B. Bradlyn, Z. Wang, L. Elcoro, M. G. Vergniory, C. Felser, M. I. Aroyo, and B. A. Bernevig, Phys. Rev. B **97**, 035139 (2018).

[57] B. Bradlyn, L. Elcoro, J. Cano, M. G. Vergniory, Z. Wang, C. Felser, M. I. Aroyo, and B. A. Bernevig, Nature (London) **547**, 298 (2017).

[58] S. M. Girvin, Phys. Rev. B **29**, 6012 (1984).

[59] A. M. Läuchli, Z. Liu, E. J. Bergholtz, and R. Moessner, Phys. Rev. Lett. **111**, 126802 (2013).

[60] B. Mera and T. Ozawa, arXiv:2304.00866.

[61] J. Herzog-Arbeitman, A. Chew, D. K. Efetov, and B. A. Bernevig, Phys. Rev. Lett. **129**, 076401 (2022).

[62] E. H. Rezayi, Phys. Rev. Lett. **119**, 026801 (2017).

[63] L. Herviou and F. Mila, Phys. Rev. B **107**, 115137 (2023).

[64] S. Murakami and N. Nagaosa, Phys. Rev. Lett. **90**, 057002 (2003).

[65] Y. Li and F. D. M. Haldane, Phys. Rev. Lett. **120**, 067003 (2018).

[66] N. Bultinck, S. Chatterjee, and M. P. Zaletel, Phys. Rev. Lett. **124**, 166601 (2020).

[67] J. Yu, M. Xie, F. Wu, and S. Das Sarma, Phys. Rev. B **107**, L201106 (2023).

[68] E. Lieb, T. Schultz, and D. Mattis, Ann. Phys. **16**, 407 (1961).

[69] Y.-L. Wu, N. Regnault, and B. A. Bernevig, Phys. Rev. B **89**, 155113 (2014).

[70] J. M. B. Lopes dos Santos, N. M. R. Peres, and A. H. Castro Neto, Phys. Rev. Lett. **99**, 256802 (2007).

[71] S. Fang, S. Carr, Z. Zhu, D. Massatt, and E. Kaxiras, arXiv:1908.00058.

[72] T. Zhang, N. Regnault, B. A. Bernevig, X. Dai, and H. Weng, Phys. Rev. B **105**, 125127 (2022).

[73] D. E. Parker, T. Soejima, J. Hauschild, M. P. Zaletel, and N. Bultinck, Phys. Rev. Lett. **127**, 027601 (2021).

[74] Y. H. Kwan, G. Wagner, T. Soejima, M. P. Zaletel, S. H. Simon, S. A. Parameswaran, and N. Bultinck, Phys. Rev. X **11**, 041063 (2021).

[75] G. Wagner, Y. H. Kwan, N. Bultinck, S. H. Simon, and S. A. Parameswaran, Phys. Rev. Lett. **128**, 156401 (2022).

[76] N. Nakatsuji and M. Koshino, Phys. Rev. B **105**, 245408 (2022).

[77] T. Wang, D. E. Parker, T. Soejima, J. Hauschild, S. Anand, N. Bultinck, and M. P. Zaletel, arXiv:2211.02693.

[78] X. Wang, J. Finney, A. L. Sharpe, L. K. Rodenbach, C. L. Hsueh, K. Watanabe, T. Taniguchi, M. A. Kastner, O. Vafek, and D. Goldhaber-Gordon, Proc. Natl. Acad. Sci. USA **120**, e2307151120 (2023).
[79] K. P. Nuckolls, R. L. Lee, M. Oh, D. Wong, T. Soejima, J. P. Hong, D. Călugăru, J. Herzog-Arbeitman, B. A. Bernevig, K. Watanabe *et al.*, Nature (London) **620**, 525 (2023).
[80] E. Y. Andrei, D. K. Efetov, P. Jarillo-Herrero, A. H. MacDonald, K. F. Mak, T. Senthil, E. Tutuc, A. Yazdani, and A. F. Young, Nat. Rev. Mater. **6**, 201 (2021).
[81] E. Y. Andrei and A. H. MacDonald, Nat. Mater. **19**, 1265 (2020).
[82] K. F. Mak and J. Shan, Nat. Nanotechnol. **17**, 686 (2022).
[83] Z. Bi, N. F. Q. Yuan, and L. Fu, Phys. Rev. B **100**, 035448 (2019).
[84] T. Devakul, V. Crépel, Y. Zhang, and L. Fu, Nat. Commun. **12**, 6730 (2021).
[85] Z. Hennighausen and S. Kar, Electron. Struct. **3**, 014004 (2021).
[86] P. Mai, B. E. Feldman, and P. W. Phillips, Phys. Rev. Res. **5**, 013162 (2023).
[87] P. Mai, J. Zhao, B. E. Feldman, and P. W. Phillips, Nat. Commun. **14**, 5999 (2023).
[88] Z. Liu, E. J. Bergholtz, H. Fan, and A. M. Läuchli, Phys. Rev. Lett. **109**, 186805 (2012).
[89] A. Sterdyniak, C. Repellin, B. A. Bernevig, and N. Regnault, Phys. Rev. B **87**, 205137 (2013).
[90] M. Udagawa and E. J. Bergholtz, J. Stat. Mech.: Theory Exp. (2014) P10012.
[91] Y.-H. Wu, J. K. Jain, and K. Sun, Phys. Rev. B **91**, 041119(R) (2015).
[92] B. d. z. Jaworowski, N. Regnault, and Z. Liu, Phys. Rev. B **99**, 045136 (2019).
[93] Z. Liu and E. J. Bergholtz, in *Encyclopedia of Condensed Matter Physics*, Vol. 1 (Elsevier, Amsterdam, 2024), pp. 515–538.
[94] X. Liu, G. Farahi, C.-L. Chiu, Z. Papic, K. Watanabe, T. Taniguchi, M. P. Zaletel, and A. Yazdani, Science **375**, 321 (2022).
[95] Y. Hu, Y.-C. Tsui, M. He, U. Kamber, T. Wang, A. S. Mohammadi, K. Watanabe, T. Taniguchi, Z. Papic, M. P. Zaletel, and A. Yazdani, arXiv:2308.05789.
[96] G. Farahi, C.-L. Chiu, X. Liu, Z. Papic, K. Watanabe, T. Taniguchi, M. P. Zaletel, and A. Yazdani, arXiv:2303.16993.
[97] S. Zhao, J. Huang, V. Crépel, X. Wu, T. Zhang, H. Wang, X. Han, Z. Li, C. Xi, S. Pan *et al.*, arXiv:2308.02821.
[98] X. Qian, J. Liu, L. Fu, and J. Li, Science **346**, 1344 (2014).
[99] Y. Qi, P. G. Naumov, M. N. Ali, C. R. Rajamathi, W. Schnelle, O. Barkalov, M. Hanfland, S.-C. Wu, C. Shekhar, Y. Sun, V. Süß *et al.*, Nat. Commun. **7**, 11038 (2016).
[100] L. Elcoro, B. J. Wieder, Z. Song, Y. Xu, B. Bradlyn, and B. A. Bernevig, Nat. Commun. **12**, 5965 (2021).
[101] M. Aroyo, J. Perez-Mato, C. Capillas, E. Kroumova, S. Ivantchev, G. Madariaga, A. Kirov, and H. Wondratschek, Z. Kristallogr. **221**, 15 (2006).
[102] M. I. Aroyo, A. Kirov, C. Capillas, J. M. Perez-Mato, and H. Wondratschek, Acta Crystallogr. Sect. A **62**, 115 (2006).
[103] C. Brouder, G. Panati, M. Calandra, C. Mourougane, and N. Marzari, Phys. Rev. Lett. **98**, 046402 (2007).
[104] J. Herzog-Arbeitman, V. Peri, F. Schindler, S. D. Huber, and B. A. Bernevig, Phys. Rev. Lett. **128**, 087002 (2022).